United States Department of Energy award number DE-EE0000467

The Effect of Airborne Contaminants on Fuel Cell Performance and Durability

Final scientific/technical report

Jean St-Pierre, principal investigator
Hawaii Natural Energy Institute
School of Ocean and Earth Science and Technology
University of Hawai‘i Mānoa
1680 East-West Road, POST 109
Honolulu, HI 96822
Phone: (808) 956-3909 / Fax: (808) 956-2336 / Email: jsp7@hawaii.edu

Subcontractors:
University of Connecticut, Ugur Pasaogullari
Ballard Power Systems, Tommy Cheng
WPCSOL, William Collins

This material is based upon work supported by the U.S. Department of Energy's Office of Energy Efficiency and Renewable Energy (EERE) under the Fuel Cell Technologies Office (FCTO) under Award Number DE-EE0000467.

Executive summary

The commercialization of proton exchange membrane fuel cells vehicles has begun. However, a successful diffusion of this technology is in part relying on its field performance including durability. Airborne contaminants originating from natural or anthropogenic sources, which negatively impact fuel cell performance at concentrations as low as a few part per million in many cases, increase fuel cell deployment risks because air filter specifications or life are either missing or are currently unknown for many species. Furthermore, air filters may fail or may only be replaced after their useful life has been exceeded. For a more robust system, a more thorough understanding of the impact of contaminants on fuel cell performance is needed to document air filter specifications (prevention) and devise recovery procedures (maintenance) that are effective at the system level.

Eight previously undocumented airborne contaminants were selected for detailed studies from more than 200 identified species (acetonitrile, acetylene, bromomethane, iso-propanol, methyl methacrylate, naphthalene, propene, Ca^{2+} cation). Tolerance limits were derived from data obtained with different contaminant concentrations. Other characterization data, including the effect of current density, led to the identification of operating conditions intensifying contamination effects: low temperatures are relevant to vehicle startup in cold environments whereas low platinum catalyst loadings are essential to decrease vehicle cost. The use of many and complementary electrochemical, chemical and physical characterization methods and the derivation of several mathematical models supported the formulation of contamination mechanisms and the development of recovery procedures. The complexity of these contamination mechanisms, for example affecting all cell voltage loss types (kinetic, ohmic, mass transport) in several different ways, suggests a shift to prevention and generic maintenance measures. Only two of the selected contaminants led to cell voltage losses after injection was interrupted. Proposed recovery procedures for calcium ions, a component of road de-icers, dessicants, fertilizers and soil conditioners, were either ineffective or partly effective, whereas for bromomethane, a fumigant, the cell voltage was recovered to its initial value before contamination by manipulating and sequencing operating conditions. However, implementation for a fuel cell stack and system remains to be demonstrated. Contamination mechanisms also led to the identification of membrane durability stressors. All 8 selected contaminants promote the formation of hydrogen peroxide, a known agent that can produce radicals that attack the ionomer and membrane molecular structure whereas the dehydrating effect of calcium ions on the ionomer and membrane increases their brittleness and favors the creation of pinholes under mechanical stresses. In view of the large quantity of material produced, data related to acetylene, acetonitrile and calcium ions were emphasized. The reader is directed to the team's publications for a more detailed account (section 3.1).

The project team pioneered the screening of agents used to clean fuel cell system parts. It was demonstrated that all 8 industrial cleansers, selected from a pool of approximately 60 candidates, were well-suited for fuel cells because the cell voltage was only partially recoverable within a single hydrogen fuel fill or the cell voltage fell below the fuel cell system power electronics low end operating point. Specific fuel cell cleansers need to be developed. A provisional patent covering a concept to measure the catalyst area covered by the ionomer was inspired by the developed contamination mechanisms and would benefit activities focusing on the increase in

platinum or other catalyst utilization. Contamination mechanisms also inspired a concept for a new and generic recovery procedure that is currently being explored using other federal funds.

Key words: Proton exchange membrane fuel cell, polymer electrolyte membrane fuel cell, durability, cathode contamination, contamination mechanism, contaminant tolerance limit, contamination recovery procedure

Table of contents

1 Comparison of the actual accomplishments with the goals and objectives of the project

The project 4 milestones and the 2 key objectives, defining contaminant tolerance limits and devising effective recovery procedures, are summarized in this section. Additional intermediate milestones were added to the original set to take account of the revised milestone 4 delivery date (March 31, 2014 revised to December 31, 2015). These additional milestones and corresponding accomplishments are listed in table 1.1.1. Additional details are provided in section 2.

1.1 Milestones and go/no go decisions

Milestone 1 (March 31, 2011): Prioritize a group of ~10 airborne contaminants of relevance to stationary and automotive fuel cell applications based on i) their performance impact (screening results), ii) occurrence (literature results, industry exchange)

- Result: 11 contaminants ranked using 2 quantitative criteria by March 11, 2011. Most contaminants were selected from Environmental Protection Agency data with a few suggestions from Nuvera (2,2-bis(4-hydroxyphenyl)propane, methyl methacrylate) and the Fuel Cell Tech Team (1,1-difluoroethane, 1,1,1,2-tetrafluoroethane)

Milestone 2 (March 31, 2012): Quantify performance loss for at least 4 different contaminants under various operating conditions

- Result: The performance loss for 4 contaminants (acetylene, 5-100 ppm; methyl methacrylate, 2-100 ppm; naphthalene, 0.5-2.3 ppm; propene, 2-100 ppm) was determined for different contaminant concentrations, current densities (0.2-1 A cm^{-2}) and temperatures (10-80 °C) by March 28, 2012

Go/no go decision 1 (March 31, 2012): Identify contaminants (and concentrations) resulting in performance loss ≥ 20 % of initial performance

- Result: The contamination concentration leading to a 20 % performance loss was determined (acetylene, ~16 ppm; methyl methacrylate, ~20 ppm; naphthalene, ~1.4 ppm; propene, ~100 ppm) by March 28, 2012

Go/no go decision 2 (March 31, 2012): Quantify effects of various conditions on cell poisoning. Data reported to modelers (within the team)

- Result: The performance loss for 4 contaminants (acetylene, 5-100 ppm; methyl methacrylate, 2-100 ppm; naphthalene, 0.5-2.3 ppm; propene, 2-100 ppm) was determined for different contaminant concentrations, current densities (0.2-1 A cm^{-2}) and temperatures (10-80 °C) and data were available for use by team members by March 28, 2012.

Go/no go decision 3 (March 31, 2012): Identify mitigation strategies, restoring cell to 90 % of initial performance, for reversible contaminants (interpreted as 90 % recovery of voltage loss at steady state)

- Result: More than 90 % of the voltage loss at steady state was recovered after contaminant injection interruption (acetylene, methyl methacrylate, propene) with the exception of naphthalene for some operating conditions. Operation condition changes

were sufficient to recover performance after naphthalene exposure (cell operation with H_2/N_2 for cyclic voltammetry or for a polarization curve)

Milestone 3 (March 31, 2013): Quantify the local variability in performance loss over the cell active area for at least 4 different contaminants. Identify principal poisoning mechanism for these contaminants

- Result: Diagnostic tests encompassing kinetic (oxygen reduction catalyst active area, hydrogen peroxide yield and Tafel slope, contaminant intermediates/products and their yield), ohmic (membrane and catalyst layer ionomer conductivity) and mass transport (oxygen mass transport resistance, change in current distribution) contributions were completed by April 10, 2013, including rotating/ring disc electrode tests (6 contaminants), membrane conductivity cell tests (2 contaminants including acetonitrile, the only selected organic contaminant leading to *in situ* ohmic losses), segmented cell tests (3 contaminants with another contaminant test partially completed), fuel cell coupled with gas chromatography tests (4 contaminants), and impedance spectroscopy tests (7 contaminants). A general contamination mechanism was postulated based on these results

Milestone 4 (March 31, 2014 revised to December 31, 2015): Demonstrate successful mitigation of the impact of the most important 4 airborne contaminants

- Result: An *in situ* solution flush was only partially effective to reverse Ca^{2+} contamination (salt precipitate dissolution, ion exchange with mixed Ca^{2+}/H^+ form ionomer and membrane). Low cell voltage operation was ineffective (water production at the cathode and the higher Ca^{2+} concentration at this location due to the electric field were expected to facilitate ion exchange with H^+ ions in water). Bromomethane contamination was reversible by desorbing product Br^- ions at low cathode potentials and favoring their dissolution in liquid water produced at high current densities). The other 6 selected contaminants recovered under nominal conditions (80 °C) after contaminant exposure ceased
- Result: Other accomplishments related to interim milestones added to take account of the change in delivery date are listed in table 1.1.1

Table 1.1.1. Summary of additional intermediate milestones and corresponding accomplishments.

Milestone	Status	Due Date
M4 (interim): Complete the identification of intermediate or reaction products	Completed	March 2014
Determine the effect of acetonitrile intermediate or reaction products on membrane conductivity	Completed	
Complete segmented fuel cell measurements	Completed	
Complete 4 outreach products	4 journal papers	
M4 (interim): Characterize the long term effects of a contaminant mixture	Delayed (November 2015)	June 2014
Characterize the effect of acidic and cleaning solutions circulation on performance recovery	Completed	
Complete 5 outreach products	3 journal papers, 4 proceedings, 5 conference, GM and SAE presentations	
M4 (interim): Identify differences introduced by metallic bipolar plates	Delayed (November 2015)	September 2014
Characterize the long term effects of an organic contaminant	Completed	
Characterize the long term effects of a foreign cation contaminant	Completed	
Complete 4 outreach products	2 journal papers, 2 proceedings, 4 conference presentations	
M4 (interim): Characterize the effect of sustained OCV periods on fuel cell performance recovery	Delayed (August 2015)	December 2014
Complete 7 outreach products	1 journal paper, 1 conference presentation	
M4: Demonstrate successful mitigation of the impact of the most important 4 airborne contaminants	Delayed (November 2015)	March 2015
Characterize the effect of sustained air starvation and point of zero charge periods on fuel cell performance recovery	Delayed (August 2015)	
Complete 7 outreach products	6 journal papers, 1 SAE presentation	

1.2 Contaminant tolerance limits

Contaminant tolerance limits were derived on the basis of results obtained during milestone 2 (effect of contaminant concentration on cell voltage loss, tables 2.2.1 and 2.2.2, figure 2.2.8, bottom). These tolerance limits are expected to guide filter system design (preventive mitigation). Experimental data for acetonitrile, acetylene and bromomethane are illustrated in figure 1.2.1 as examples.

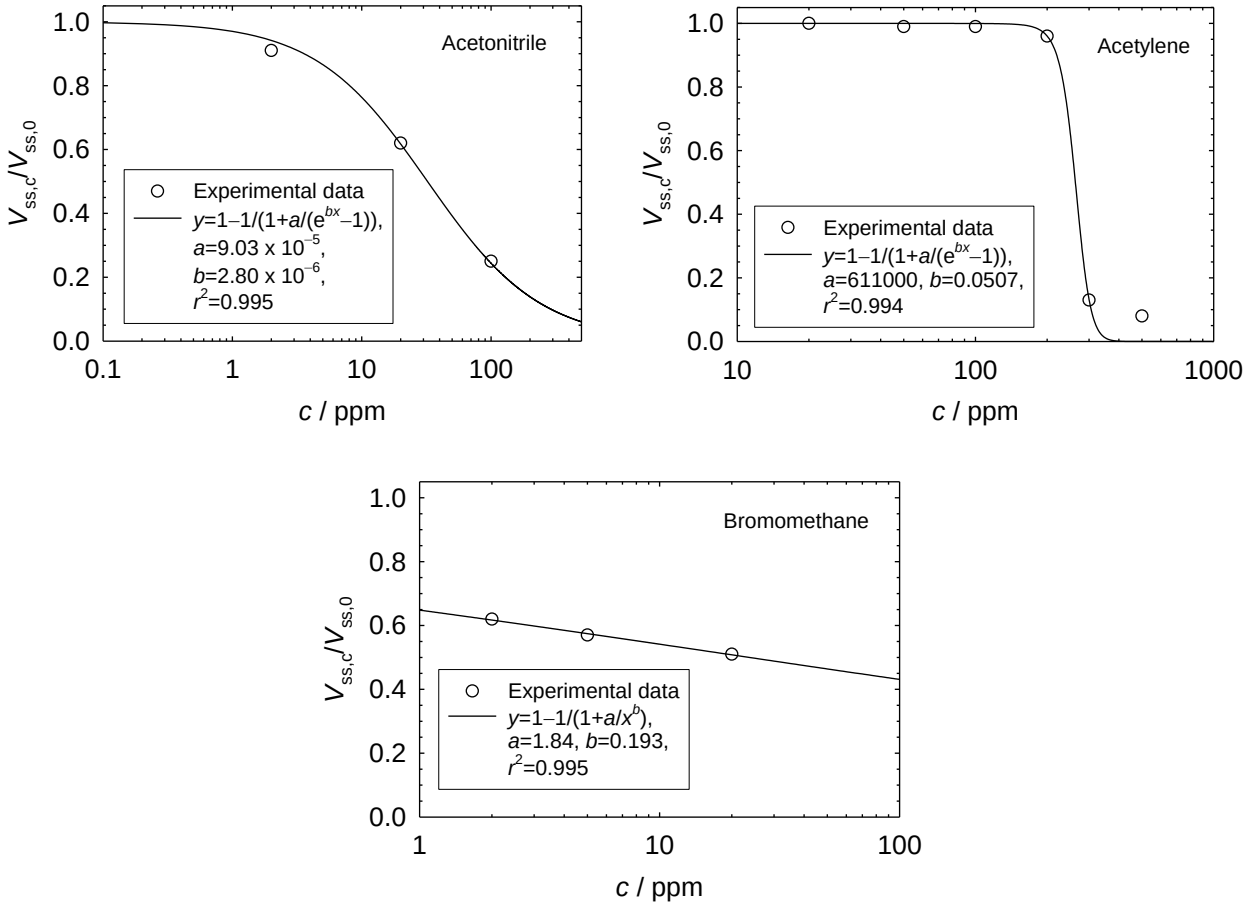

Figure 1.2.1. Dimensionless cell voltage loss as a function of contaminant concentration for acetonitrile, acetylene and bromomethane. c is the contaminant concentration in the air stream, $V_{ss,c}$ is the cell voltage at steady state in the presence of a contaminant, and $V_{ss,0}$ is the steady state cell voltage in the absence of a contaminant.

Generally, data in figure 1.2.1 follow a similar trend. The dimensionless cell voltage loss $V_{ss,c}/V_{ss,0}$ is equal to 1 at low contaminant concentrations (no contaminant effect). At larger contaminant concentrations, the contaminant begins to have a substantial effect and the dimensionless cell voltage loss decreases. Two empirical expressions inspired by a contamination model relation (equation 10 in reference [1]) were used to fit data. Equation 1.2.1 was used for bromomethane whereas equation 1.2.2 was used for all other contaminants.

$$V_{ss,c}/V_{ss,0} = 1 - 1/\left(1 + a/c^{b}\right) \quad (1.2.1)$$

$$V_{ss,c}/V_{ss,0} = 1 - 1/\left(1 + a/\left(e^{bc} - 1\right)\right) \quad (1.2.2)$$

where c is the contaminant concentration in the air stream, $V_{ss,c}$ is the cell voltage at steady state in the presence of a contaminant, $V_{ss,0}$ is the steady state cell voltage in the absence of a contaminant and, a and b are fitted parameters. Equations 1.2.1 and 1.2.2 fitted parameters are given in table 1.2.1 for all studied contaminants. The resulting empirical equations enabled the

calculation of the contaminant concentration that leads to a small cell voltage loss of 0.5, 1 and 5 % (or any other desirable value). The confidence level in these predictions is color coded in table 1.2.1; high for green (located within the experimental contaminant concentration range), medium for yellow (smaller than the lower end of the experimental contaminant concentration range by a factor approximately less than 10) and low for red (much smaller than the lower end of the experimental contaminant concentration range). It is emphasized that these tolerance limits were derived for a specific membrane/electrode assembly and set of operating conditions. It was further assumed that a steady state is reached (with the exception of Ca^{2+} because a steady state was not reached within a 100 h test period) which usually takes in the order of 1 to 100 hours. Therefore, the actual loss for a vehicle is likely overestimated because the operation duration is likely shorter and contaminant effects are reversible for many species.

Table 1.2.1. Contaminant tolerance limits for 5, 1 and 0.5 % fuel cell performance losses at 80 °C and 1 A cm^{-2}.

Contaminant[a]	Predicted contaminant tolerance (ppm)			Experimental contaminant concentration range/ambient air concentration (ppm/ppm carbon)[b]	8 h total weight average permissible exposure limit (ppm)[c]	Empirical correlation parameters[d]		
	$V_{ss,c}/V_{ss,0}$=0.95	$V_{ss,c}/V_{ss,0}$=0.99	$V_{ss,c}/V_{ss,0}$=0.995			*a*	*b*	r^2
Acetonitrile	1.7	0.33	0.16	2-100/3.1	40	9.03×10^{-5}	2.80×10^{-6}	0.995
Acetylene	210	170	158	20-500/0.0386	Simple asphyxiant	611000	0.0507	0.994
Bromomethane	5.7×10^{-6}	1.1×10^{-9}	3.0×10^{-11}	2-20/0.0066	5	1.84	0.193	0.995
Iso-propanol	4200	800	400	250-8600/0.08[e]	200-400[f]	8.53×10^{-5}	1.07×10^{-9}	0.857
Methyl methacrylate	9.9	1.9	0.95	2-100/0.00267	50-100	4.03×10^{-6}	2.13×10^{-8}	0.988
Naphthalene	0.63	0.21	0.12	0.5-2.4/0.05	10	59.2	2.26	0.987
Propene	23	4.5	2.2	2-100/0.102	500	6.86×10^{-6}	1.56×10^{-8}	0.978
Ca^{2+}	3.7	0.71	0.35	2-10/NA		2.13×10^{-7}	3.05×10^{-9}	0.925

[a] Confidence level in contaminant tolerance limits: high in green (located within the experimental contaminant concentration range), medium in yellow (smaller than the lower end of the experimental contaminant concentration range by a factor approximately less than 10), and low in red (much smaller than the lower end of the experimental contaminant concentration range).

[b] 24 h average annual maximum concentration. ppm carbon is the volume concentration in ppm multiplied by the number of carbon atoms in the compound.

[c] From OSHA and/or ACGIH.

[d] Contaminant tolerance limits were estimated based on 2 empirical equations. $V_{ss,c}/V_{ss,0}=1-1/[1+(a/(e^{bc}-1))]$ for acetonitrile, acetylene, iso-propanol, methyl methacrylate, naphthalene, propene and Ca^{2+}, and $V_{ss,c}/V_{ss,0}=1-1/[1+(a/c^{b})]$ for bromomethane where $V_{ss,c}$ is the steady state cell voltage during contamination (100 h value for Ca^{2+}), $V_{ss,0}$ is the steady state cell voltage before contamination, c is the contaminant concentration and, a and b are fitted parameters.

[e] Indoor mean.

[f] For iso-propanol, the experimental concentration range is larger than the lower end of the 8 h total weight average permissible exposure limit range. Therefore, for this hypothetical situation, the driver is also affected by the experimental contaminant concentrations.

1.3 Recovery procedures

Only 2 of the 8 studied contaminants (table 1.2.1) did not lead to recovery after the injection was stopped (Ca^{2+}, bromomethane). For Ca^{2+}, 2 in situ recovery methods, which are the most relevant for these applications, were investigated. Cell operation at a low cell voltage sufficient to reach the limiting current density to push the cations near the cathode and favor ion exchange with the product water protons was not effective (not shown). The circulation of an acid solution within the cell was more effective and lead to the removal of a large fraction of the accumulated salt deposit by dissolution (figure 1.3.1). However, membrane/electrode assembly cross-sections revealed that the interior of the gas diffusion layer still contained salt deposits (figure 1.3.2).

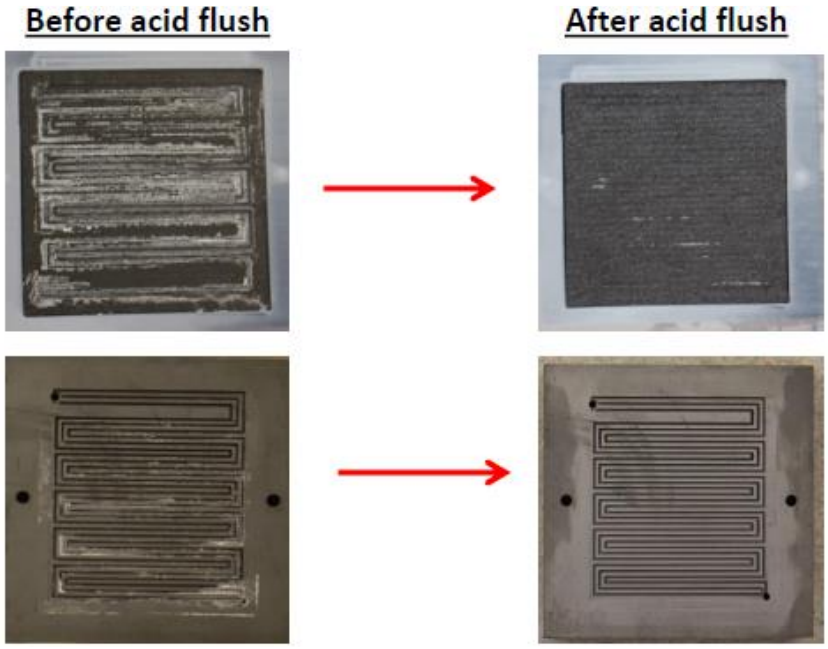

Figure 1.3.1. $CaSO_4$ salt deposits on a gas diffusion layer (top, left) and a bipolar plate (bottom, left). An *in situ* exposure to a 100 mM H_2SO_4 solution for 3 h is sufficient to remove most salt deposits from the gas diffusion electrode (top, right) and the bipolar plate (bottom, right).

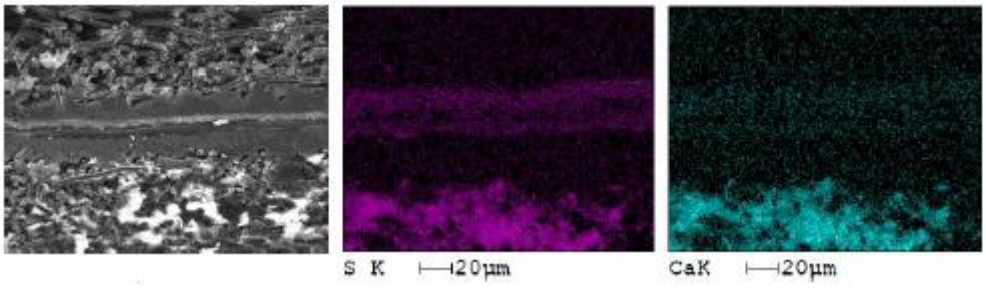

Figure 1.3.2. The membrane/electrode assembly cross section as observed by scanning electron microscopy (left) shows, from the image top to the bottom, the anode gas diffusion layer, the catalyst coated membrane with its support in the middle and the cathode gas diffusion layer with salt deposits in white. The S (center) and Ca (right) energy dispersive X-ray spectroscopy maps correlate with the cathode salt deposits.

The cell performance only partially recovered and mostly in the mass transport regime at high current densities (figure 1.3.3). The partial recovery was ascribed to the hydrophilic salt deposits removal favoring liquid water accumulation in the gas diffusion electrode and impeding oxygen transport. Presumably, a significant amount of Ca^{2+} is still present in the ionomer or membrane (ion exchange with the acid solution protons does not take place or its extent is partial) and negatively affects cell performance even if the concentration is below the detection limit of the energy dispersive x-ray spectrometer (figure 1.3.2).

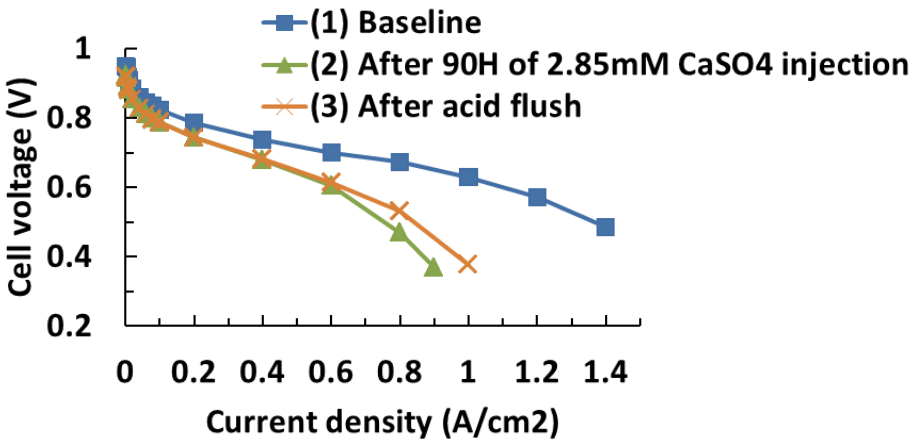

Figure 1.3.3. Polarization curves obtained during and after different *in situ* contamination stages.

For bromomethane, recovery was attempted after operating the cell at a constant cell voltage (figure 1.3.4, left) which led to an almost complete loss in current density. Bromide ions produced by bromomethane hydrolysis were identified as a species strongly adsorbing on the surface of the Pt catalyst. It was deduced that desorption of these ions which takes place at a low cathode potential followed by cell operation favoring the formation of liquid water drops would remove Br^- ions by dissolution and entrainment.

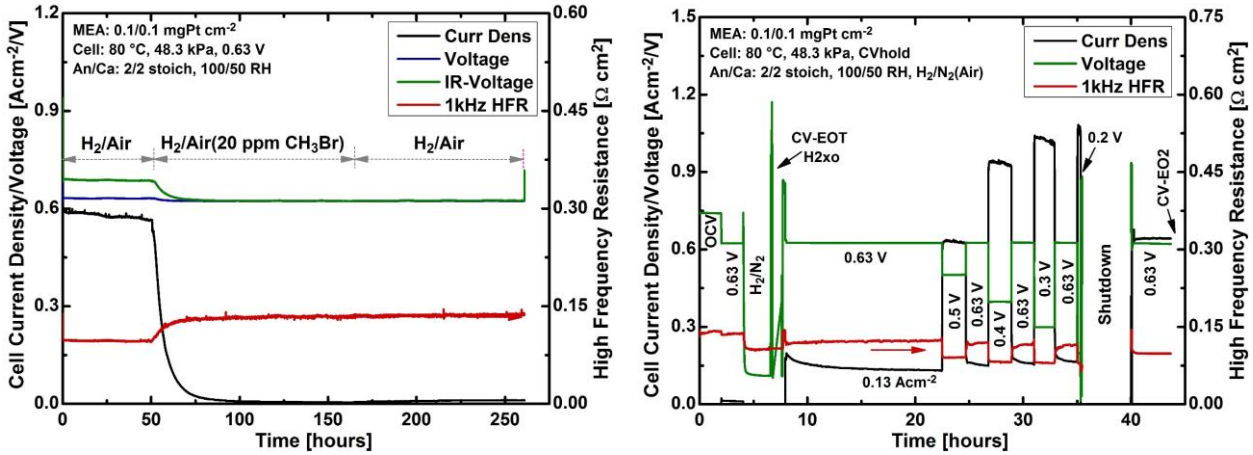

Figure 1.3.4. Bromomethane contamination test (left) and subsequent variable cell voltage periods used to recover the initial cell performance (right). The beginning of the time scale on the right figure corresponds to the end of the time scale on the left figure.

Figure 1.3.4, right shows that the original current density of ~0.6 A cm^{-2} is restored at 40-44 h after a low cathode potential period at ~7-8 h induced by operating with N_2 rather than air and a low cell voltage operation period at ~35 h to maximize the current density and water production. The method effectiveness was confirmed by operating a second cell which led to the same loss in performance (figure 1.3.5, top, left). However, Br^- desorption and removal was achieved by changing the oxidant gas composition to obtain a low cathode potential (operating with H_2 rather than air) and favoring the production of liquid water by lowering the cell temperature (decrease in water vapor saturation pressure) and injecting more water in vapor or liquid form. The cell current density was recovered to ~0.5 A cm^{-2} at 58-68 h, figure 1.3.5, bottom). The recovery was more extensive after polarization curves with a current density increase from ~0.5 to ~0.6 A cm^{-2} (figure 1.3.6). For both cells contaminated with bromomethane, the current density recovery at 0.63 V exceeded 90 %.

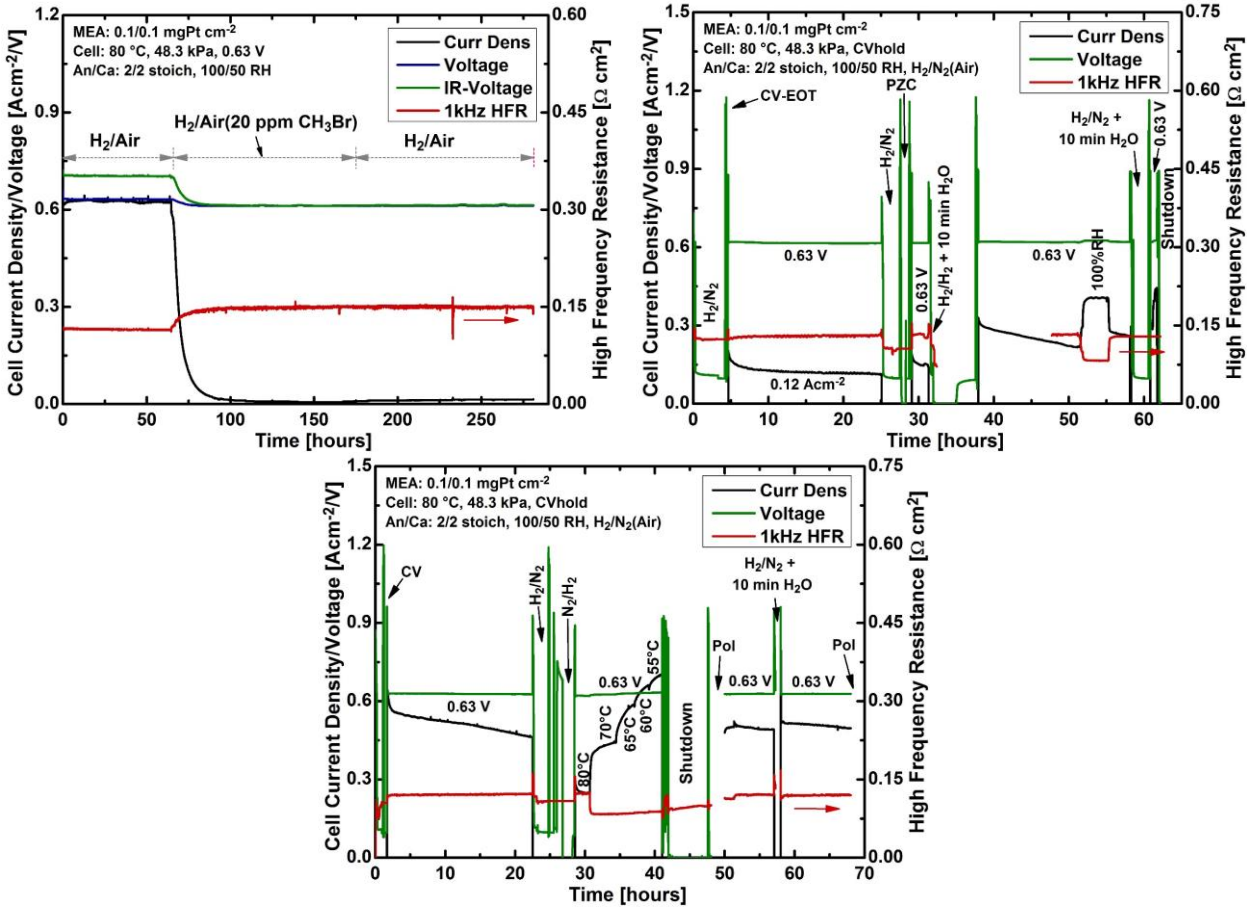

Figure 1.3.5. Bromomethane contamination test (top, left) and subsequent variable compartment gas compositions, humidification and temperature periods used to recover the initial cell performance (top, right and bottom). The beginning of the time scale on the top, right figure corresponds to the end of the time scale on the top, left figure. The beginning of the time scale on the bottom figure corresponds to the end of the time scale on the top, right figure.

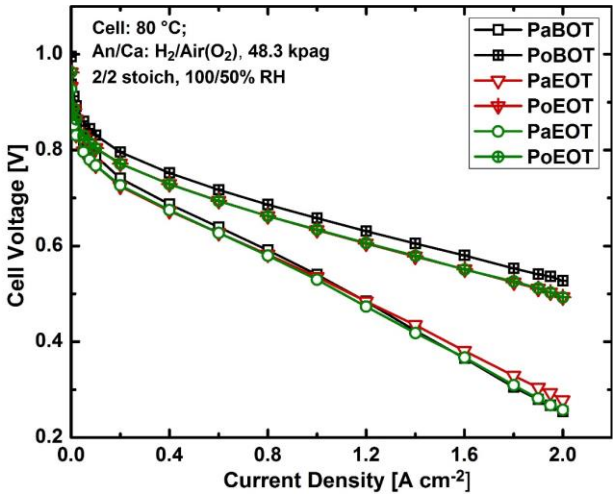

Figure 1.3.6. Air and oxygen polarization curves before and after the variable cathode compartment gas compositions, humidification and temperature periods used to recover the bromomethane contamination loss. Pa and Po respectively refer to air and oxygen polarization curves at the beginning (BOT) and end (EOT) of the tests.

2 Project activities

Project tasks and objectives are listed in table 2.1. Tasks 1 and 2 are detailed in this section (section 2) whereas tasks 3 and 4 are part of subsequent mandatory sections, respectively sections 3.5 (task 3) and sections 3.1 and 3.2 (task 4). Table 2.2 contains the 4 project milestones and associated tasks.

Table 2.1. Project tasks and objectives.

Task	Objectives
1.1 Impurity Identification and Screening	1. Identify potential contaminants originating from air pollution and road side environments. 2. Screen and prioritize impurities based on degradation of cell performance or chemical interaction with the MEA.
1.2 Contaminant Impact	1. Quantify impact of contaminant and contaminant mixtures on fuel cell performance and durability at different operating conditions. 2. Quantify all reaction products to aid identification of reaction and adsorption processes. 3. Quantify spatial variability of contaminant processes using segmented cell.
1.3 Cell Recovery	Quantify cell recovery resulting from removal of contaminant and change of operating conditions.
1.4 *Ex situ* Analysis	Characterize changes in catalyst, MEA and GDL structure resulting from exposure to contaminant and contaminant mixtures.
2.1 Real World Operation	Characterize effect of contaminant at 'real world' operating conditions.
2.2 Mitigation Strategies	Explore operating strategies and novel techniques to mitigate contaminant effects.
3.0 Model Development and Application	1. Validate and use empirical performance models to quantify and understand spatial variability of contaminant effects in PEMFCs. 2. Develop and validate mechanistic models that quantify material degradation. 3. Establish the relationship between those mechanisms and models and the loss of PEMFC performance.
4.0 Outreach	Conduct outreach activities to disseminate critical data, findings, models, and relationships that describe the effects of airborne contaminants on PEMFC performance and durability.

Table 2.2. Project milestones.

Year	Milestone
1	Prioritize a group of ~10 airborne contaminants of relevance to stationary and automotive fuel cell applications based on (tasks 1.1.1 and 1.1.2) ⇨ performance impact (screening results). ⇨ occurrence (literature results, industry exchange).
2	Quantify performance loss for at least 4 different contaminants under various operating conditions (tasks 1.2.1 and 1.3).
3	Quantify spatial variability of performance loss for at least 4 different contaminants. Identify principal poisoning mechanism for same (tasks 1.2.2, 1.2.3 and 1.4).
4	Demonstrate successful mitigation of the impact of the most important 4 airborne contaminants (task 2.2).

2.1 Contaminant down selection (milestone 1, tasks 1.1.1 and 1.1.2)

Initial efforts focused on contaminant identification. This step was followed by the creation of qualitative criteria and their use to reduce the number of contaminant screening tests to a manageable level. Quantitative criteria were also derived to further restrict the number of contaminants subjected to extensive characterization tests.

2.1.1 *1st tier contaminant identification and validation*

Contaminants were identified primarily by reviewing the Environmental Protection Agency information, consulting the fuel cell community, and analyzing road side soil, internal combustion engines and fuel cell filters' samples. The Environmental Protection Agency yielded a list of more than 200 species in air. As for solid species, samples were collected from several areas of the northern hemisphere (figure 2.1.1) and vehicle air intake filters. An analysis example for a filter sample is illustrated in figure 2.1.2. Table 2.1.1 summarizes sample analyses which reveals a significant number of additional contaminants.

Figure 2.1.1. Distribution of road side soil samples.

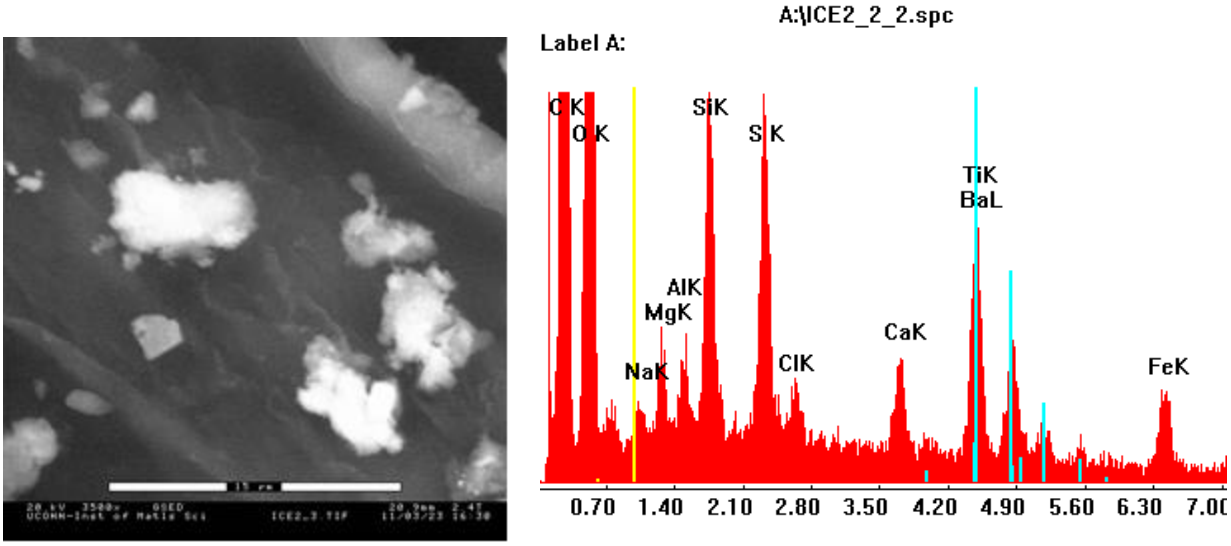

Figure 2.1.2. Analysis of a typical filter specimen. Scanning electron microscopy image (left) and energy dispersive x-ray spectrum (right). This is the only spectrum in which barium, an element commonly used in automobile ignitions and engine hoods, is seen.

Airborne species can easily bypass the air intake filter because slippage occurs and the filter may eventually be saturated or fail (hole formation) and contaminate the fuel cell. Although soil and filter samples are solid and are more easily captured by the air intake filter, contaminants may still reach the fuel cell if the particles are sufficiently small or the filter fails (hole formation). In this case, the presence of product liquid water within the fuel cell can leach solids with the creation of ions. Therefore, even if an air filter provides a preventive measure, it is still probable that a fuel cell will be contaminated. It is thus important to understand the tolerance of a fuel cell to specific contaminants (filter requirements) and contamination mechanisms to devise recovery procedures or develop more resistant components. With these approaches, a more robust fuel cell system would be achieved.

In view of the large number of species and limited resources, down selection procedures are essential to focus activities toward the most relevant contaminants. A two-step approach used for an ecological risk assessment [2] was adapted. As a first step, qualitative criteria are used to decrease the number of species which resulted in a list of 1st tier contaminants. Different criteria were used for airborne species and ions (table 2.1.2). As a second step, quantitative criteria are used to assess experimental results obtained from the contaminant list that was reduced with the qualitative criteria which resulted in a list of 2nd tier contaminants. In this manner, the two-step approach is cost effective because without qualitative criteria all contaminants would need experimental measurements and substantial resources, and without quantitative criteria the effects of all identified contaminants would remain undetermined. It is noted that 2 criteria were common to both classes of contaminants (table 2.1.2) and were introduced to be responsive to the fuel cell community and avoid duplication of efforts by avoiding contaminants that have previously been documented. Finally, quantitative criteria were initially derived based on the behavior of airborne contaminants. However, these were not applicable to ion contaminants because their behavior was different. In particular, steady states for a step change in contaminant concentration were generally not observed. Therefore, for ions, the cell degradation rate was

favored to down select species for detailed studies (section 3.1, references J1 and J3 for more details about the down selection procedure).

Table 2.1.1. Road side contaminants observed from vehicular air filters, fuel cell air filters and road side soil samples.

Elements observed		Valence	ICE filter analysis	UTC filter analysis	Road side samples
Cations	Al	+3	√		√
	Fe	+2, +3	√	√	
	Ni	+2	√		
	Cr	+3	√	√	
	Na	+1	√	√	
	Ba	+2	√	√	
	Ca	+2	√	√	√
	Mg	+2	√		√
	Cu	+2		√	
	Sn	+2	√		
	K	+1	√	√	
	Mn	+2		√	
	Zn	+2		√	
	V	+3		√	
	Tl	+1		√	
	Si	+4	√		√
Anions	P as PO_4^{-3}	-3	√		
	Cl	-1	√	√	√

Table 2.1.2. Qualitative criteria by class used to reduce the number of contaminants.

Airborne contaminants	Foreign ions
• Atmospheric presence at a significant level • Expectation of reactivity within the fuel cell • Absence of recorded data • Largest range in chemical functionalities • Compound toxicity • Suggestions given by industry and research institutions	• Roadside and, air and water filter samples • Encounter likeliness based on usage and probable future usage • Valence state • Absence of recorded data • Solubility, toxicity and availability • Interest of industry members

Table 2.1.3 summarizes the 21 airborne contaminants that were down selected after the use of the qualitative criteria. Methyl methacrylate and 2,2-bis(4-hydroxyphenyl)propane were suggested by Nuvera whereas 1,1-difluoroethane and 1,1,1,2-tetrafluoroethane were suggested by the Fuel Cell Tech Team. Table 2.1.4 summarizes the 7 cations and 4 anions that were down selected after the use of the qualitative criteria. In view of their different physical state, ion charge and solubility were important considerations that were not relevant for airborne species.

The following organizations were contacted to validate tables 2.1.3 and 2.1.4 contaminants: Air Liquide, Air Products, Argonne National Laboratory (ANL), Automotive Fuel Cell Cooperation (AFCC), California Fuel Cell Partnership (CFCP), California Stationary Fuel Cell Collaborative

(CSFCC), Enviromental Protection Agency (EPA), Fuel Cell and Hydrogen Energy Association (FCHEA), Japan Automobile Research Institute (JARI), Linde, Los Alamos National Laboratory (LANL), National Aeronautics and Space Administration (NASA), National Center for Atmospheric Research (NCAR), National Institute of Standards and Technology (NIST), National Renewable Energy Laboratory (NREL), Naval Research Laboratory (NRL), Nuvera, Praxair, SAE International.

Table 2.1.3. Down selected airborne contaminants and some of their characteristics. Reprinted and reformatted with permission from *J. Electrochem. Soc.*, **161**, F280 (2014). Copyright 2013, The Electrochemical Society.

Contaminants			**Annual maximum concentration (ppm carbon)[a]**			**Source**	**OSHA PEL (ppm)[b]**
Hydrocarbon functionality	**Common name**	**Formula**	**1 h average**	**3 h average**	**24 h average**		
N/A	Ozone	O_3	0.197 ppm			Chemical manufacture reagent, bleaching agent, disinfectant	0.1
Alcohol	Iso-propanol	$CH_3CH(OH)CH_3$	0.65 (indoor max) 0.08 (indoor mean)			Cleaning fluid and solvent	400
Aldehyde	Acetaldehyde	CH_3CHO	0.022 (indoor max) 0.007 (indoor mean)			Chemical manufacture precursor	200
Alkane	Butane	C_4H_{10}	1.768	0.364	0.265	Fuel, industrial feedstock, propellant	800
Alkene	Propene	C_3H_6	0.625	0.0819	0.102	PP synthesis precursor and petrochemical feedstock	Not applicable
Alkyne	Acetylene	C_2H_2	0.117	0.0376	0.0386	Welding fuel and chemical manufacture precursor	Not applicable
Aromatic	Toluene	$C_6H_5CH_3$	0.296	0.0545	1.17	Solvent and industrial feedstock	200
Ester	Methyl acetate	CH_3COOCH_3				Solvent and industrial intermediate	200
	Methyl methacrylate	$CH_2CCH_3COOCH_3$			0.00267	PMMA synthesis precursor	100
	Vinyl acetate	$CH_2CHOOCCH_3$			0.102	PVA synthesis precursor	Not applicable
Ether	Methyl tert-butyl ether	$(CH_3)_3COCH_3$		0.0017	0.0192	Gasoline additive and solvent	Not applicable
Halocarbon	1,1-difluoroethane	CH_3CHF_2			$1x10^{-5}$ [c]	Refrigerant	Not available
	1,1,1,2-tetrafluoroethane	CH_2FCF_3			$6x10^{-5}$ [c]	Refrigerant	Not available
	Bromomethane	CH_3Br			0.0066	Solvent and chemical manufacture precursor	Not applicable
	Chlorobenzene	C_6H_5Cl			0.0026	Commodity production intermediate	75
	Dichloromethane	CH_2Cl_2		$8.7x10^{-4}$	0.124	Paint and degreaser solvent	25
	Trichlorofluoromethane	CCl_3F			$2.7x10^{-4}$ [c]	Former refrigerant	1000
Ketone	Acetone	CH_3COCH_3		0.190	0.2022	Solvent and polymer synthesis precursor	1000
Nitrile	Acetonitrile	CH_3CN			3.1	Butadiene production solvent	40
Phenol	2,2-bis(4-hydroxyphenyl)propane	$(HOC_6H_4)_2(CH_3)_2C$			17 pg l^{-1}	Epoxy resin and plastic precursor	Not available
Polycyclic aromatic	Naphthalene	$C_{10}H_8$			0.05	Mothball primary ingredient	10

[a] Unless otherwise noted. ppm carbon is the volume concentration in ppm multiplied by the number of carbon atoms in the compound.

[b] OSHA: occupational safety and health administration, PEL: permissible exposure limit (8 h time weighted average).

[c] Yearly average in ppm in the atmosphere.

Table 2.1.4. Down selected cation contaminants and some of their characteristics.

	Element	Common Valence	Common Occurence	Source
Cations	Aluminum	+3	$AlCl_3$, $(AlO_x(OH)_{3-2x})$, $Al(OH)^{4-}$	Electrical Insulation, Production of Metals, and Cement
	Barium	+2	$BaSO_4$, $BaCO_3$	Automobile Ignitions, Tires, Glassmaking, Rat Poison, Fluorescent Lamps
	Calcium	+2	$Ca(OH)_2$, $CaCO_3$	Tires, Concrete, Fertilizer, Glass, Road Paints, De-Icing Fluids
	Magnesium	+2	$(CaMg)(CO_3)_2$, $MgCO_3$, $Mg(OH)_2$, $KMgCl_3{\cdot}6(H_2O)$, $Mg_3Si_4O_{10}(OH)_2$, $(Mg,Fe)_2SiO_4$	Wheels, Electronic Devices, Electrical Insulation, Production of Metals, and Cement
	Potassium	+1	$KAlSi_3O_8$, Granite, $(KCl{\cdot}MgCl_2{\cdot}6(H2O))$, $(MgSO_4{\cdot}KCl{\cdot}3H_2O)$, $(MgSO_4{\cdot}K_2SO_4)$, KCl	Hydrogen Generated by Alkaline Electrolysis, Trace Compound in Sea Salt
	Sodium	+1	NaCl, Amphibole, Zeolite	Sea Salt
	Titanium	+4	TiO_2, $FeTiO_3$, $CaTiO_3$,$CaTiSiO_5$	High Strenth Steel Alloys, Paints
Anions	Carbonate	-2	Na_2CO3, $MgCO_3$, K_2CO_3, $CaCO_3$	Common Natural Occurrence
	Chloride	-1	NaCl, KCl, $CaCl_2$, $MgCl_2$	Salt
	Hydroxide	-1	NaOH, KOH, Alkali Metals	Common Natural Occurrence
	Phosphate	-2	Phosphate Minerals, $Ca_5(PO_4)_3(F,Cl,OH)$	Fertilizer

2.1.2 *2nd tier airborne contaminants*

All down selected contaminants (tables 2.1.3 and 2.1.4) were injected for a temporary amount of time in the air stream of a single Fuel Cell Technologies fuel cell or a modified version (50 cm^2 active area for airborne contaminants, 25 cm^2 active area for foreign ions) using a common membrane/electrode assembly (GORE PRIMEA M715 membrane/electrode assemblies, cathode/anode, 0.4 or 0.1/0.4 mg Pt cm^{-2} (50 % Pt/C), 18 µm GORE-SELECT membrane, and SGL 25 BC gas diffusion layers unless otherwise noted). Operating conditions differed to accommodate the injection of a dilute aqueous salt solution (as opposed to an airborne contaminant). Ions are generally more benign than airborne contaminants because a liquid water path is needed for their transport to the cathode. From that standpoint, the presence of a hydrophobic gas diffusion layer readily offers an effective barrier.

Contaminant concentrations were set above atmospheric values (table 1.2.1) to accelerate degradation and minimize resource usage. For example, figures 2.2.2, top, 2.2.3, top, left, and 2.2.5, top demonstrate that an increase in contaminant concentration hasten cell voltage degradation. Figure 2.1.3, bottom, left illustrates that a steady state was only reached during bromomethane contamination after ~60 h at a 50 ppm concentration (0.0066 ppm in ambient air). Sections 2.4.1 and 2.4.3 contain data obtained with contaminant concentrations closer to those in ambient air (table 1.2.1) and lower than those employed for contaminant screening tests (table 2.1.5).

Figure 2.1.3 illustrates the variety of behaviors resulting from airborne contaminants (section 3.1, reference J3 for all airborne contaminants down selection data). The effect can be negligible or large, recoverable, partially recoverable or supra-recoverable. Contamination and recovery time scales also significantly vary. Such a variety of parameters (performance lost and recovered, time scales) complicates contaminant down selection suggesting the need to develop quantitative criteria consistently applied for selection and minimize qualitatively based decisions.

Airborne contaminants predominantly behave as illustrated in figure 2.1.4. Upon injection of the contaminant, the cell performance drops until a steady state is reached after a variable amount of time dependent on operating conditions. After the contamination injection is interrupted, the initial cell performance is partially, fully or supra- recovered. Points a and c correspond to the measured voltage at the time the contaminant is injected and injection is terminated. Points b and d are defined by the intersection of two asymptotes at the beginning and end of the contamination and recovery periods. Two empirical methods were considered for contaminant ranking and rely on these 4 time/voltage pairs (points a to d). Method 1 relies on the combination of steady state contamination and irrecoverable performance losses, corresponding time scales and contaminant concentration. Method 2 relies on the combination of the energy lost to contamination and regained during self-recovery:

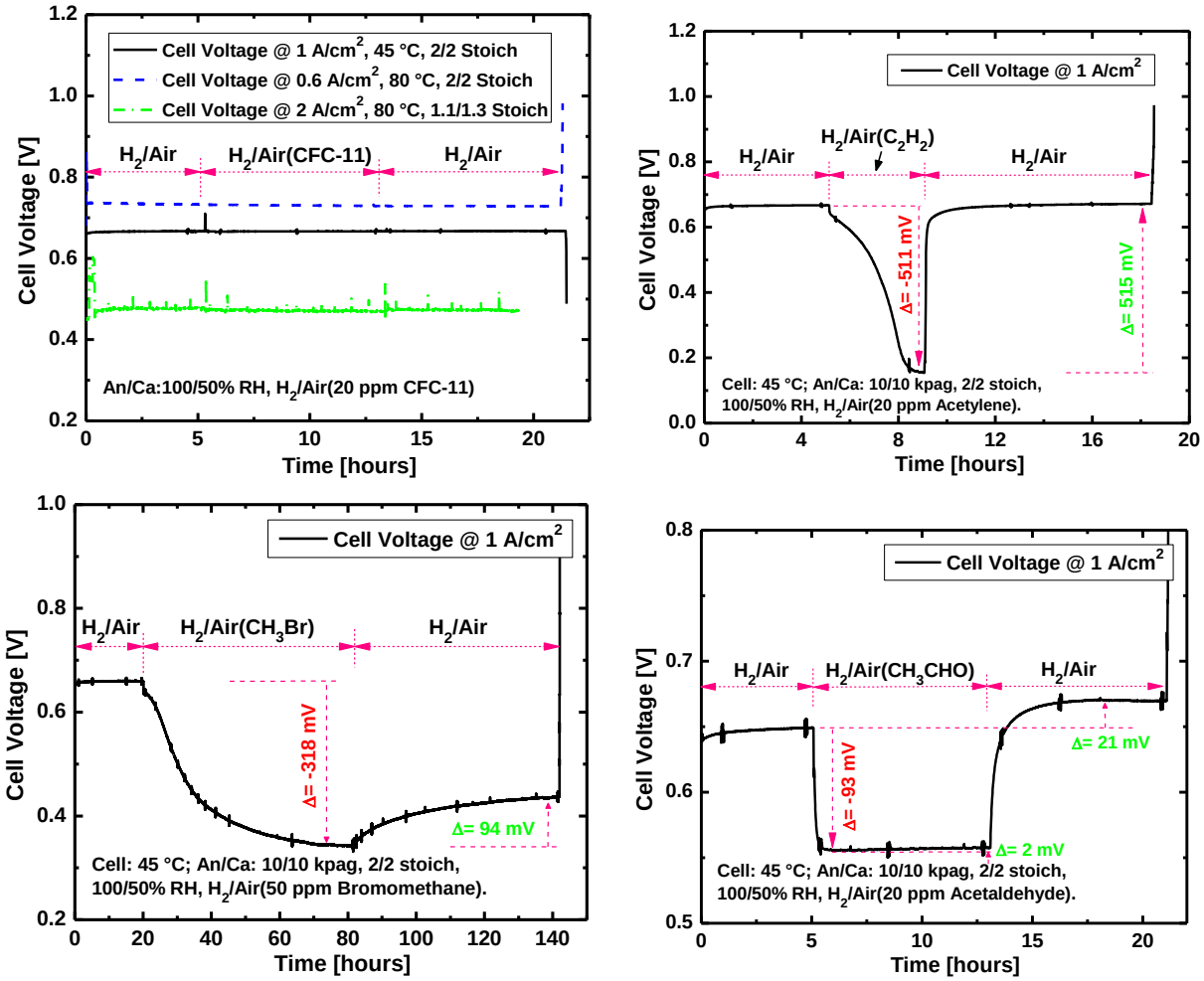

Figure 2.1.3. Different fuel cell voltage transients resulting from a temporary airborne contaminant injection in the air stream. No effect (top, left), large effect but recoverable performance (top, right), large effect but partly recoverable performance (bottom, left), large effect but supra-recoverable performance (bottom, right). Top, left (1 A cm^{-2} curve only), top, right and bottom figures reprinted and reformatted with permission from *J. Electrochem. Soc.*, **161**, F280 (2014). Copyright 2013, The Electrochemical Society.

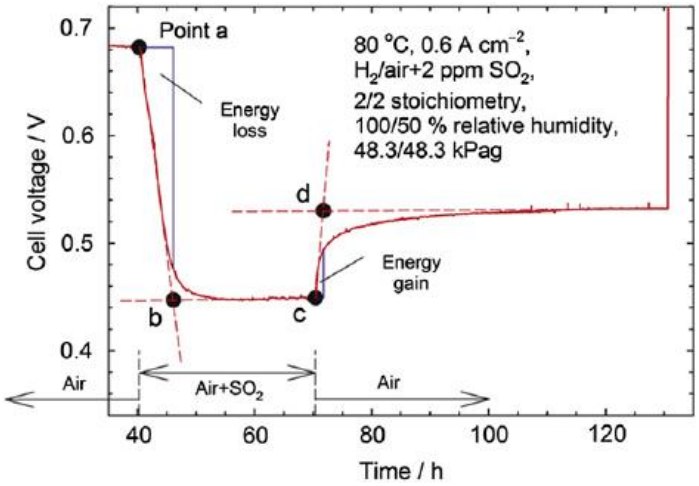

Figure 2.1.4. Graphical representation of the two methods' parameters used to prioritize contaminants. Reprinted from International Journal of Hydrogen Energy, Volume 37, Jean St-Pierre, Yunfeng Zhai, Michael Angelo, Quantitative ranking criteria for PEMFC contaminants, Pages 6784-6789, Copyright (2012), with permission from Elsevier (http://www.sciencedirect.com/science/journal/03603199?sdc=1).

$$SC_1 = \frac{(V_a - V_b)^2 (V_a - V_d)(t_d - t_c)}{c_{\text{contaminant}} (V_d - V_c)(t_b - t_a)} \quad (2.1.1)$$

$$SC_2 = \int_{t_a}^{t_b} (V_a - V)dt \Big/ \int_{t_c}^{t_d} (V - V_c)dt \quad (2.1.2)$$

where SC represents a selection criteria (V^2 ppm^{-1} or dimensionless), V_i the cell voltage at point i (V), t_i the time at point i (h), $c_{contaminant}$ the contaminant concentration in the dry reactant stream (ppm), and V the cell voltage (V). Additional derivation details for equations 2.1.1 and 2.1.2 are given in section 3.1, references J1 and J3.

Equations 2.1.1 and 2.1.2 parameters are listed in table 2.1.5 for the 1st tier airborne contaminants and 2 combinations of cathode and anode gas inlet relative humidities (section 3.1, references J3).

Larger SC_1 and SC_2 values generally mean more significant performance losses. Table 2.1.6 shows the resulting contaminant rankings (section 3.1, reference J3). Generally, the selection criteria values are not very sensitive to relative humidity. The range in values is larger for SC_1 (more sensitive parameter). Only 2 of the top 5 contaminants (highlighted in red) are the same for SC_1 and SC_2 (bromomethane, naphthalene). For contaminants that led to a recovery exceeding the initial loss (acetaldehyde, propene, highlighted in green), rankings either correspond to low SC_1 values or are scattered over the SC_2 range. Interestingly, SC_2 is not only useful to pinpoint contaminants that have a large negative effect on performance, but also others that lead to a recovery exceeding the initial loss (propene). These seemingly beneficial contaminants are a good example of the envisaged use of both selection criteria as a quantitative measure to guide decisions. A strict application of SC_1 would preclude any further interest. However, acetaldehyde and propene unusual behavior may hide some permanent performance

benefit. For the reason that SC_2 is able to identify contaminants that lead to a supra-recoverable effect, and also because SC_2 is less sensitive to the change in operating conditions (section 3.1, reference J1), it was used to create the second tier list. As a result, all contaminants with highlighted SC_2 values were selected with the exception of acetone (low probability of fuel cell exposure). Rather, acetonitrile was added to the list because it was the only contaminant that led to ohmic losses. In summary, the following airborne contaminants were selected for more detailed studies: acetonitrile (nitrile), acetylene (alkyne), bromomethane (halocarbon), iso-propanol (alcohol), methyl methacrylate (ester), naphthalene (aromatic), propene (alkene).

Table 2.1.6. 2nd tier down selection criteria values for 1st tier down selected airborne contaminants. Reprinted and reformatted with permission from *J. Electrochem. Soc.*, **161**, F280 (2014). Copyright 2013, The Electrochemical Society.

Contaminant[a]	***SC*$_1$ (V^2 ppm^{-1})**		***SC*$_2$**	
	100/50[b]	**0/0**[b]	**100/50**[b]	**0/0**[b]
1,1-difluoroethane[c]	7.23×10^{-4}	3.74×10^{-4}	0.0259	0.0682
1,1,1,2-tetrafluoroethane[d]	2.16×10^{-4}	1.88×10^{-4}	0.0413	0.00532
2,2-bis(4-hydroxyphenyl)propane[e]	No effect	No effect	No effect	No effect
Acetaldehyde	-2.35×10^{-4}	-1.03×10^{-4}	0.214	0.409
Acetone	-2.86×10^{-7}	1.24×10^{-6}	6.75	6.59
Acetonitrile	5.78×10^{-3}	9.51×10^{-3}	0.0575	0.0410
Acetylene	3.13×10^{-6}	3.86×10^{-6}	30.6	16.5
Bromomethane	4.04×10^{-3}	7.37×10^{-3}	7.57	8.03
Butane	1.63×10^{-6}	-	0.188	-
Chlorobenzene	1.57×10^{-2}	4.09×10^{-2}	0.165	0.0978
Dichloromethane	No effect	No effect	No effect	No effect
Iso-propanol	-2.55×10^{-7}	1.54×10^{-4}	17.8	0.1
Methyl acetate	1.97×10^{-6}	-	1.05	-
Methyl methacrylate	1.44×10^{-5}	1.32×10^{-4}	4.86	3.94
Methyl tert-butyl ether	6.69×10^{-6}	4.62×10^{-4}	2.05	0.260
Naphthalene	∞	∞	∞	∞
Ozone	5.38×10^{-4}	4.68×10^{-4}	0.149	0.188
Propene	-3.08×10^{-5}	-6.55×10^{-5}	32.1	1.05
Toluene	5.38×10^{-4}	1.34×10^{-3}	0.349	0.247
Trichlorofluoromethane[f]	No effect	8.76×10^{-4}	No effect	0.277
Vinyl acetate	-4.42×10^{-5}	-1.16×10^{-4}	1.19	0.879

[a] 20 ppm contaminant concentration with the exception of bromomethane (50 ppm), bisphenol A (0.1 ppm), butane (100 ppm) and ozone (95/83 ppm for wet/dry conditions).
[b] Anode/cathode relative humidity (%).
[c] Also referred to as HFC-152a.
[d] Also referred to as HFC-134a.
[e] Also referred to as bisphenol A.
[f] Also referred to as CFC-11.

Table 2.1.5. 2nd tier down selection criteria parameter values for 1st tier down selected airborne contaminants. Reprinted and reformatted with permission from *J. Electrochem. Soc.*, **161**, F280 (2014). Copyright 2013, The Electrochemical Society.

Contaminant[a]	$V_a - V_b$ (V)		$V_a - V_d$ (V)		$V_d - V_c$ (V)		$t_b - t_a$ (h)		$t_d - t_c$ (h)		$\int_{t_a}^{t_b}(V_a - V)dt$ (Vh)		$\int_{t_c}^{t_d}(V - V_c)dt$ (Vh)	
	100/50[b]	**0/0**[b]	**100/50**[b]	**0/0**[b]	**100/50**[b]	**0/0**[b]	**100/50**[b]	**0/0**[b]	**100/50**[b]	**0/0**[b]	**100/50**[b]	**0/0**[b]	**100/50**[b]	**0/0**[b]
1,1-difluoroethane[c]	0.147	0.188	0.008	0.005	0.215	0.229	1.01	1.76	18.2	17.1	0.0631	0.2	2.44	2.93
1,1,1,2-tetrafluoroethane[d]	0.025	0.022	0.01	0.007	0.015	0.014	0.14	0.09	1.45	1.4	0.0004	0.00005	0.00968	0.0094
2,2-bis(4-hydroxyphenyl)propane[e]	No effect	No effect	No effect	No effect	No effect	No effect	No effect	No effect	No effect	No effect	No effect	No effect	No effect	No effect
Acetaldehyde	0.093	0.106	–0.022	–0.008	0.113	0.114	0.14	0.18	0.39	0.47	0.00583	0.00895	0.0272	0.0219
Acetone	0.012	0.02	–0.001	0.004	0.013	0.017	1.49	2.58	0.77	0.68	0.0101	0.0457	0.0015	0.00693
Acetonitrile	0.444	0.447	0.019	0.022	0.43	0.436	1.6	1.15	21.2	21.7	0.407	0.299	7.07	7.29
Acetylene	0.499	0.496	0.004	0.004	0.509	0.502	3.13	2.03	0.1	0.08	0.57	0.46	0.0186	0.028
Bromomethane	0.306	0.301	0.25	0.314	0.068	0.053	19.6	19.5	11.5	13.4	2.82	3.24	0.373	0.403
Butane	0.01	-	0.006	-	0.008	-	0.35	-	0.76	-	0.00145	-	0.00772	-
Chlorobenzene	0.579	0.563	0.049	0.107	0.551	0.491	0.33	0.26	3.48	3.08	0.0976	0.0699	0.592	0.715
Dichloromethane	No effect	No effect	No effect	No effect	No effect	No effect	No effect	No effect	No effect	No effect	No effect	No effect	No effect	No effect
Iso-propanol	0.01	0.022	–0.001	0.007	0.01	0.011	2.33	0.1	1.19	1	0.0244	0.0007	0.00137	0.007
Methyl acetate	0.005	-	0.003	-	0.004	-	0.50	-	1.05	-	0.001	-	0.00095	-
Methyl methacrylate	0.455	0.472	0.004	0.025	0.469	0.457	0.55	0.6	0.09	0.13	0.112	0.132	0.023	0.0336
Methyl tert-butyl ether	0.044	0.034	0.006	0.016	0.05	0.028	1.39	0.07	0.8	0.98	0.0329	0.00338	0.016	0.013
Naphthalene	0.51	0.51	0.575	0.579	0	0	0.41	0.36	∞	∞	0.0958	0.078	0	0
Ozone	0.136	0.144	0.047	0.042	0.116	0.122	4.07	4.05	27.8	22	0.263	0.298	1.76	1.59
Propene	0.204	0.226	–0.02	–0.016	0.216	0.23	0.25	0.19	0.04	0.07	0.0253	0.0206	0.0008	0.0196
Toluene	0.477	0.472	0.005	0.01	0.525	0.55	0.28	0.34	1.39	2.25	0.0683	0.082	0.196	0.332
Trichlorofluoromethane[f]	No effect	0.015	No effect	0.005	No effect	0.007	No effect	0.01	No effect	1.09	No effect	0.00119	No effect	0.0043
Vinyl acetate	0.146	0.155	–0.007	–0.013	0.152	0.154	0.2	0.21	0.18	0.24	0.0153	0.0189	0.0128	0.0215

[a] 20 ppm contaminant concentration with the exception of bromomethane (50 ppm), bisphenol A (0.1 ppm), butane (100 ppm) and ozone (95/83 ppm for wet/dry conditions).

[b] Anode/cathode relative humidity (%).

[c] Also referred to as HFC-152a.

[d] Also referred to as HFC-134a.

[e] Also referred to as bisphenol A.

[f] Also referred to as CFC-11.

2.1.3 *2nd tier road side contaminant*

Table 2.1.1 was established on the basis of solid filter and road side samples. However, it was envisaged that contaminants in solid form would have a minimal impact on the fuel cell due to the gas diffusion layer barrier. Thus, salts soluble in water were used to test the impact of these elements and favor ion exchange with the ionomer and/or membrane (table 2.1.4). Therefore, the measured contaminant effects are considered as worse case scenarios. A test station was modified for the injection of the salt solutions which included a nebulizer and a peristaltic pump (figure 2.1.5).

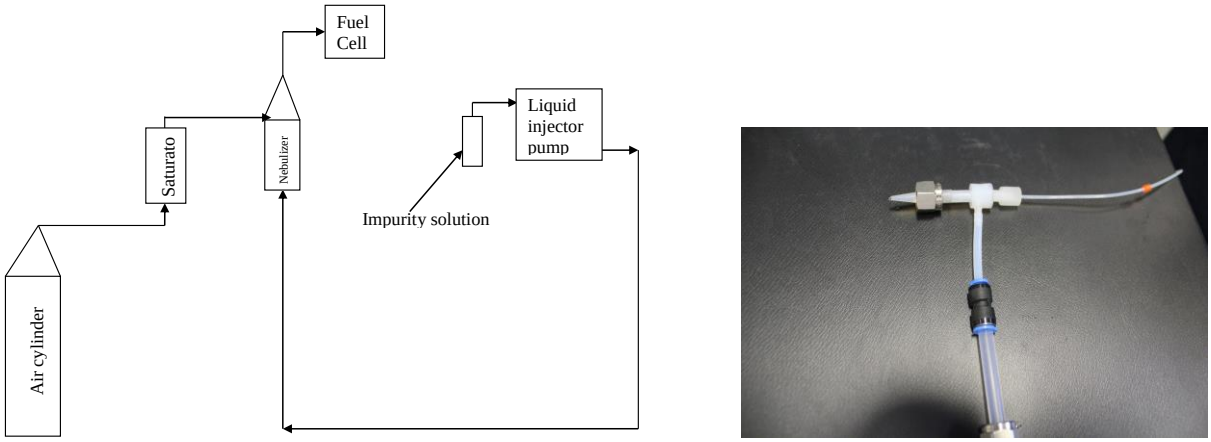

Figure 2.1.5. Schematic diagram of the test station modifications for the injection of salt solutions (left). Nebulizer (right).

Additionally, early attempts to contaminate fuel cells revealed a smaller (<20 % decrease in cell voltage) and slower impact than gaseous contaminants (figure 2.1.6, left). As a result, several operating conditions were modified to facilitate the transfer of water from the cathode to the anode side (higher cathode relative humidity and pressure) over the entire active area (high cathode and anode stoichiometries) to ensure that foreign cations would reach the ionomer and/or membrane for ion exchange (figure 2.1.6, right). Such changes in operating conditions were assumed to favor the presence of a liquid water path between the flow field channels and the ionomer and/or membrane for ion transport. However, as a result of these changes, the identification of failure modes associated with unmodified conditions was precluded.

Furthermore, early tests also revealed that contamination by foreign cations is more complicated than originally anticipated (water management dependent, sections 2.3 and 2.5). Therefore, the first tier list of foreign cations and anions (table 2.1.4) was reduced to a second tier list containing a single salt candidate: calcium sulfate. Calcium has seldom been studied and is ubiquitous as a road de-icing agent. The complete list of 2nd tier contaminants, those that were selected for detailed studies, is summarized in table 2.1.7.

For brevity, only a fraction of the screening data, which also include Ba, Fe and Mg salts, is shown in figures 2.1.6 and 2.1.7. It is noted that the fuel cells do not reach a steady state even after several tens of hours after contaminant injection, which precludes an analysis based on the parameters defined by equations 2.1.1 and 2.1.2 (figure 2.1.4). However, this situation did not prevent the selection of a second tier foreign cation which was rather based on qualitative

grounds as mentioned above. It was hoped that results from tasks 1.2 and 1.3 (section 2.2, effects of operating conditions) would lead to other strategies that accelerate contamination and facilitate foreign cation screening.

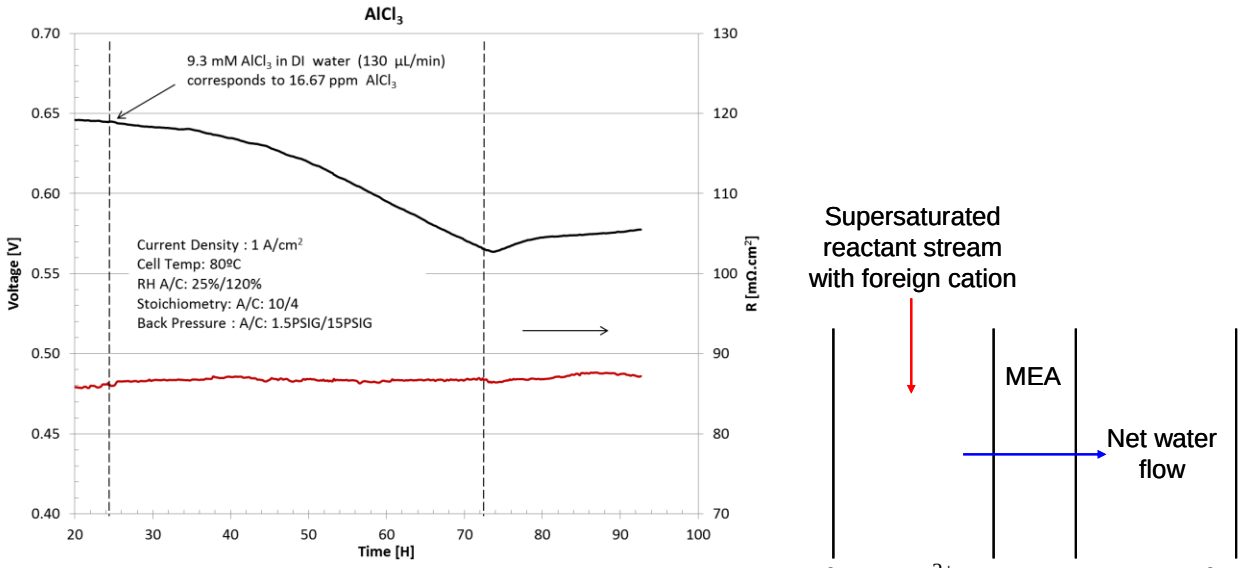

Figure 2.1.6. Cell voltage and resistance transients resulting from Al^{3+} contamination (left). Conceptual approach to favor the transport of foreign cations toward the ionomer and membrane (right). Left figure, reformatted original, *Journal of The Electrochemical Society*, **162** (4) F373-F379 (2015). © The Author(s) 2015. Published by ECS. This is an open access article distributed under the terms of the Creative Commons Attribution Non-Commercial No Derivatives 4.0 License (CC BY-NC-ND, http://creativecommons.org/licenses/by-nc-nd/4.0/), which permits non-commercial reuse, distribution, and reproduction in any medium, provided the original work is not changed in any way and is properly cited. For permission for commercial reuse, please email: oa@electrochem.org. [DOI: 10.1149/2.0291504jes]. All rights reserved.

Table 2.1.7. 2nd tier contaminants and their main sources.

Contaminant	Source
Acetonitrile (CH_3CN)	Solvent and chemical intermediate
Acetylene (C_2H_2)	Welding fuel and chemical intermediate
Bromomethane (CH_3Br)	Fumigant
Iso-propanol (C_3H_8O)	Solvent, chemical intermediate, and windshield de-icer
Methyl methacrylate ($CH_2C(CH_3)COOCH_3$)	Synthesis precursor for poly(methyl methacrylate), a shatter-resistant alternative to glass
Naphthalene ($C_{10}H_8$)	Model aromatic, chemical intermediate and fumigant
Propene (C_3H_6)	Synthesis precursor for polypropylene used for films, packaging, etc
Ca^{2+} ($Ca\text{-}Cl_2$ or $\text{-}SO_4$)	Road de-icer, desiccant, fertilizer and soil conditioner

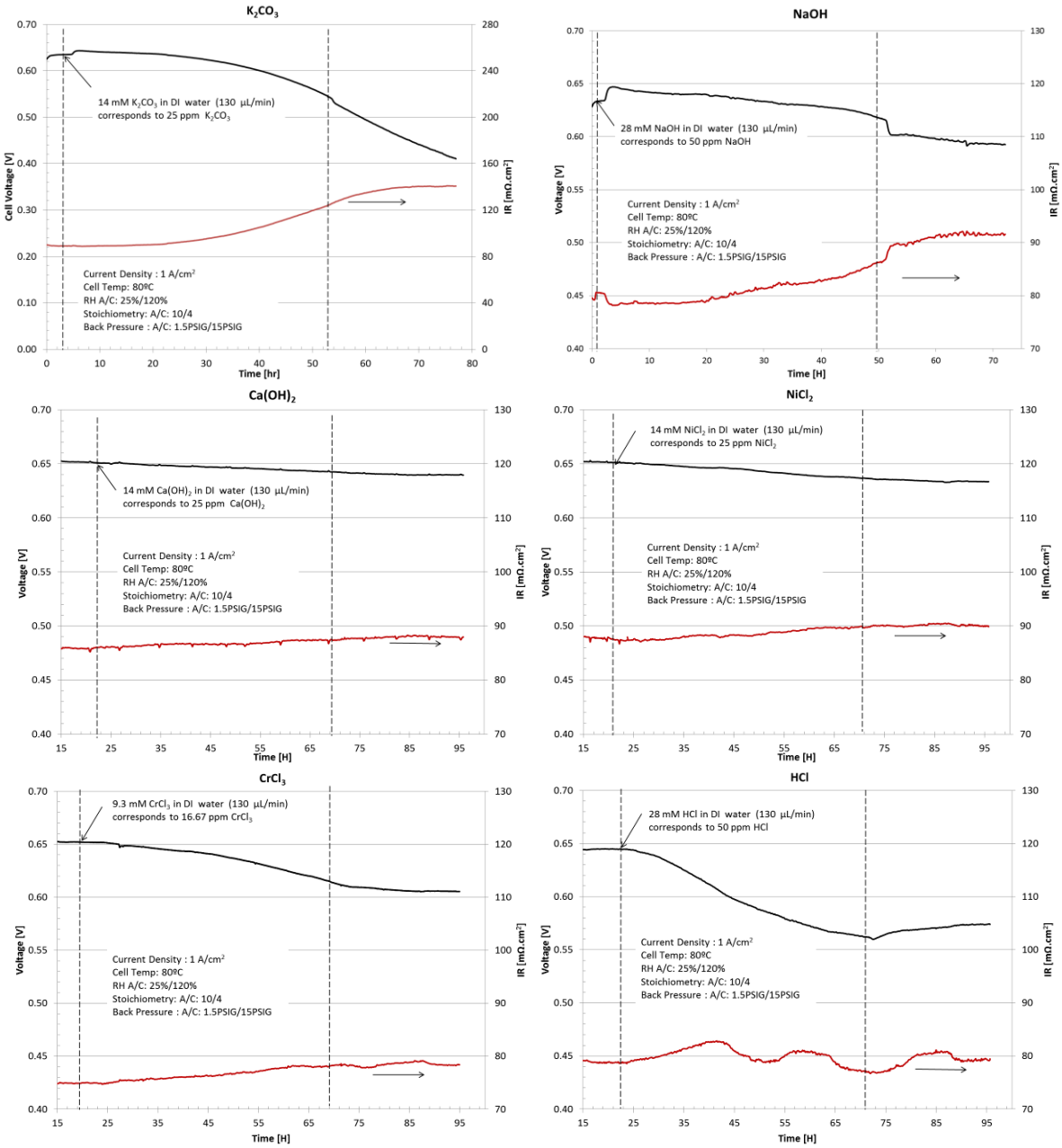

Figure 2.1.7. Cell voltage and resistance transients for a K^+ cation/CO_3^{2-} anion salt (top, left), a monovalent Na^+ cation/OH^- anion (top, right), a divalent Ca^{2+} cation/ OH^- anion (middle, left), a divalent Ni^{2+} cation/Cl^- anion (middle, right), a trivalent Cr^{3+} cation/Cl^- anion (bottom, left), a monovalent H^+ cation/Cl^- anion (bottom, right). Middle, right and bottom figures, reformatted originals, *Journal of The Electrochemical Society*, **162** (4) F373-F379 (2015).

Other results from screening tests, in addition to figure 2.1.6, left, are displayed in figure 2.1.7 (section 3.1, references J2 for SO_4^{2-}, J11 for ClO_4^- and J17 for Cl^- data with various cations).

2.2 Effects of operating conditions (milestone 2, tasks 1.2.1 and 1.3)

Fuel cells are used under a wide range of operating conditions. It is therefore important to determine the contamination effect under many operating conditions including temperature (startup and shutdown periods), current density (power demand during drive cycle), and local atmosphere composition variations. The contaminant concentration effect is particularly important because it provides guidance on contaminant threshold concentrations and invaluable information to define air filtering system tolerances (prevention). These operating conditions, temperature, current density, and contaminant concentration, lead to the largest variations in quantitative selection criteria (equations 2.1.1 and 2.1.2) for SO_2 (section 3.1, reference J1) and are the most sensitive.

A partial factorial design was used to limit the number of tests. Even with this restriction, the number of tests is equal to at least 49 for airborne contaminants alone (7 contaminants, 3 operating conditions and 3 levels with a central point, figure 2.2.1). The contaminant concentration is the first operating condition to be investigated. Subsequent tests at other current densities and temperatures are generally completed using the contaminant concentration that led to a loss in cell performance equal to or near 20 %. Levels were selected to cover a relevant and wide range in current density and temperature. Freezing temperatures were avoided considering the significant increase in test complexity. The Ca^{2+} contamination test at 10 °C was not completed due to an equipment limitation. As for the test at 45 °C, it was not completed at the same concentration as those at 80 °C because contaminant injection is tied to the cell water management (Ca^{2+} and humidification water are simultaneously provided as a solution). Therefore the 45 °C data are not directly comparable to those at 80 °C.

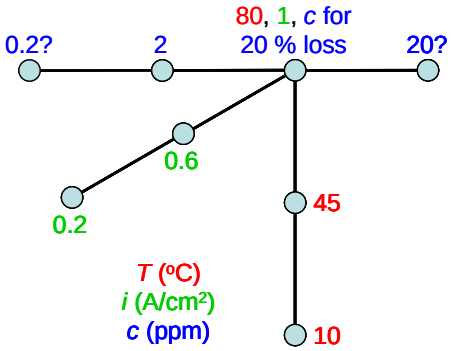

Figure 2.2.1. Partial factorial design for the determination of the operating condition sensitivity of a fuel cell to contamination (acetonitrile example).

Figures 2.2.2 to 2.2.5 summarizes data for a few airborne contaminants (acetylene, naphthalene, bromomethane). These figures confirm the strong dependency on all three operating parameters. Generally, a lower temperature leads to a larger cell voltage loss whereas larger contaminant concentrations and current densities have the same effect. These behaviors are understandable on the basis of an increase in catalyst coverage by contaminants at larger contaminant concentrations and lower temperatures, or by a more severe competition for catalyst sites

between contaminant and oxygen adsorbates at larger current densities. The performance loss was recoverable in almost all cases by changing the operating conditions to obtain a cathode potential located between 1 (open circuit voltage) and 0 V (air starvation, limiting current) versus a hydrogen reference electrode (figure 2.2.4 for naphthalene). Bromomethane, which leads to irrecoverable cell voltage losses, requires a more specific procedure (section 2.5).

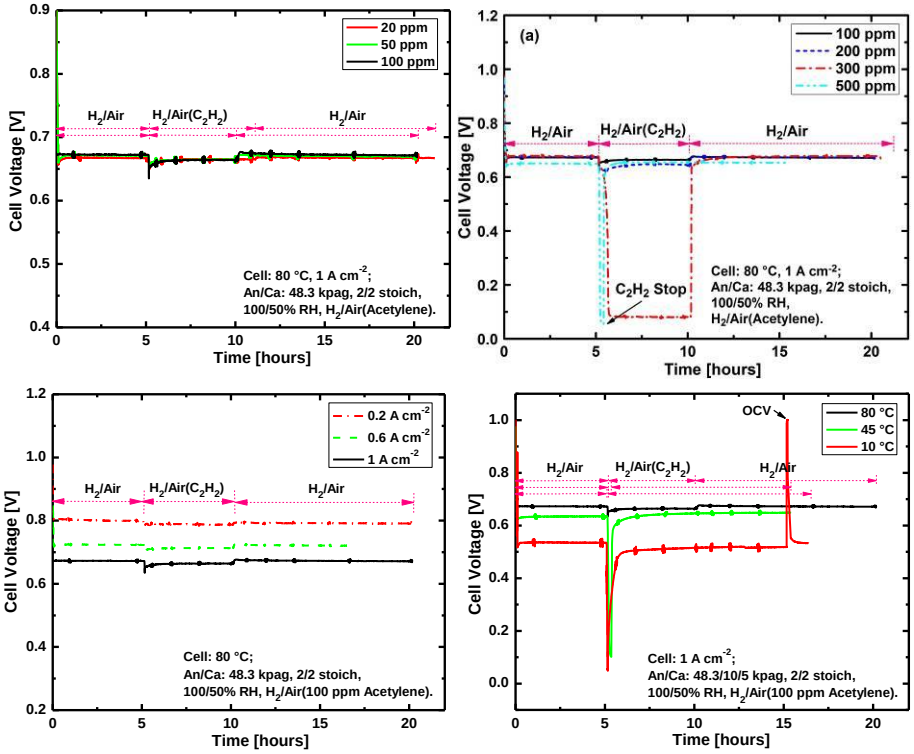

Figure 2.2.2. Effect of contaminant concentration (top), current density (bottom, left) and temperature (bottom, right) on a fuel cell temporarily contaminated with acetylene.

Figure 2.2.6 illustrates the impact of Ca^{2+} concentration and current density. A larger Ca^{2+} concentration accelerates the degradation rate (figure 2.2.6, top, left), which is consistent with an ion exchange step between the aqueous and ionomer phases and a larger decrease in membrane conductivity (figure 2.2.6, bottom, left). The ion exchange extent (ion exchange isotherm) is proportional to the ratio of the Ca^{2+} concentration to the sum of the Ca^{2+} and H^{+} concentrations. An ionomer is more conductive in a proton form because proton transport through the polymer channels benefit from the additional Grotthus mechanism. Ionomers in other forms are not as conductive. In comparison, the impact of current density is not as clear with small variations in degradation rate (figure 2.2.6, top, right). This observation is attributed to the balancing impact of several contributions such as ion exchange and water management. For instance, the larger electric field in the membrane will distort the Ca^{2+} distribution with a larger concentration at the cathode interface which decreases the ion exchange extent. More water is transferred to the anode side at low current densities with the lower impact of electroosmotic drag which favors salt precipitation as indicated by relatively sudden increases in cell resistance for 0.2 A cm^{-2} data (figure 2.2.6, bottom, right). These results imply that degradation is accelerated by larger Ca^{2+} concentrations which offer an option to obtain steady state contamination data with shorter test durations.

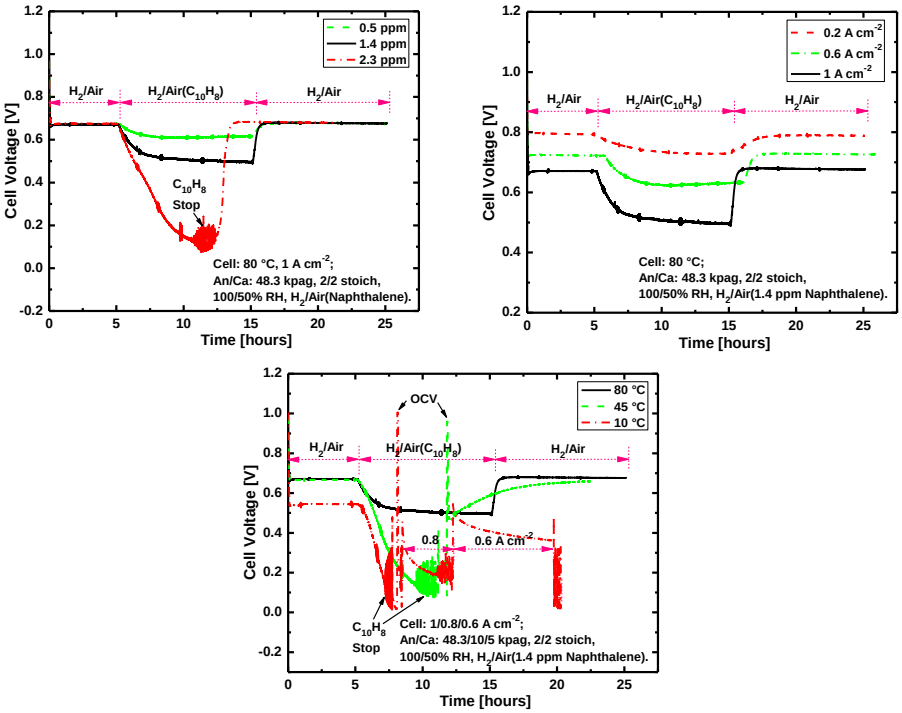

Figure 2.2.3. Effect of contaminant concentration (top, left), current density (top, right) and temperature (bottom) on a fuel cell temporarily contaminated with naphthalene. Reprinted and reformatted with permission from *ECS Trans.*, **50** (2), 635 (2012). Copyright 2012, The Electrochemical Society.

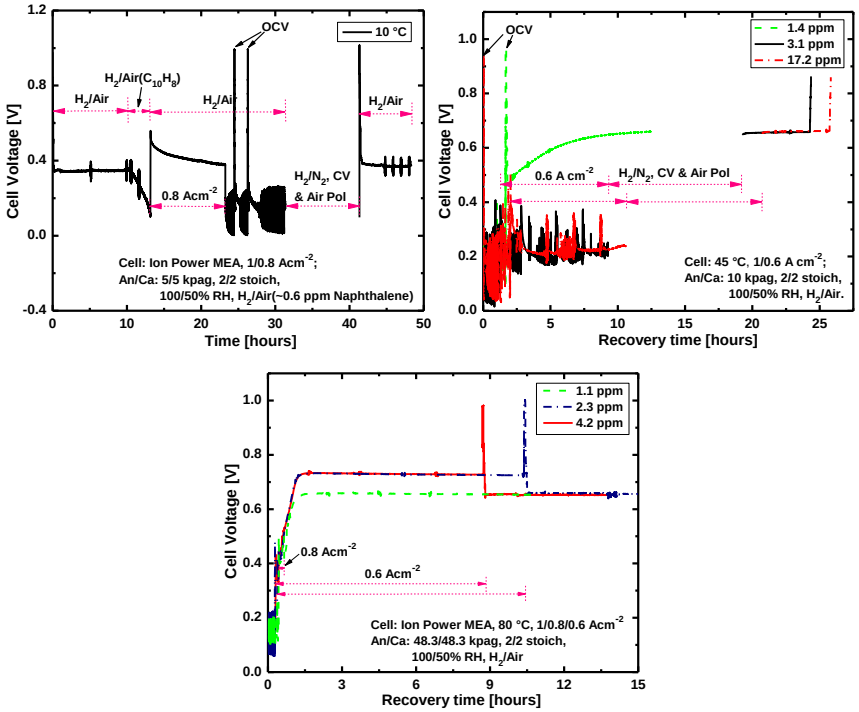

Figure 2.2.4. Effect of changes in operating conditions on performance loss recovery resulting from naphthalene contamination. 10 °C data (top, left), 45 °C (top, right), 80 °C (bottom).

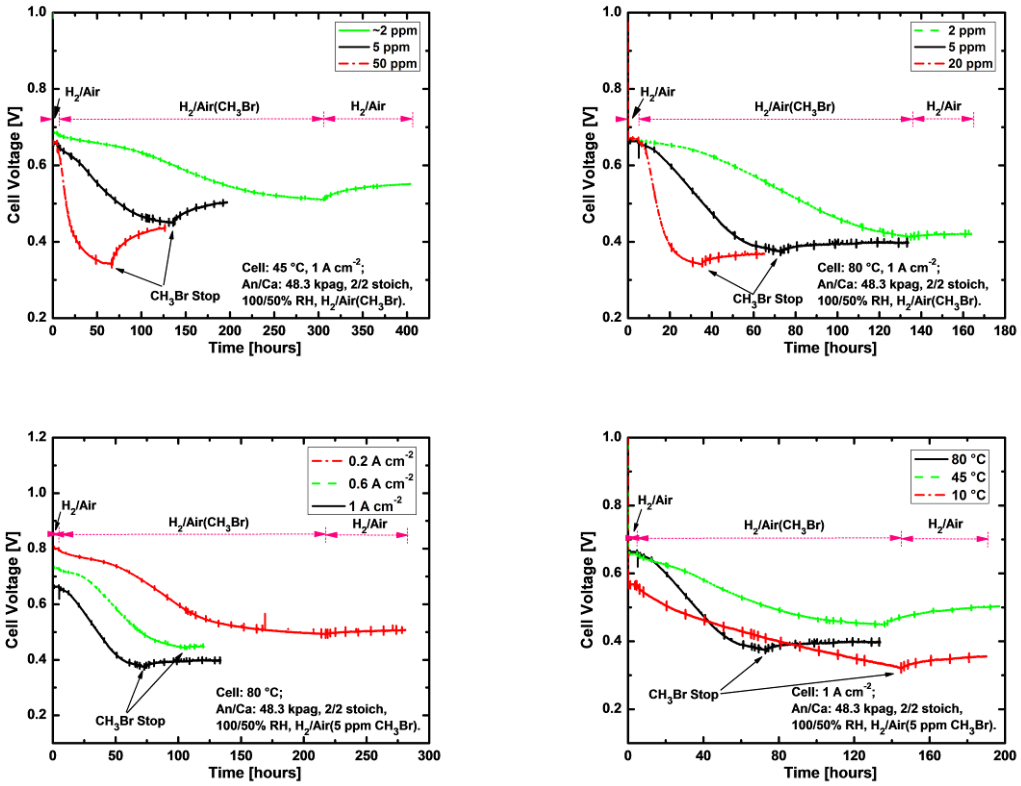

Figure 2.2.5. Effect of contaminant concentration (top), current density (bottom, left) and temperature (bottom, right) on a fuel cell temporarily contaminated with bromomethane.

Operating conditions were modified for the figure 2.2.7 additional Ca^{2+} tests to be comparable as much as possible with tests performed with organic contaminants (figures 2.2.2 to 2.2.5). This was a good opportunity to explore this comparison because Ca^{2+} concentration and temperature parameters could not be independently changed as already stated. Figure 2.2.7, left depicts the small effect of different current densities on the cell voltage degradation rate. This observation is consistent with figure 2.2.6, top, right before the onset of salt precipitation. Salt precipitation does not occur with the modified operating conditions (figure 2.2.7, left) because the modified conditions do not favor as much cation transport toward the ionomer and membrane (section 2.1). Figure 2.2.7, right shows the overall impact of a decrease in temperature from 80 to 45 °C and a decrease in effective contaminant concentration from 3.9 to 0.92 ppm Ca^{2+}. Figure 2.2.6, top, left data indicated that a decrease in Ca^{2+} concentration from 20 to 4 ppm decreased the cell voltage degradation rate. The degradation rate for the 80 °C case is negligible for a 3.9 ppm Ca^{2+} concentration (figure 2.2.7, right). The situation is expected to be unchanged at 0.92 ppm Ca^{2+} based on figure 2.2.6, right data. Therefore, it is deduced from figure 2.2.7, right that the significant decrease in cell voltage degradation rate is almost entirely attributable to the temperature decrease. However, the larger impact of Ca^{2+} contamination at a lower temperature is not as easy to ascribe to a specific mechanism because foreign cations affect thermodynamics as well as kinetic, ohmic and mass transport overpotentials [3]. Although specific adsorption of cations on the catalyst surface does not occur, an effect is still observed on the oxygen reduction reaction [4]. Also, even if the cell resistance is not affected (figure 2.2.7, right), it does not mean

that an impact is absent because measurements do not represent the actual ionomer and membrane conductivity [3]. Furthermore, the oxygen permeability through an ionomer or membrane contaminated with foreign cations is diminished [5]. This last statement is consistent with the observed temperature effect (figure 2.2.7, right) because oxygen transport in the ionomer or membrane is an activated process.

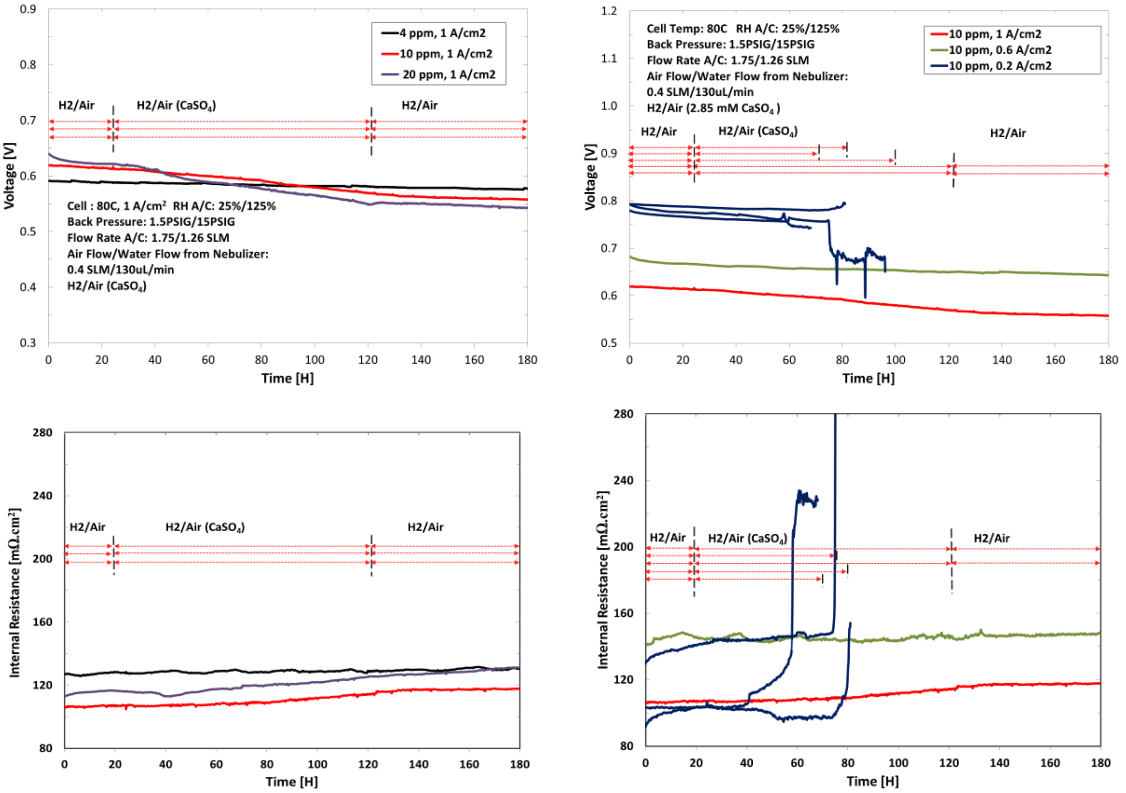

Figure 2.2.6. Effect of contaminant concentration (left) and current density (right) on cell voltage (top) and cell resistance (bottom) for a fuel cell temporarily contaminated with Ca^{2+}. Reprinted and reformatted with permission from *ECS Trans.*, **58** (1), 529 (2013). Copyright 2013, The Electrochemical Society.

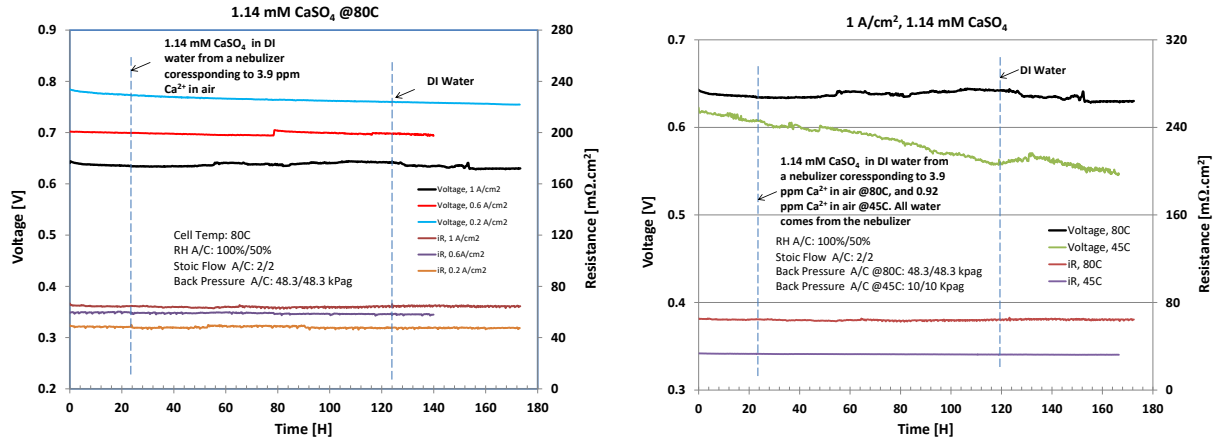

Figure 2.2.7. Effect of current density (left) and temperature (right) on cell voltage and cell resistance for a fuel cell temporarily contaminated with Ca^{2+} (1.14 mM $CaSO_4$).

Table 2.2.1 summarizes 2nd tier organic contaminant results whereas tables 2.2.2 and 2.2.3 summarize Ca^{2+} cell voltage changes after 100 h. Ca^{2+} data were treated in a different manner because steady states were not reached within reasonable durations (section 2.1). Figure 2.2.8 displays tables 2.2.1 and 2.2.2 data.

Table 2.2.1. Summary of the contaminant concentrations (in ppm) and steady state cell performance loss (in parentheses and expressed as a percentage) for the different contaminants and operating condition tests.

Contaminant	Operating conditions[a]						
	80 °C, 1 A cm^{-2}	**80 °C, 1 A cm^{-2}**	**80 °C, 1 A cm^{-2}**	**80 °C, 0.6 Acm^{-2}**	**80 °C, 0.2 Acm^{-2}**	**45 °C, 1 A cm^{-2}**	**10 °C, 1 A cm^{-2}**
Acetonitrile	100 ppm (75 %)	20 ppm (38 %)	2 ppm (9 %)	20 ppm (35 %)	20 ppm (33 %)	20 ppm (68 %)	20 ppm (78 %)
Acetylene	100/200/300 500 ppm (1/4/87/92 %)	50 ppm (1 %)	20 ppm (0 %)	100 ppm (1 %)	100 ppm (1 %)	5/20/100 ppm (1/77/85 %)	100 ppm (90 %)
Bromomethane	20 ppm (49 %)	5 ppm (43 %)	2 ppm (38 %)	5 ppm (49 %)	5 ppm (39 %)	5/20/50 ppm (32/17 after 30 h/48 %)	5 ppm (43 % after 150 h)[b]
Iso-propanol	8.6k ppm (9 %)	5.2k ppm (7 %)	250/700 ppm (2/2 %)	8.6k ppm (8 %)	8.6k ppm (6 %)	8.6k ppm (23 %)	8.6k ppm (>80 %)[c]
Methyl methacrylate	100 ppm (34 %)	20 ppm (11 %)	2 ppm (3 %)	20 ppm (8 %)	20 ppm (5 %)	20 ppm (73 %)	20 ppm (>80 %)[c]
Naphthalene	2.4 ppm (>80 %)[d]	1.4 ppm (26 %)	0.5 ppm (9 %)	1.4 ppm (14 %)	1.4 ppm (8 %)	1.4/3.1/17 ppm (>80 %)[d]	1.4 ppm (>80 %)[d]
Propene	100 ppm (18 %)	20 ppm (6 %)	2 ppm (1 %)	100 ppm (14 %)	100 ppm (8 %)	100/20 ppm (77/30 %)	100 ppm (>80 %)[c]

[a] Other operating conditions unless otherwise stated: H_2/air+contaminant, 2/2 stoichiometry, 100/50 % relative humidity, 48.3/48.3 (for 80 °C), 10/10 (for 45 °C) or 5/5 (for 10 °C) kPag.
[b] Injection stopped before the steady state was reached. The time required to reach a steady state was greater that the planned test duration.
[c] Test stopped because the cell voltage was below the 0.1 V value triggering a contaminant injection interruption. At this particular time, the cell performance was still decreasing.
[d] Cell voltage oscillations appeared before a steady state was reached. These oscillations prevent a clear identification of the steady state cell performance loss. Before these oscillations appeared, the cell performance loss was >80 %.

Table 2.2.2. Summary of the Ca^{2+} concentrations (in ppm) and cell performance loss (in parentheses and expressed as a percentage) after 100 h for the different operating condition tests that maximize transport of cations into the membrane/electrode assembly.

Contaminant	Operating conditions[a]						
	80 °C, 1 A cm^{-2}	**80 °C, 1 A cm^{-2}**	**80 °C, 1 A cm^{-2}**	**80 °C, 0.6 Acm^{-2}**	**80 °C, 0.2 Acm^{-2}**	**45 °C, 1 A cm^{-2}**	**10 °C, 1 A cm^{-2}**
Calcium sulfate	20 ppm (12 %)	10 ppm (8 %)	4 ppm (1 %)	10 ppm (3 %)	10 ppm (16-90 %)[b]	-	-

[a] Other operating conditions unless otherwise stated: H_2/air+contaminant, 1.75/1.66 L min^{-1}, 25/125 % relative humidity, 10.3/103 kPag.
[b] Results from multiple repetitions. Severe flow field plugging was observed, causing significant variations.

Table 2.2.3. Summary of the Ca^{2+} concentrations (in ppm) and cell performance loss (in parentheses and expressed as a percentage) after 100 h for the different operating condition tests.

Contaminant	Operating conditions[a]						
	80 °C, 1 A cm^{-2}	80 °C, 1 A cm^{-2}	80 °C, 1 A cm^{-2}	80 °C, 0.6 Acm^{-2}	80 °C, 0.2 Acm^{-2}	45 °C, 1 A cm^{-2}	10 °C, 1 A cm^{-2}
Calcium sulfate	-	-	3.9 ppm (1 %)	3.9 ppm (0.1 %)	3.9 ppm (1.7 %)	0.92 ppm (8%)	-

[a] Other operating conditions unless otherwise stated: H_2/air+contaminant, 2/2 stoichiometry, 100/50 % relative humidity, 48.3/48.3 (for 80 °C) or 10/10 (for 45 °C) kPag.

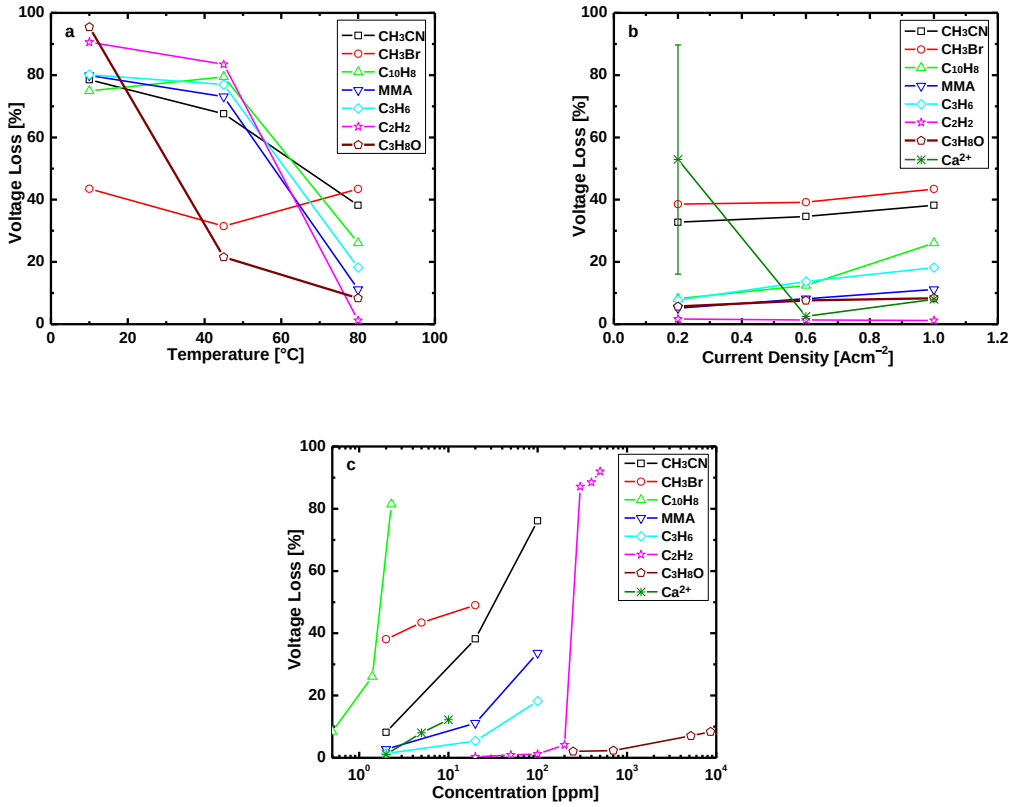

Figure 2.2.8. Effect of temperature (top, left), current density (top, right) and contaminant concentration (bottom) on fuel cell performance losses for 7 airborne contaminants and a foreign cation. CH_3CN: acetonitrile, CH_3Br: bromomethane, $C_{10}H_8$: naphthalene, MMA: methyl methacrylate, C_3H_6: propylene, C_2H_2: acetylene, C_3H_8O: iso-propanol, Ca^{2+}: calcium.

The effect of temperature is generally large (figure 2.2.8, top, left) which implies that for freezing temperatures, likely encountered during startup events in cold climates, even greater cell voltage losses are expected (>80 %). Such operating conditions were avoided here to limit test complexity. It is recommended that for future studies, a model contaminant be selected to conduct tests with concentration closer to atmospheric values and commercially relevant membrane/electrode assemblies to assess failure risks. Concurrent tests with an air filter should also be considered to evaluate its mitigating effect. The lower temperature favors contaminant adsorption on both catalyst and filter adsorbent surfaces.

In contrast, the current density effect is relatively much smaller than the temperature effect, especially for organic contaminants with cell voltage loss changes <10 % between 0.2 and 1 A cm^{-2} (figure 2.2.8, top, right). Also, cell voltage control (section 2.3) leads to larger variations in current density loss (more than 50 %) than the current density as observed for acetylene and acetonitrile contamination (section 3.1, references C5 and C15). Contaminant concentration is as impactful as temperature (figure 2.2.8, bottom) with cell voltage loss variations that exceed 90 %. Contaminant concentration data were analyzed in more detail in section 1.2 to derive tolerance limits (table 1.2.1).

2.3 Contamination mechanisms (milestone 3, tasks 1.2.2, 1.2.3 and 1.4)

The milestone 2 data (effects of operating conditions, section 2.2) includes impedance spectra obtained for the 7 organic 2nd tier airborne contaminants, the 7 operating condition cases and varying times (>490 impedance spectra). Data were fitted to a common equivalent circuit (figure 2.3.1) to extract kinetic, ohmic and mass transfer resistances and obtain an initial evaluation of contamination mechanisms. The circuit contains 2 main loops: an oxygen reduction loop (~10 Hz to ~1 kHz) and an oxygen/liquid water mass transfer loop (<10 Hz). The remainder of the circuit is ascribed to the barely perceptible hydrogen oxidation loop (>1 kHz), which has also been attributed to other phenomena. This high frequency loop will not be further discussed in part because it is not related to the main focus of this project. The figure 2.3.1 acetonitrile example shows kinetic, ohmic, and mass transfer losses with a diameter increase for both of the main loops and a translation of the entire spectra to larger real impedance values. Dimensionless ratios were calculated by dividing kinetic (oxygen reduction), ohmic and mass transfer resistances at 80 °C and 1 A cm^{-2} with pre-contamination baseline values (figure 2.3.2). Only iso-propanol led to a larger kinetic resistance (figure 2.3.2, top, left). All other organic contaminants led to larger kinetic and mass transfer resistances (acetonitrile, acetylene, bromomethane, methyl methacrylate, naphthalene, propene, figure 2.3.2, top, left and bottom). Among the 2nd tier organic contaminants, only acetonitrile led to a larger ohmic resistance (figure 2.3.2, top, right). These results already suggest that multi-step recovery procedures may be needed for bromomethane, the only contaminant that led to irrecoverable losses. Subsequent activities were targeted at understanding in more detail the origin of these different losses (2nd iteration) using a combination of *in situ* and *ex situ* tests.

Figure 2.3.2 top, left and bottom are similar which suggests a link between changes in kinetic and mass transfer resistances. A lower Pt catalyst loading leads to a smaller active area and higher mass transfer losses [6-10]. In the present contamination case, the decrease in catalyst area originates from species adsorption on the catalyst rather than a Pt loading decrease. A correlation was explored with figure 2.3.2 data by plotting the dimensionless mass transfer resistances as a function of the dimensionless kinetic resistances. Figure 2.3.3, left indicates that a significant correlation exists supporting an increase in mass transfer loss with contaminant adsorption on the catalyst. The consistency of figure 2.3.3, left data was verified by calculating the sum of the kinetic, ohmic and mass transfer resistances and corresponding ohmic losses by multiplication with current densities, and plotting these values as a function of the measured voltage losses resulting from contamination at steady state (figure 2.3.3, right).

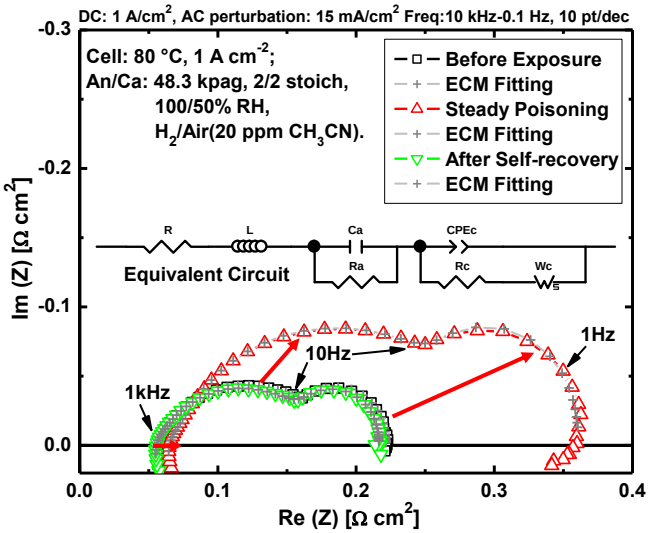

Figure 2.3.1. Impedance spectra for acetonitrile before, during and after contamination and fuel cell equivalent circuit. Reprinted with permission from *ECS Trans.*, **58** (1), 519 (2013). Copyright 2013, The Electrochemical Society.

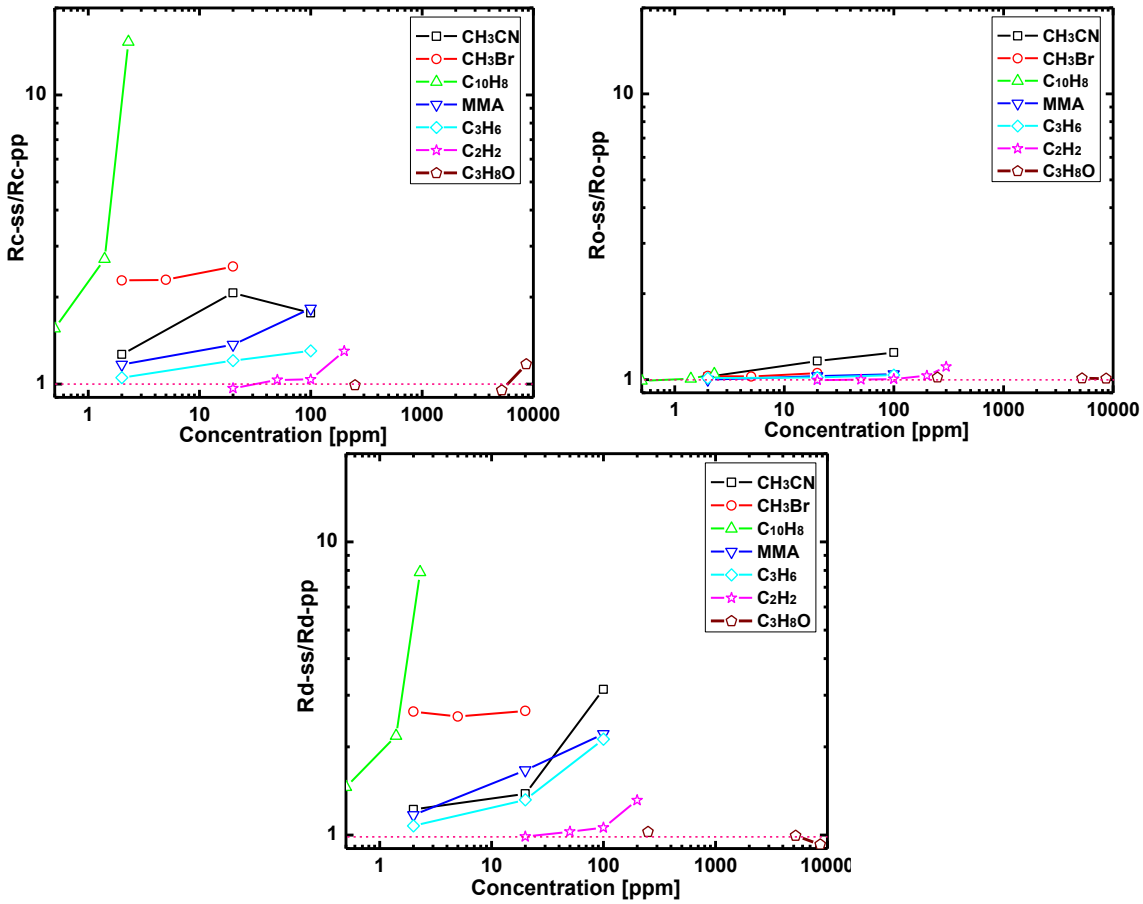

Figure 2.3.2. Dimensionless kinetic (top, left), ohmic (top, right) and mass transfer (bottom) resistances for all seven 2nd tier organic airborne contaminants. Reprinted and reformatted with permission from *ECS Trans.*, **58** (1), 519 (2013). Copyright 2013, The Electrochemical Society.

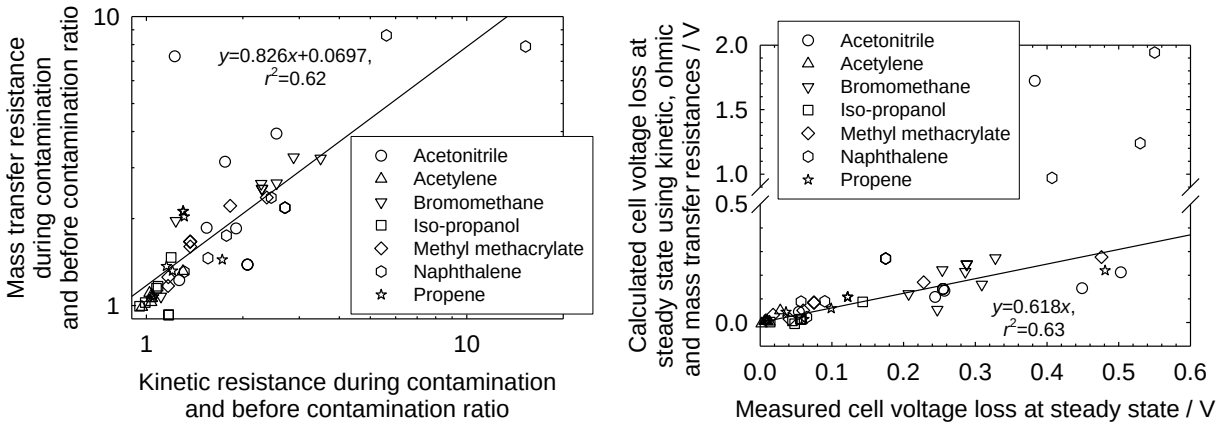

Figure 2.3.3. Dimensionless mass transfer resistances as a function of dimensionless kinetic resistances during contamination (left). Calculated cell voltage losses using kinetic, ohmic and mass transfer resistances as a function of measured cell voltage losses (right). The left figure is reprinted and reformatted with permission from *ECS Trans.*, **58** (1), 519 (2013). Copyright 2013, The Electrochemical Society.

Figure 2.3.3, right shows a strong correlation which supports the relationship observed in figure 2.3.3, left. It is noted that the slope of the correlation in figure 2.3.3, right is not equal to 1 as expected. This situation is largely due to the use of an ohmic model to correlate resistances to a cell voltage loss. This model is inappropriate for kinetic and mass transfer resistances that are current density dependent. However, insufficient data were available to use other models.

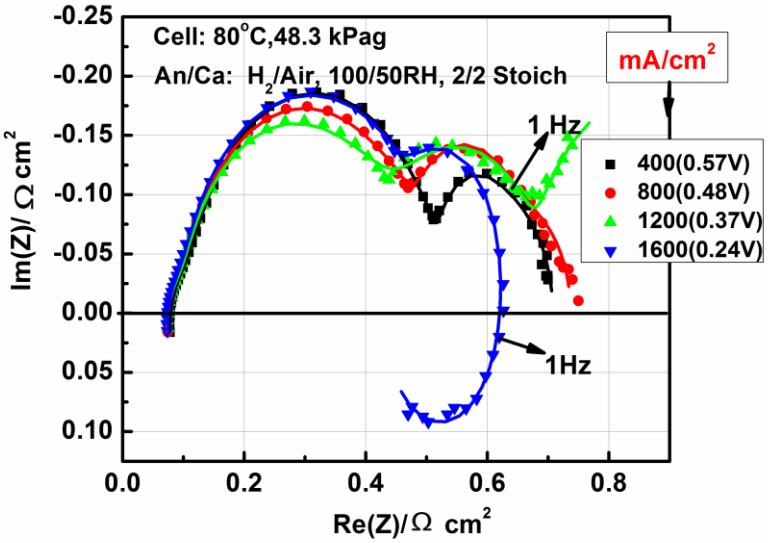

Figure 2.3.4. Impedance spectra at different current densities during propene contamination.

Additional work would be beneficial to more directly confirm and clarify the correlation existing between kinetic and mass transfer resistances during contamination (figure 2.3.3, left) by employing polarization curves up to the limiting current to relate kinetic and mass transfer

contributions. This suggestion is reinforced by the observation that the equivalent circuit generally used to evaluate resistances (figure 2.3.1) may not always be appropriate. Additional data obtained during propene contamination suggests that the low frequency loop initially ascribed to mass transfer may include contributions associated with contaminant oxidation or reduction, which manifested themselves as an additional loop at low cell voltages (figure 2.3.4). At the lowest cell voltage of 0.24 V, an inductive loop is present whereas at 0.37 V, a third capacitive loop has appeared (figure 2.3.4). For higher cell voltages, the propene reaction contribution is either masked or disappeared. Figure 2.3.4 data were fitted to an equivalent circuit that takes into account the presence of 2 reactions at the cathode (oxygen reduction, propene reduction or oxidation) [11-12]. The modified equivalent circuit is illustrated in figure 2.3.5, bottom and compared to the equivalent circuit generally used to analyze contamination data (figure 2.3.5, top). Propene data analysis is still ongoing (section 3.1, reference J39).

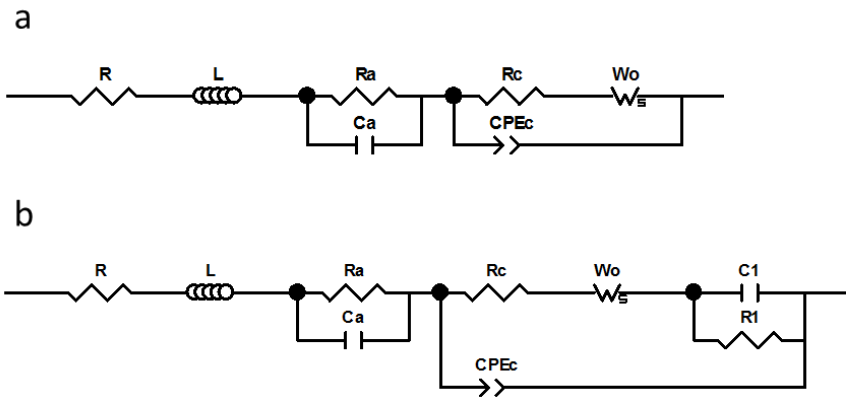

Figure 2.3.5. Equivalent circuit generally used to analyze contamination data as described in figure 2.3.1 (top). Modified equivalent circuit employed to evaluate propene contamination data obtained under a wide range of operating conditions as depicted in figure 2.3.4 (bottom).

Impedance data revealed that contamination affected all overpotential types observed in absence of contamination (kinetic, ohmic, mass transfer). Additional insight into contamination mechanisms was therefore obtained with the use of measurement methods able to probe each of the identified overpotential types (figure 2.3.6): rotating ring/disc electrode or RRDE (kinetic overpotential), membrane conductivity cell (ohmic overpotential), segmented fuel cell and single fuel cell combined with gas chromatography/mass spectrometry and impedance spectroscopy (all overpotential types). These methods were consistently applied to all 2nd tier organic contaminants. For Ca^{2+}, similar or equivalent methods were used but were supplemented to take account of the specific features of that contaminant class. Gas chromatography and mass spectroscopy were not used because Ca^{2+} was not expected to undergo reactions at the fuel cell cathode potentials. In contrast, photography (figure 1.3.1), scanning electron microscopy, and energy dispersive X-ray spectroscopy microscopy (figure 1.3.2) were employed to examine salt precipitation and a through-plane segmented membrane/electrode assembly was utilized in addition to an in-plane segmented cell to probe *in situ* the Ca^{2+} concentration gradient created by the presence of the potential gradient within the membrane (figure 2.3.7). Other complementary characterization methods were also used such as polarization curves, cyclic voltammetry, titration (membrane/electrode assembly ion exchange capacity), inductively coupled plasma mass spectroscopy, and ion chromatography (fuel cell outlet water composition), etc.

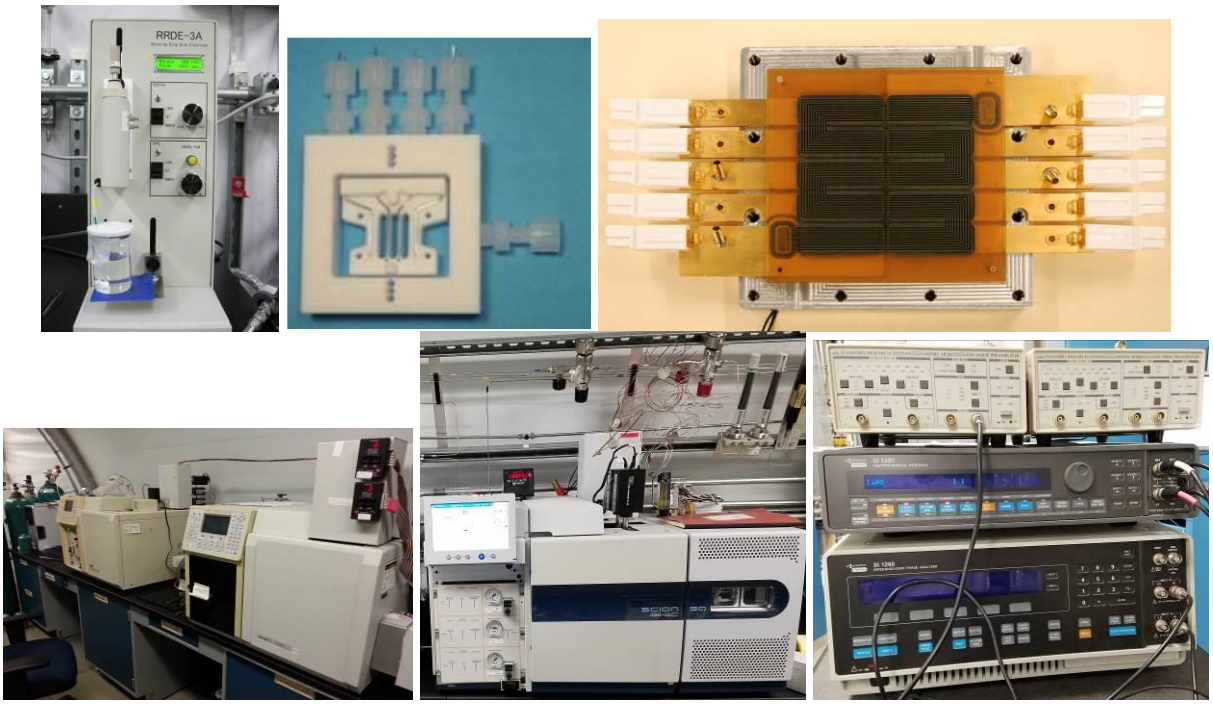

Figure 2.3.6. Equipment used to investigate contaminant mechanisms by organic species. Rotating ring/disc electrode (top left), BekkTech membrane conductivity cell (top, center), segmented cell (top, right), gas chromatographs (bottom, left), gas chromatograph/mass spectrograph (bottom, center), impedance analyzer, electrochemical interface, and low-noise pre-amplifiers (bottom, right). Top, right figure is a reformatted original, *Journal of The Electrochemical Society*, **163** (9) F1100-F1106 (2016).

In the remainder of this section, focus is given to acetylene, acetonitrile and Ca^{2+} contaminant mechanisms to illustrate the use of each technique (figures 2.3.6 and 2.3.7). These contaminants include a species from each class as well as acetonitrile, the only organic species that led to an ohmic loss (figures 2.3.1 and 2.3.2, top, right). This section will end with summaries of key parameters and contamination mechanisms for all species.

2.3.1 *Acetylene (section 3.1, references J8, J13, J14, J25)*

Rotating ring/disc electrode cyclic voltammetry data indicate that acetylene oxidizes above 0.4 V vs RHE (peak at 1.18 V vs the reversible hydrogen electrode or RHE in figure 2.3.8). In addition, acetylene reduces below 0.25 V vs RHE (larger negative currents in the hydrogen adsorption region between ~0-0.2 V vs RHE in comparison to the uncontaminated Pt surface). Concomitantly, the Pt active surface is smaller in the hydrogen oxidation region (smaller positive currents in the 0 to 0.3 V vs RHE region) due to acetylene adsorption on the catalyst surface.

Furthermore, Pt oxidation has decreased (smaller area under the Pt reduction peak at 0.7 V vs RHE) and is also due to acetylene adsorption.

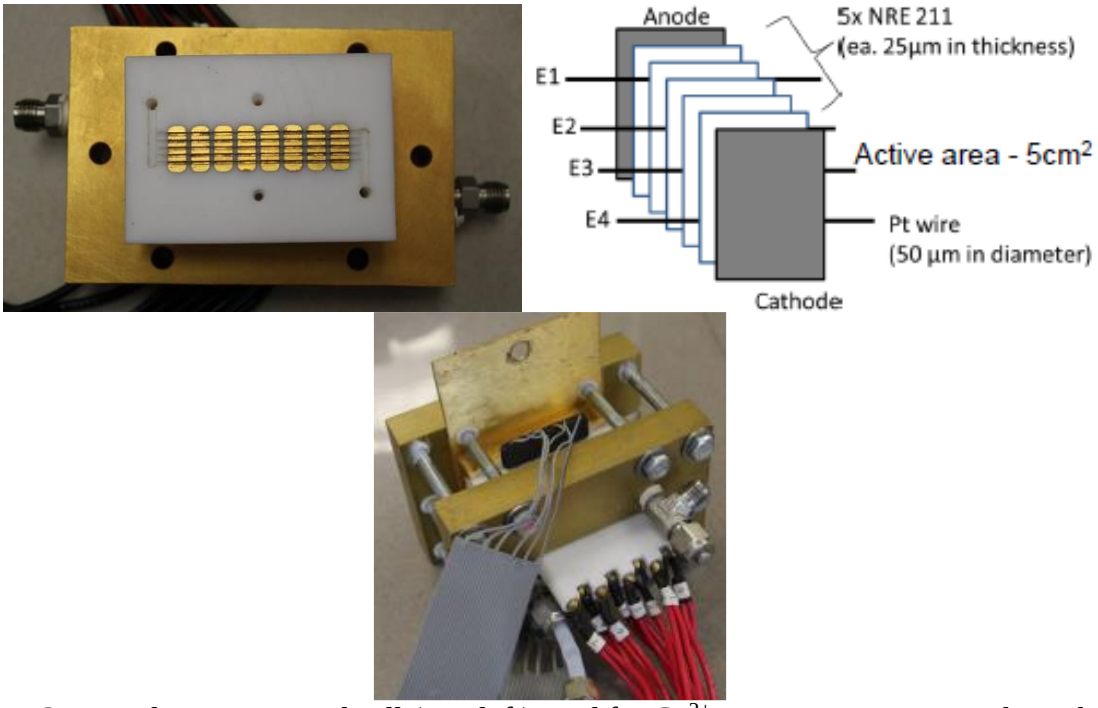

Figure 2.3.7. In-plane segmented cell (top, left) used for Ca^{2+} contamination tests. Through-plane segmented membrane/electrode assembly concept (top, right) and the segmented membrane/electrode assembly installed within the in-plane segmented cell (bottom). The top, right figure is reprinted and reformatted with permission from *ECS Trans.*, **61** (12), 37 (2014). Copyright 2014, The Electrochemical Society.

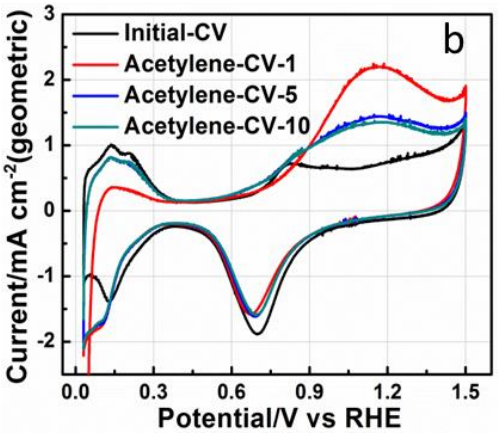

Figure 2.3.8. Cyclic voltammograms of a Pt/C film on a glassy carbon rotating disc electrode in the absence and the presence of 4000 ppm C_2H_2. Reprinted from Electrochimica Acta, Volume 133, Junjie Ge, Jean St-Pierre, Yunfeng Zhai, PEMFC Cathode Catalyst Contamination Evaluation with a RRDE - Acetylene, Pages 65-72, Copyright (2014), with permission from Elsevier (http://www.sciencedirect.com/science/journal/00134686?sdc=1).

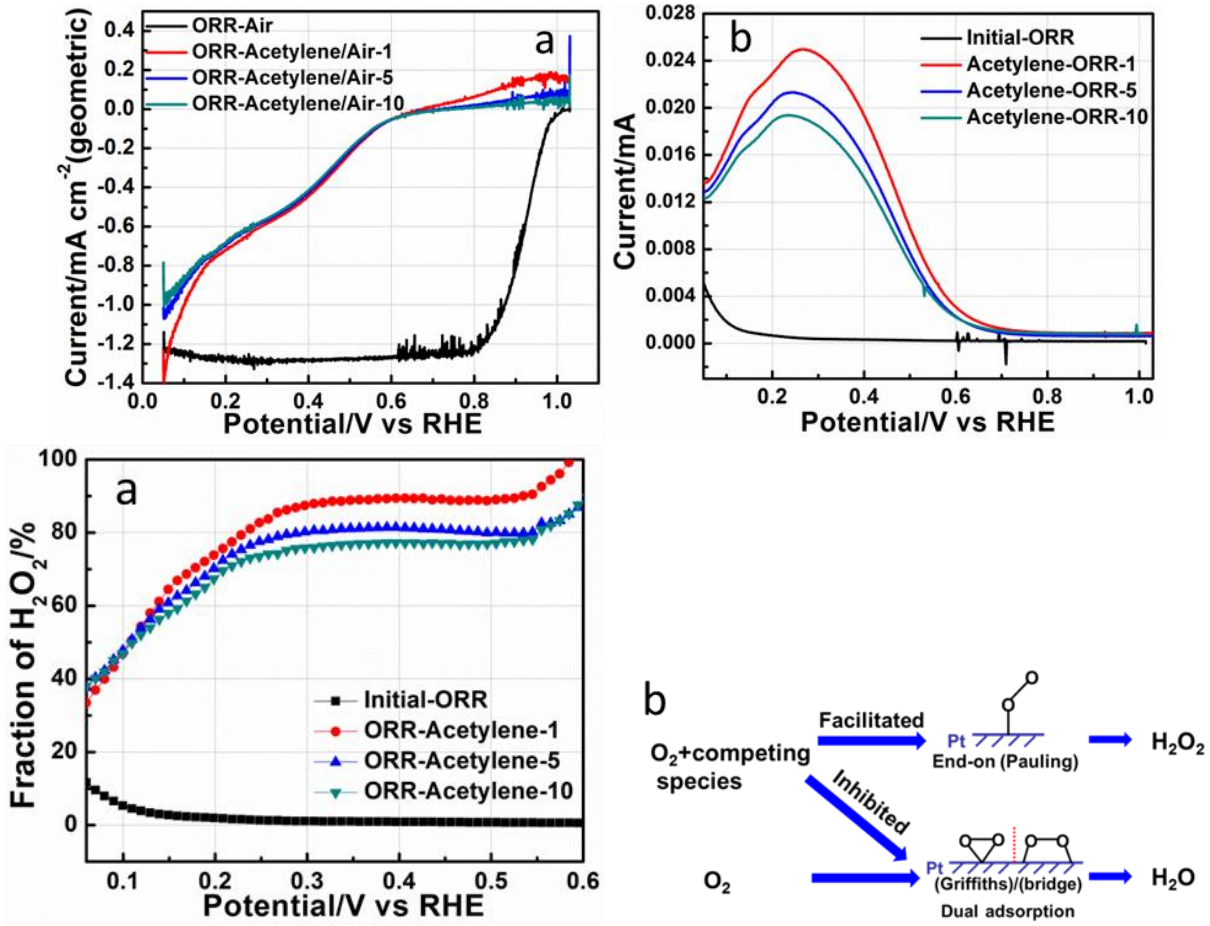

Figure 2.3.9. Linear scan voltammograms of a Pt/C film on rotating glassy carbon disc (top, left) and Pt ring (top, right) electrodes exposed to O_2 in the absence and the presence of 4000 ppm C_2H_2. Corrected ring currents (bottom, left). The main oxygen reduction product (H_2O) results from O_2 adsorption on 2 contiguous Pt catalyst sites (bottom, right) whereas the side reaction product (H_2O_2) is formed by O_2 adsorption on a single Pt catalyst site. The top, left figure is reprinted from Electrochimica Acta, Volume 133, Junjie Ge, Jean St-Pierre, Yunfeng Zhai, PEMFC Cathode Catalyst Contamination Evaluation with a RRDE - Acetylene, Pages 65-72, Copyright (2014), with permission from Elsevier (http://www.sciencedirect.com/science/journal/00134686?sdc=1).

Linear scan voltammograms obtained in the presence of oxygen revealed a largely impeded oxygen reduction reaction (figure 2.3.9, top, left) and a significantly increased ring current attributed to hydrogen peroxide oxidation (figure 2.3.9, top, right). This observation suggests that membrane and ionomer degradation in a fuel cell is likely enhanced in the presence of contaminants. A similar increase in hydrogen peroxide production was also observed for all other 2^{nd} tier contaminants (table 2.3.2 and 2.3.3) and justified long term contamination tests with acetonitrile and Ca^{2+} (section 2.4.1). The ring current is corrected using the following expression [13]:

$$\text{Fraction of } H_2O_2 = \frac{2\frac{I_R}{N}}{I_D + \frac{I_R}{N}} \quad (2.3.1)$$

where I_R represents the ring current (A), N the ring collection efficiency and I_D the disc current (A). Figure 2.3.9, bottom, left shows that the fraction of peroxide produced raises from less than ~1-2 % to ~80 % between 0.3-0.5 V vs RHE in the presence of acetylene. The large increase is ascribed to a decrease in available Pt catalyst sites. Two contiguous Pt sites are needed to form water (figure 2.3.9, bottom, right). However, in the presence of acetylene, competitive adsorption takes place forcing O_2 adsorption in an end-on configuration which leads to hydrogen peroxide. Below 0.25 V vs RHE, acetylene is reduced which decreases its influence leading to a decrease in hydrogen peroxide production (figure 2.3.9, bottom, left).

Polarization curves (figure 2.3.9, top, left and, figure 2.3.10, top, left and right) were replotted using the Koutecky-Levich relationship (figure 2.3.10, bottom, left) to extract kinetic current values (mass transfer correction) and average number of electrons exchanged:

$$\frac{1}{i} = \frac{1}{i_k} + \frac{1}{i_l} = \frac{1}{i_k} + \frac{1}{0.62nFD^{2/3}\omega^{1/2}\nu^{-1/6}c} \quad (2.3.2)$$

where i is the overall current density (A cm^{-2}), i_k the kinetic current density (A cm^{-2}), i_l the limiting current density (A cm^{-2}), n the average number of electrons exchanged, F the Faraday constant (96,500 C mol^{-1}), D the oxygen diffusion coefficient (cm^2 s^{-1}), ω the electrode rotation speed (rad s^{-1}), ν the electrolyte kinematic viscosity (cm^2 s^{-1}), and c the oxygen concentration (mol cm^{-3}). The slopes of Koutecky-Levich plots leads to average charge transfer numbers (F, D, ν and c are known) that are consistent with those derived from hydrogen peroxide (figure 2.3.9, top, right) and total current (figure 2.3.9, top, left) densities (figure 2.3.10, bottom, right):

$$n = \frac{4I_D}{I_D + \frac{I_R}{N}} \quad (2.3.3)$$

where n is the average number of electrons exchanged, I_D the disc current (A), I_R the ring current (A) and N the ring collection efficiency. In the absence of a side reaction (H_2O is the product), n=4 whereas for a H_2O_2 product, n=2. In the presence of acetylene, n is very close to 2 (figure 2.3.10, bottom, right) because a large amount of hydrogen peroxide is formed in the 0.3-0.5 V vs RHE range (figure 2.3.9, bottom, left).

The kinetic currents calculated using disc and limiting currents (figure 2.3.9, top, left) using equation 2.3.2 are reproduced in figure 2.3.11. Acetylene modifies the oxygen reduction rate determining step because the Tafel slope increases from the expected 61 to 179 at current densities below ~0.8 mA cm^{-2} and 274 mV decade^{-1} at current densities above ~0.8 mA cm^{-2}. It

is assumed that the acetylene adsorbates on the Pt catalyst surface detected by cyclic voltammetry (figure 2.3.8) interact with O_2 adsorbates:

$$O_2 + Pt \rightarrow Pt(O_2)_{ads} \quad (2.3.4)$$

$$Pt(O_2)_{ads} + e^- \rightarrow Pt(O_2^-)_{ads} \quad \text{(rate determining step)} \quad (2.3.5)$$

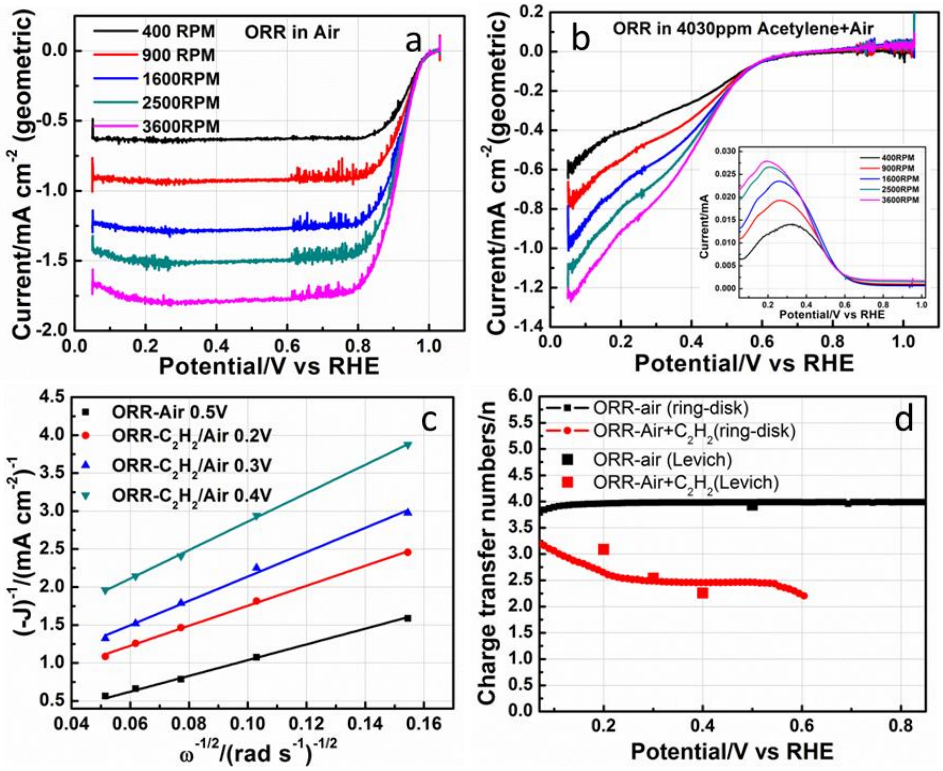

Figure 2.3.10. Linear scan voltammograms of a Pt/C film on a rotating glassy carbon disc electrode exposed to O_2 in the absence (top, left) and the presence (top, right) of 4000 ppm C_2H_2 for different electrode rotation speeds. Corresponding Koutecky-Levich plots (bottom, left) and charge transfer numbers (bottom, right). Top and bottom, left figures are reprinted from Electrochimica Acta, Volume 133, Junjie Ge, Jean St-Pierre, Yunfeng Zhai, PEMFC Cathode Catalyst Contamination Evaluation with a RRDE - Acetylene, Pages 65-72, Copyright (2014), with permission from Elsevier (http://www.sciencedirect.com/science/journal/00134686?sdc=1).

A linear sweep voltammogram and cyclic voltammograms completed after the electrode was removed from the cell, rinsed with water and immersed in a second cell with an uncontaminated electrolyte demonstrated that this simple procedure was sufficient to restore performance. Figure 2.3.12, top, left shows that the oxygen polarization curve has almost returned to its original state with the exception of a slightly smaller limiting current. In comparison, the ring currents are equal before contamination and after recovery (figure 2.3.12, top, right). Cyclic voltammograms were subsequently completed with increasingly higher values for the maximum cathode potential to increase the extent of leftover acetylene adsorbates' oxidation. For the first series, the maximum cathode potential of 1 V vs RHE led to a recovery level of 92 % based on the Pt catalyst active area (Figure 2.3.12, top, left, inset). In the hydrogen oxidation region (0-0.3 V vs

RHE), the current after recovery is slightly lower than before contamination. The recovery level increases to 97 % after voltammograms are completed with a maximum cathode potential of 1.2 V vs RHE (figure 2.3.12, bottom, left). A further increase to a maximum cathode potential of 1.5 V vs RHE does not alter the recovery level (figure 2.3.12, bottom, right). Cathode potentials higher than 1 V vs RHE may lead to degradation (catalyst carbon support corrosion) and are problematic to implement with a fuel cell stack or system.

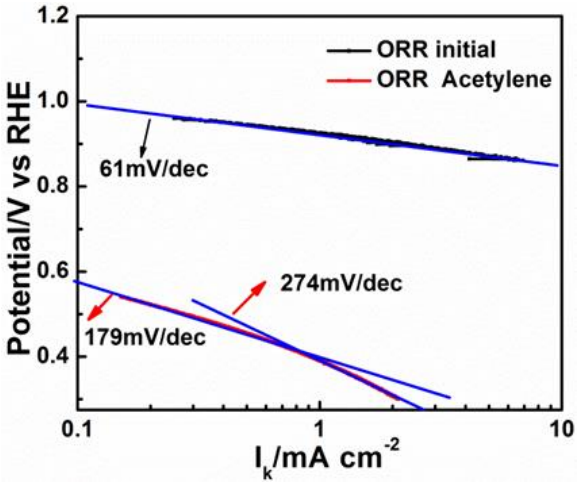

Figure 2.3.11. Oxygen reduction Tafel plots in the absence and in the presence of 4000 ppm C_2H_2. Reprinted from Electrochimica Acta, Volume 133, Junjie Ge, Jean St-Pierre, Yunfeng Zhai, PEMFC Cathode Catalyst Contamination Evaluation with a RRDE - Acetylene, Pages 65-72, Copyright (2014), with permission from Elsevier (http://www.sciencedirect.com/science/journal/00134686?sdc=1).

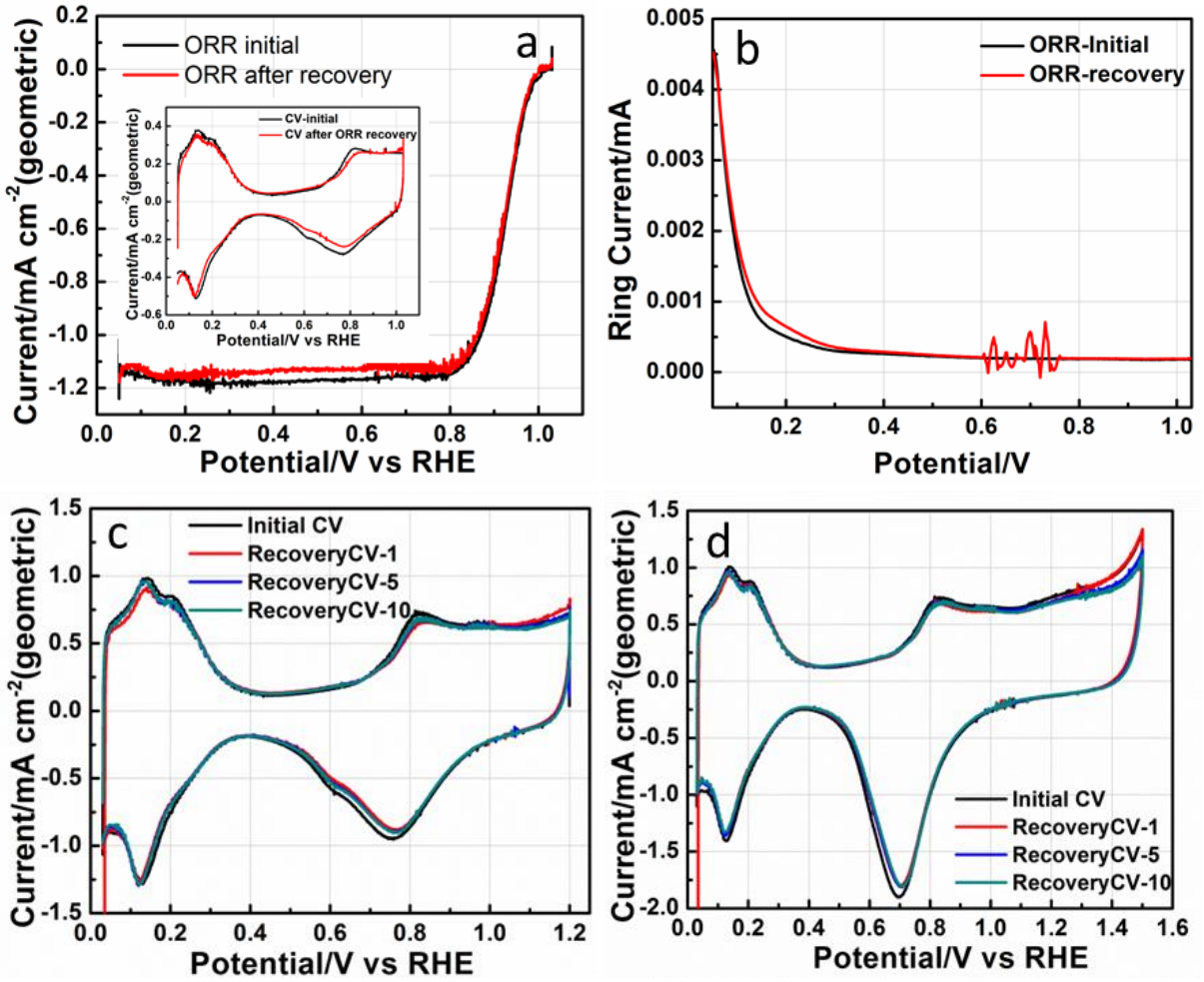

Figure 2.3.12. Linear scan voltammograms of a Pt/C film on rotating glassy carbon disc (top, left) and Pt ring (top, right) electrodes exposed to O_2 before and after exposure to 4000 ppm C_2H_2. Subsequent cyclic voltammograms were successively obtained by increasing the maximum cathode potential from 1 (top, left, inset) to 1.2 (bottom, left) and 1.5 (bottom, right) V vs RHE. Reprinted from Electrochimica Acta, Volume 133, Junjie Ge, Jean St-Pierre, Yunfeng Zhai, PEMFC Cathode Catalyst Contamination Evaluation with a RRDE - Acetylene, Pages 65-72, Copyright (2014), with permission from Elsevier (http://www.sciencedirect.com/science/journal/00134686?sdc=1).

A 27.5 μm thick Nafion XL membrane sample loaded in a BekkTech membrane conductivity cell (figure 2.3.6, top, center) was exposed to a H_2/N_2 stream containing either 0 or 500 ppm C_2H_2. It was assumed that this ionomer is similar to the Gore catalyst coated membrane ionomer used for *in situ* fuel cell tests (uncatalyzed Gore membranes were not available). Chronopotentiometry (the potential divided by the imposed current gives the resistance), cyclic voltammetry (the slope of the curves is equal to the resistance), and impedance spectroscopy (high frequency intercepts with the real impedance axis of ~8,850 ohms are similar) measurements were completed (figure 2.3.13), and they consistently revealed the absence of an acetylene effect (the conductivity change was ~1-2 %). The *ex situ* results correlate well with normalized high frequency resistance fuel cell data (figure 2.3.2, top, right).

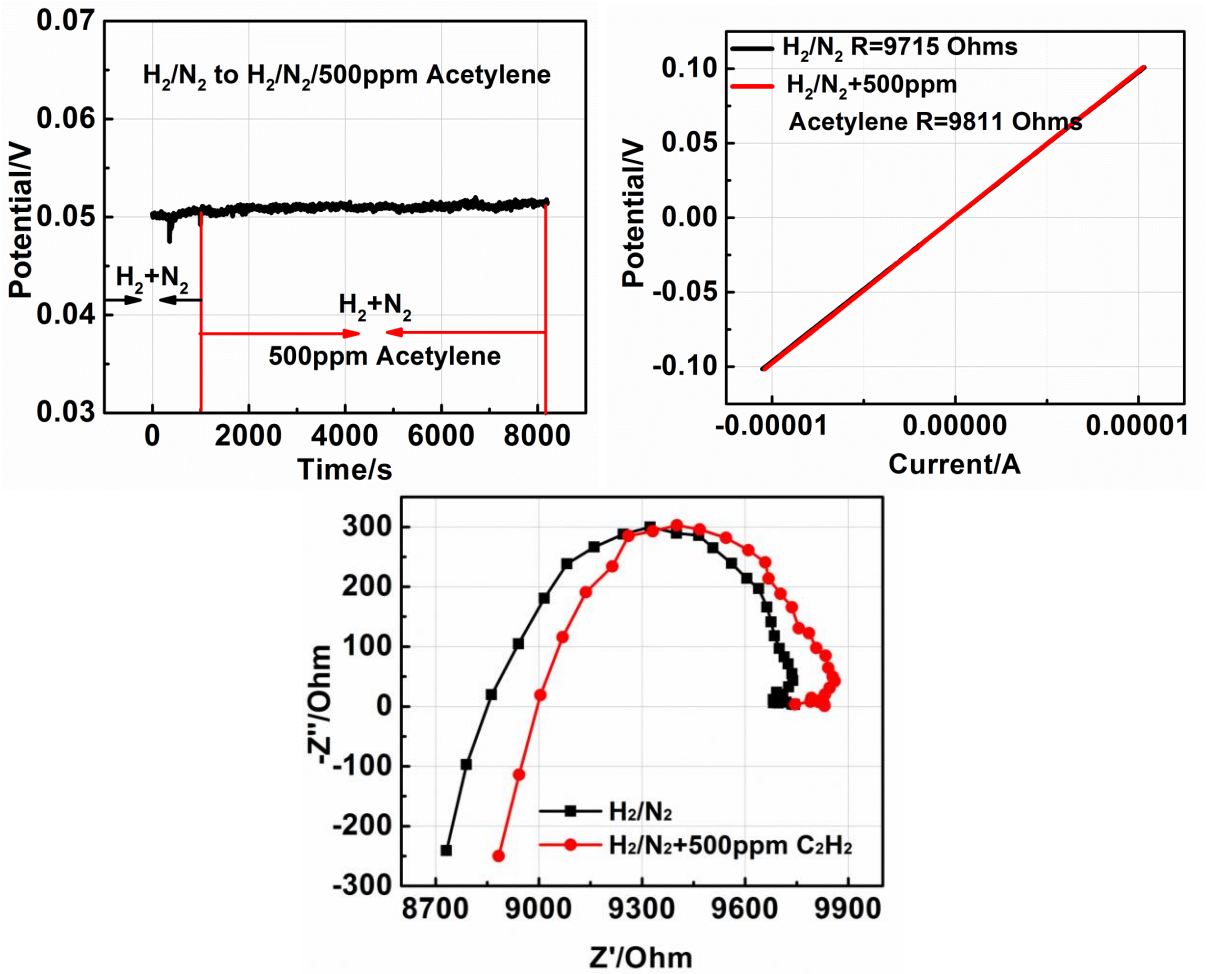

Figure 2.3.13. Nafion XL membrane conductivity measurements in a BekkTech cell flowing a mixture of H_2/N_2 without or with 500 ppm C_2H_2. Measurements were completed by chronopotentiometry (top, left), cyclic voltammetry (top, right) and impedance spectroscopy (bottom).

Milestone 2 Go/No Go decisions (section 1.1) included the contaminant concentration resulting in a performance loss ≥20 %. Figure 2.2.8 in section 2.2 indicates that the 20 % target was not achieved with Ca^{2+} partly because a liquid water path is necessary for the contaminant to reach the catalyst and ionomer (the gas diffusion layer is an effective barrier). For iso-propanol, the 20 % target was also not achieved because the cell voltage for concentrations exceeding ~8000 ppm was not stable owing to flooding (iso-propanol is a surfactant that presumably affected water management). For bromomethane, the loss exceeded 20 % because it was eventually established that a product accumulates over time for all concentrations used (Br^-, section 3.1, reference J21). For acetylene, the concentration dependency was strong which made it difficult to accurately control the desired concentration for a given performance loss. Therefore, a common performance loss could not be selected for all studied contaminants (the steady state contaminant impact was expected to be dependent on the cathode potential). This statement is important in relation to segmented cell measurements which require significant resources including analysis of a large amount of data. For acetylene, segmented cell tests were completed with a 300 ppm concentration.

Figure 2.3.14, left depicts the segmented cell (figure 2.3.6, top, right) local cell voltages and dimensionless current densities before, during, and after contamination by 300 ppm C_2H_2. Local cell voltages are equal and are essentially due to the relatively small 100 cm^2 active area (iso-potential). In contrast, a dimensionless current density redistribution is observed at the beginning of the contamination period due to the gradual adsorption on both catalyst and carbon (catalyst support, sub-layer, gas diffusion layer) surfaces along the flow field channel length. Segment 1 nearest the cell air inlet is the first impacted. As contaminant adsorbates cover segment 1 surfaces, downstream segments start to be impacted in succession (traveling wave). It is hypothesized that acetylene adsorption and surface processes are relatively slow in comparison to transport processes (figure 2.3.14, right). After all segments surfaces are covered with adsorbates, steady cell voltages and dimensionless current densities are observed but are still distributed with, presumably, a progressive decrease in acetylene concentration from the inlet to the outlet due to partial acetylene reduction. After the injection of acetylene is stopped, the cell voltage recovery is at first large and rapid and is followed by a slower recovery period that ultimately leads to a cell voltage equal to the pre-contamination level. The recovery behavior is attributed to the rapid desorption of acetylene reduction products and slower oxidation of other acetylene adsorbates with a transition occurring at ~0.6 V. These interpretations are consistent with gas chromatography/mass spectroscopy results reported in this section (discussion related to figures 2.3.22 and 2.3.24).

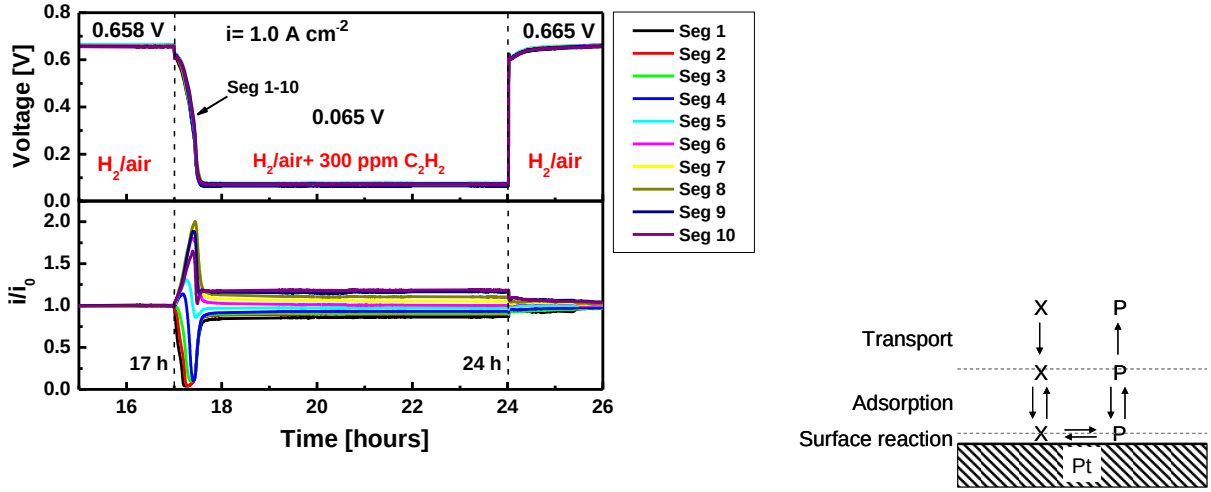

Figure 2.3.14. Local cell voltage and dimensionless current density transients before, during, and after contamination by 300 ppm C_2H_2 (left). Contaminant processes sequence for a contaminant X leading to a product P (right).

It is noted that localized high current densities (up to ~2 A cm^{-2}) during the rapid cell voltage decrease (figure 2.3.14, left) will create temporary high local temperatures and peroxide production rates (near the air outlet). The long term impact of such conditions may accelerate catalyst (agglomeration) and ionomer degradation.

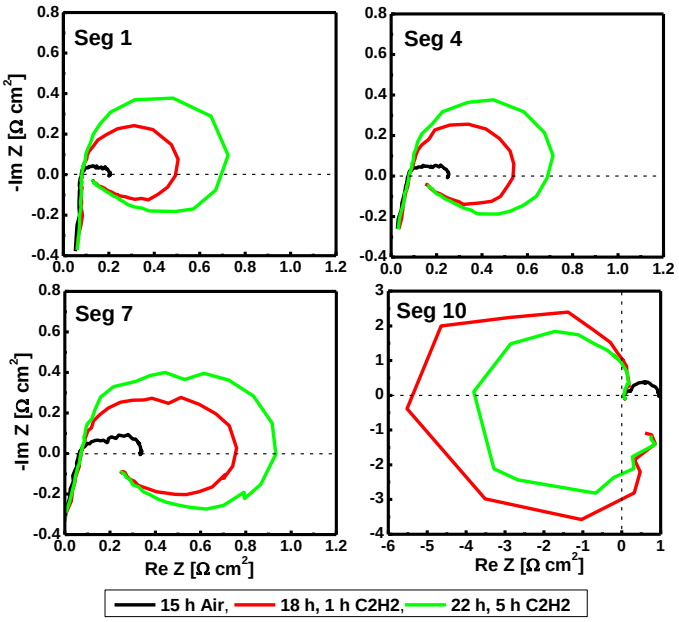

Figure 2.3.15. Local impedance spectra obtained before and during contamination by 300 ppm C_2H_2. Air baseline and after shorter contaminant exposure periods. 1 A cm^{-2}.

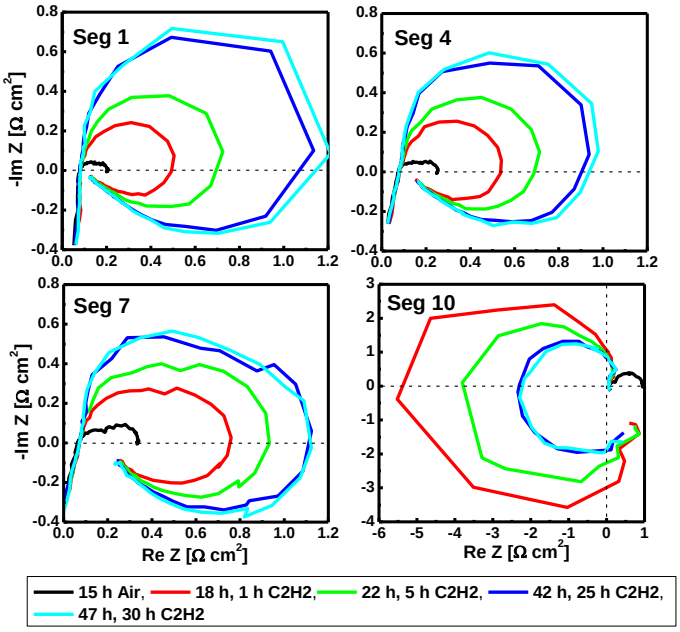

Figure 2.3.16. Local impedance spectra obtained before and during contamination by 300 ppm C_2H_2. Air baseline and after shorter and longer contaminant exposure periods. 1 A cm^{-2}.

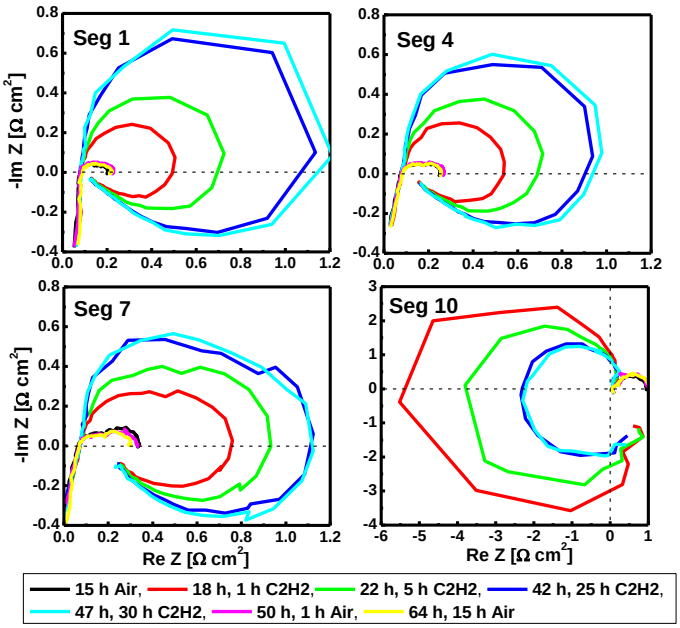

Figure 2.3.17. Local impedance spectra obtained before, during, and after contamination by 300 ppm C_2H_2. Air baseline and after contaminant exposure and recovery periods. 1 A cm^{-2}.

Impedance spectra (figures 2.3.15, 2.3.16 and 2.3.17) illustrate increases in both high (oxygen kinetics) and low (mass transfer) frequency loop sizes during acetylene contamination. Similar observations have already been mentioned in the first paragraph of section 2.3. The impedance increase in the presence of acetylene is accompanied by the appearance of an inductive behavior at low frequencies (positive imaginary impedance values), which is ascribed to the slow transformation of acetylene on Pt. Segment 10 shows an unusual behavior with impedance values in all 4 quadrants of the Nyquist plot and an initial increase followed by a decrease (a similar phenomenon is observed with a low oxygen stoichiometry, CO contamination, etc., but the actual cause remains to be identified for acetylene contamination). In addition, the impedance still evolves after 1 h acetylene exposure despite a steady state cell voltage and dimensionless current density (figure 2.3.14, left) but eventually a steady state is reached. The processes responsible for the slower impedance transient and different segment 10 behavior are currently unclear. The recovery process is rapid and the recovery is nearly complete, which is consistent with figure 2.3.14, left results.

Changes in local cell voltages (figure 2.3.18, left) and active catalyst areas (figure 2.3.18, right) before and after acetylene contamination also demonstrate a near complete recovery. The anode and cathode active catalyst area losses of respectively 8 and 14 % are typical of membrane/electrode assemblies that have not been contaminated.

In view of the limited number of tests completed with a segmented cell and the strong correlation between the local cell voltage (and by extension cathode potential) and the current density distribution (figure 2.3.14, left), it would be beneficial to characterize contamination for other contaminant concentrations, current densities and temperatures (section 2.2, first paragraph) to

assess local degradation risks resulting from a cumulative exposure to temporary high current densities (local hot spots and high hydrogen peroxide production rates).

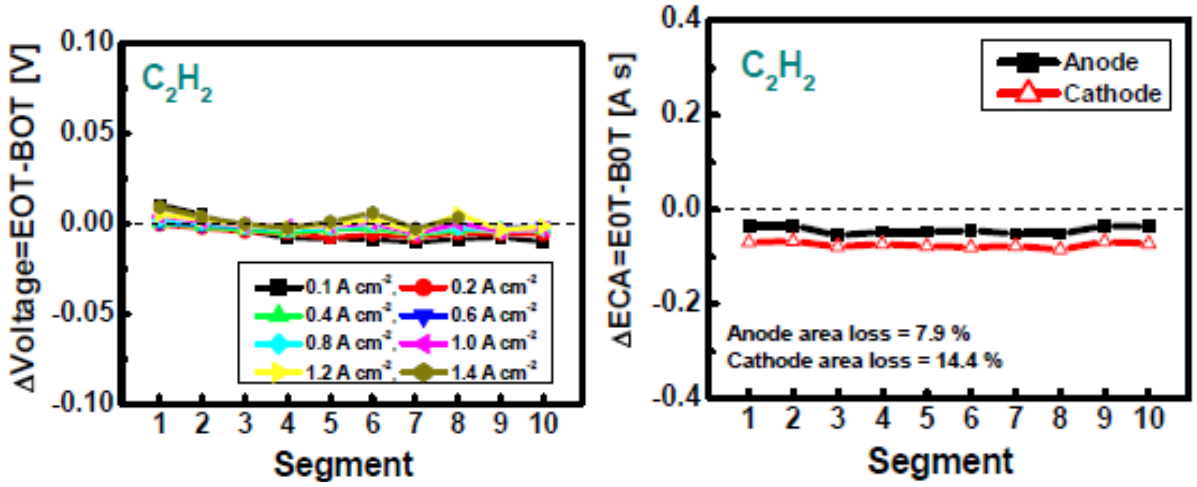

Figure 2.3.18. Changes in local cell voltages and catalyst electrochemical areas before and after contamination by 300 ppm C_2H_2.

Acetylene speciation was determined by gas chromatography and mass spectrometry using 3 different fuel cell operating modes (figure 2.3.19). Inlet reactant stream compositions and cell polarization were selected to respectively favor catalytic, electrochemical, and all reactions. For fuel cell operating modes that favor catalytic and electrochemical reactions (figure 2.3.19, left and center), characterization was supplemented by cyclic voltammetry, which was useful to guide the selection of cathode potentials for subsequent tests. Data interpretation was also facilitated by recording chronopotentiometry and chronoamperometry transients for cell polarization tests (figure 2.3.19, center and right).

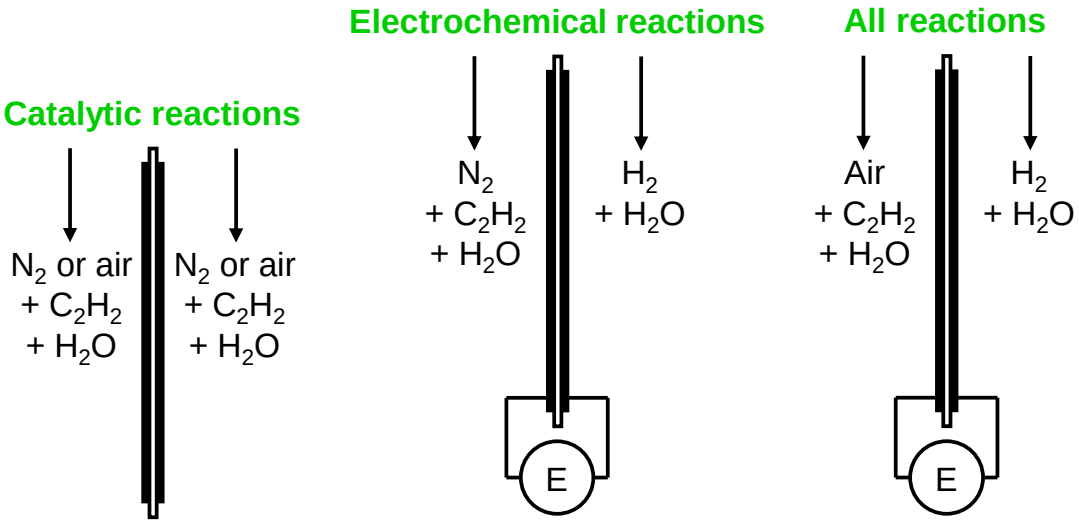

Figure 2.3.19. Fuel cell operating modes used to characterize outlet gas streams compositions with gas chromatography and mass spectroscopy. Inlet reactant gas compositions and cell voltages were selected to respectively favor catalytic (left), electrochemical (center), and all (right) reactions.

For the catalytic reactions fuel cell operating mode (C_2H_2 in N_2), data indicate that acetylene is inert (figure 2.3.20, top, left) because C_2H_2 and CO_2 peaks are not affected. However, C_2H_2 adsorbs on Pt due to the presence of an oxidation peak at 1 V vs the pseudo hydrogen reference electrode or HRE after the N_2 purge (figure 2.3.20, bottom, left). For acetylene in air, acetylene is largely converted to CO_2 in the presence of O_2 (equation 2.3.6) with the almost complete disappearance of the C_2H_2 peak, a concurrent large increase in CO_2 peak height (figure 2.3.20, top, right), and a conversion in excess of 95 % (figure 2.3.20, bottom, right).

$$2C_2H_2 + 5O_2 \rightarrow 4CO_2 + 2H_2O \quad (2.3.6)$$

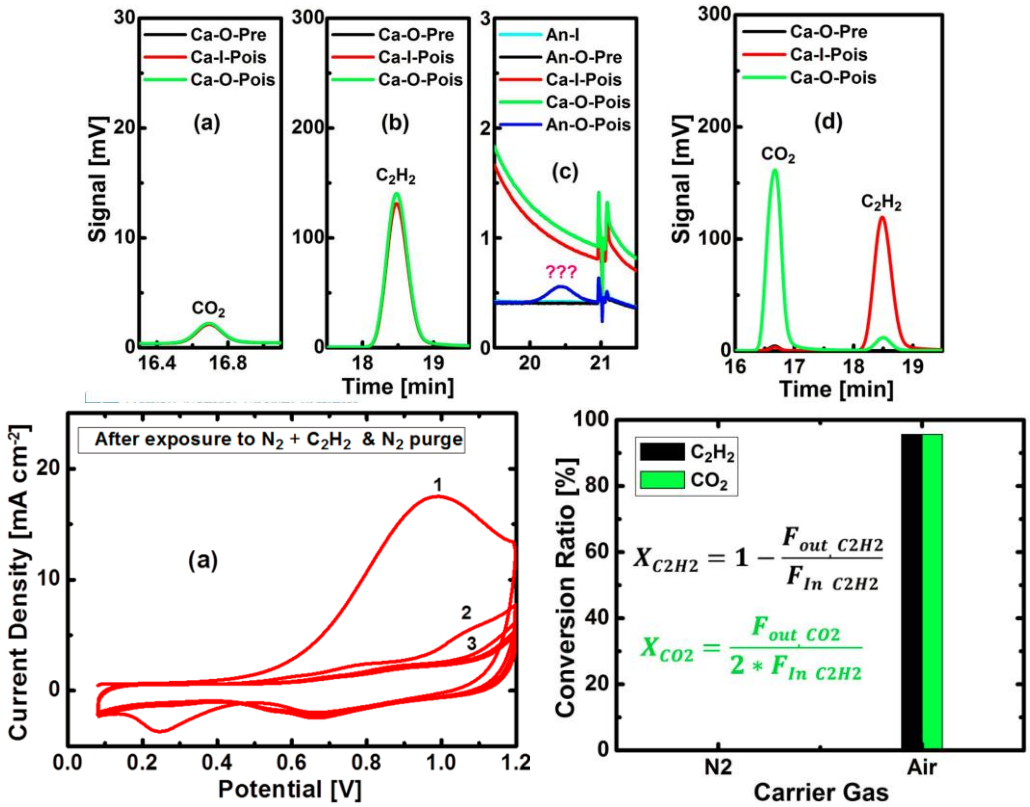

Figure 2.3.20. Gas chromatographs for a fuel cell fed with a mixture of C_2H_2 in N_2 (top, left) and C_2H_2 in air (top, right). Cyclic voltammograms for the fuel cell exposed to a mixture of C_2H_2 in N_2 after a N_2 purge (bottom, left). Conversion ratios for the fuel cell exposed to the C_2H_2 mixtures (bottom, right). Conversion definitions are differently defined to emphasize the observed mass balance (bottom, right).

For the electrochemical reactions fuel cell operating mode (C_2H_2 in N_2), results show that acetylene either undergoes a hydrogenation reaction (equation 2.3.7) or an electrochemical reduction (equation 2.3.8) at an open circuit potential (or OCP). This conclusion is supported by the change in open circuit potential (figure 2.3.21, top, left) brought by the mixed potential established between H_2/H^+ and C_2H_6/C_2H_2 electrodes. The conclusion is also supported by the disappearance of C_2H_2 and the appearance of 2 new peaks in the cathode outlet gas stream (C_2H_4 and C_2H_6?) in figure 2.3.21, bottom. Cyclic voltammograms at the end of the contamination and recovery periods (figure 2.3.21, top, right) reveal that acetylene is oxidized above 0.3 V vs HRE

(0.8 V vs HRE peak) and easily leaves the surface with an inert gas purge (after the purge the cyclic voltammogram is similar to the one before contamination although slightly offset).

$$C_2H_2 + 2H_2 \rightarrow C_2H_6 \quad (2.3.7)$$

$$C_2H_2 + 4H^+ + 4e^- \rightarrow C_2H_6 \quad (2.3.8)$$

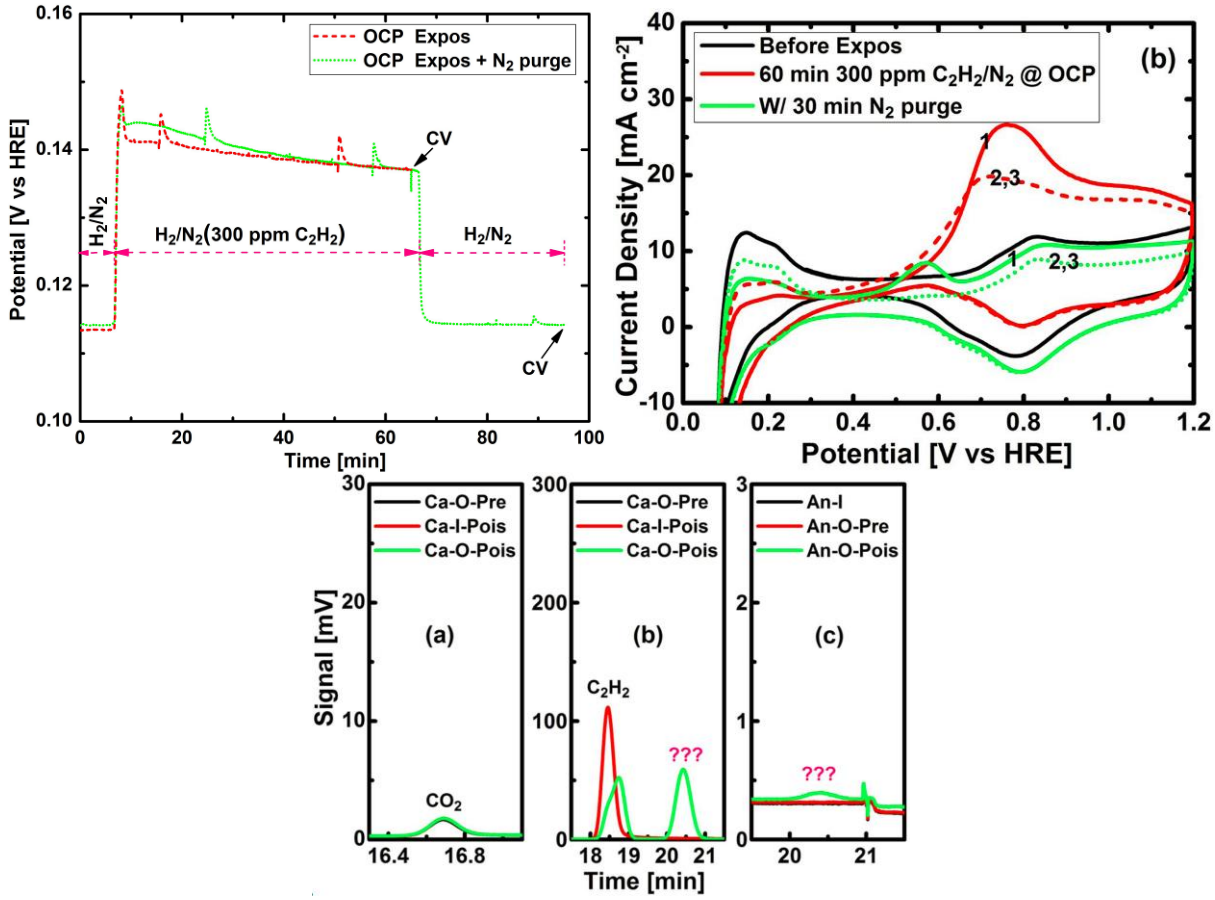

Figure 2.3.21. Chronopotentiometric transients (top, left) and cyclic voltammograms (top, right) for a fuel cell exposed to a mixture of C_2H_2 in N_2 at OCP. Gas chromatographs for a fuel cell fed with a mixture of C_2H_2 in N_2 at OCP (bottom).

For the higher cell voltages of 0.5, 0.65 and 0.9 V, the positive currents indicate that acetylene is also oxidized (equations 2.3.9 and 2.3.10, figure 2.3.22, top, left). The progressive decrease in the current density suggests the accumulation of intermediates on catalyst surfaces. The current decrease is less pronounced for high cell voltages because acetylene oxidation is favored. This information is supported by the corresponding cyclic voltammograms (figure 2.3.22, top, right, bottom, left and right), which show oxidation peaks at 0.7 and ~1 V vs HRE. The 0.7 V vs HRE is attributed to CO or CO like intermediates whereas for the ~1 V vs HRE peak intermediates remain to be identified. The 0.7 and ~1 V vs HRE peaks are less pronounced for the higher cell voltages because oxidation is favored leaving less intermediates on the catalyst surface. Additionally, the unidentified intermediate is not removed by an inert gas purge but is progressively oxidized at higher potentials.

$$C_2H_2 + 4H_2O \rightarrow 2CO_2 + 10H^+ + 10e^- \quad (2.3.9)$$

$$aC_2H_2 + bH_2O \rightarrow c\text{Intermediate}_{ads} + dH^+ + ne^- \quad (2.3.10)$$

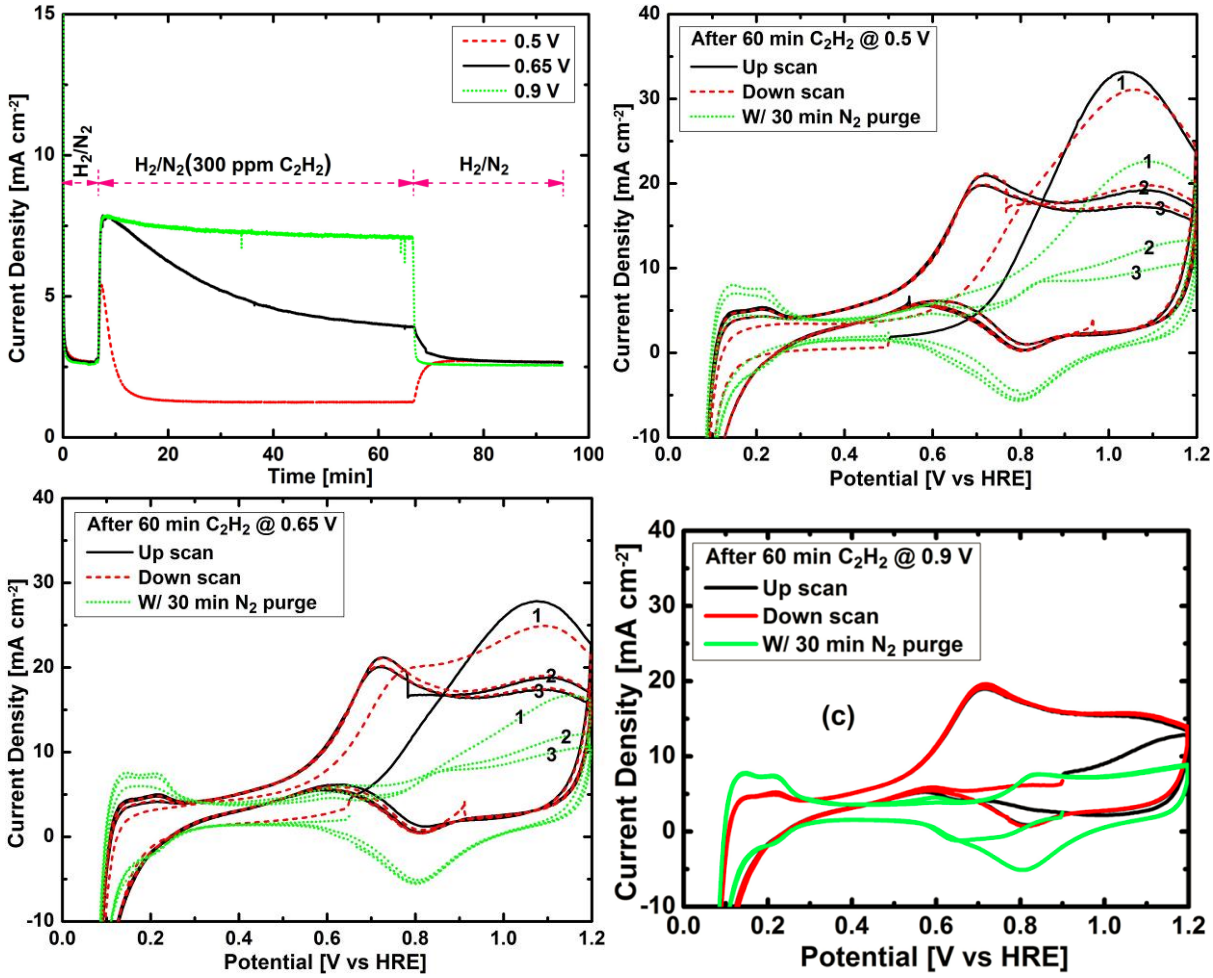

Figure 2.3.22. Chronopotentiometric transients (top, left) and cyclic voltammograms for a fuel cell exposed to a mixture of C_2H_2 in N_2 at 0.5 V (top, right), 0.65 V (bottom, left) and 0.9 V (bottom, right).

For acetylene in N_2, acetylene oxidization leads to CO_2 and CO (equation 2.3.11) in addition to the unidentified acetylene intermediate as demonstrated by the appearance of new peaks (figure 2.3.23, top). Acetylene conversion and products vary with potential (figure 2.3.23, bottom). Specifically, the extent of acetylene oxidation significantly increases with the cell voltage.

$$C_2H_2 + 2H_2O \rightarrow 2CO + 6H^+ + 6e^- \quad (2.3.11)$$

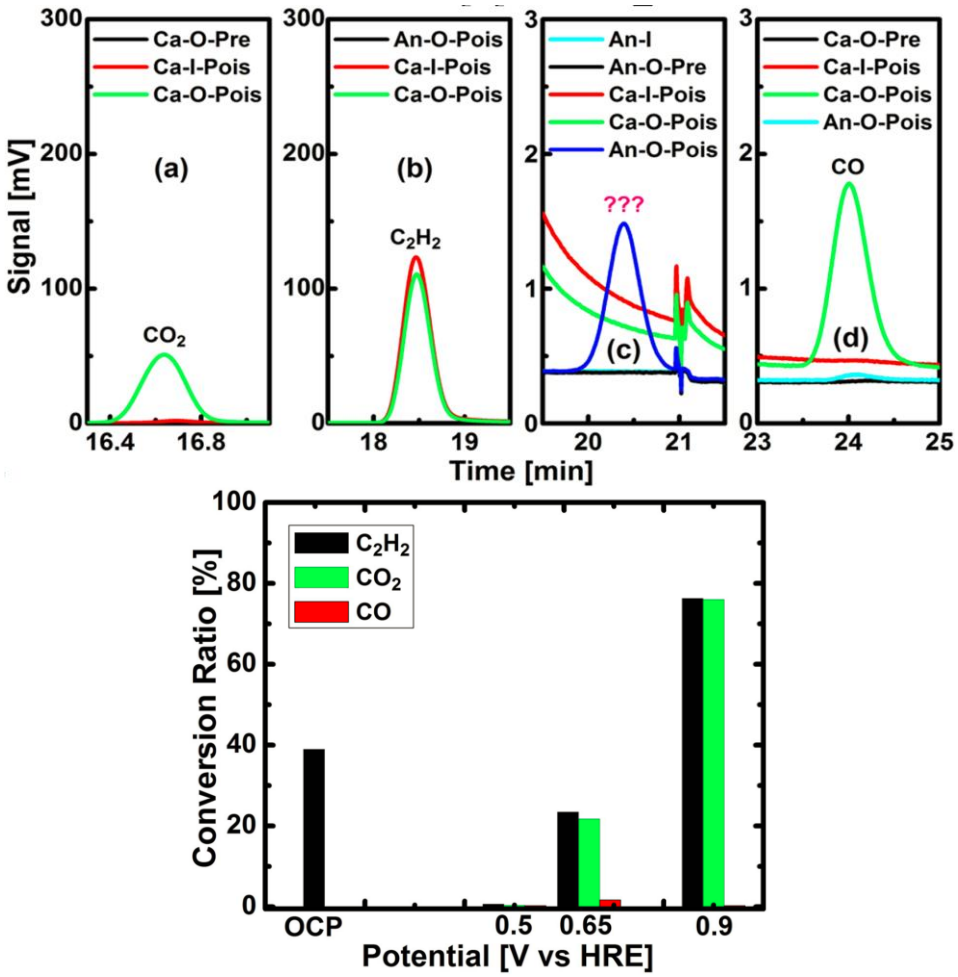

Figure 2.3.23. Gas chromatographs for a fuel cell fed with a mixture of C_2H_2 in N_2 (top). Acetylene conversion and product distribution (bottom). OCP is ~0.14 V during acetylene contamination (figure 2.3.21, top, left).

For acetylene in air, the cell performance loss is large and recovery is slow for potentials associated with the unidentified acetylene intermediate (figure 2.3.24, top) and the operating range of automotive applications (0.65 and 0.67 V vs HRE). Additionally, acetylene reactions lead to varying levels of CO_2, CO and an unidentified acetylene intermediate (figure 2.3.24, middle). However, despite the significant acetylene conversion (figure 2.3.24, bottom), the contaminant effect is still large on fuel cell performance, which support the development of filtering system specifications and other preventive and recovery procedures.

In summary, acetylene speciation studies with different fuel cell configurations (figure 2.3.19) have revealed that the contamination mechanism is complex involving several chemical and electrochemical reactions (equations 2.3.6 to 2.3.11) and products that are potential dependent. Such a situation may complicate performance recovery and suggest the use of several cell potentials to evaluate the effectiveness of recovery procedures.

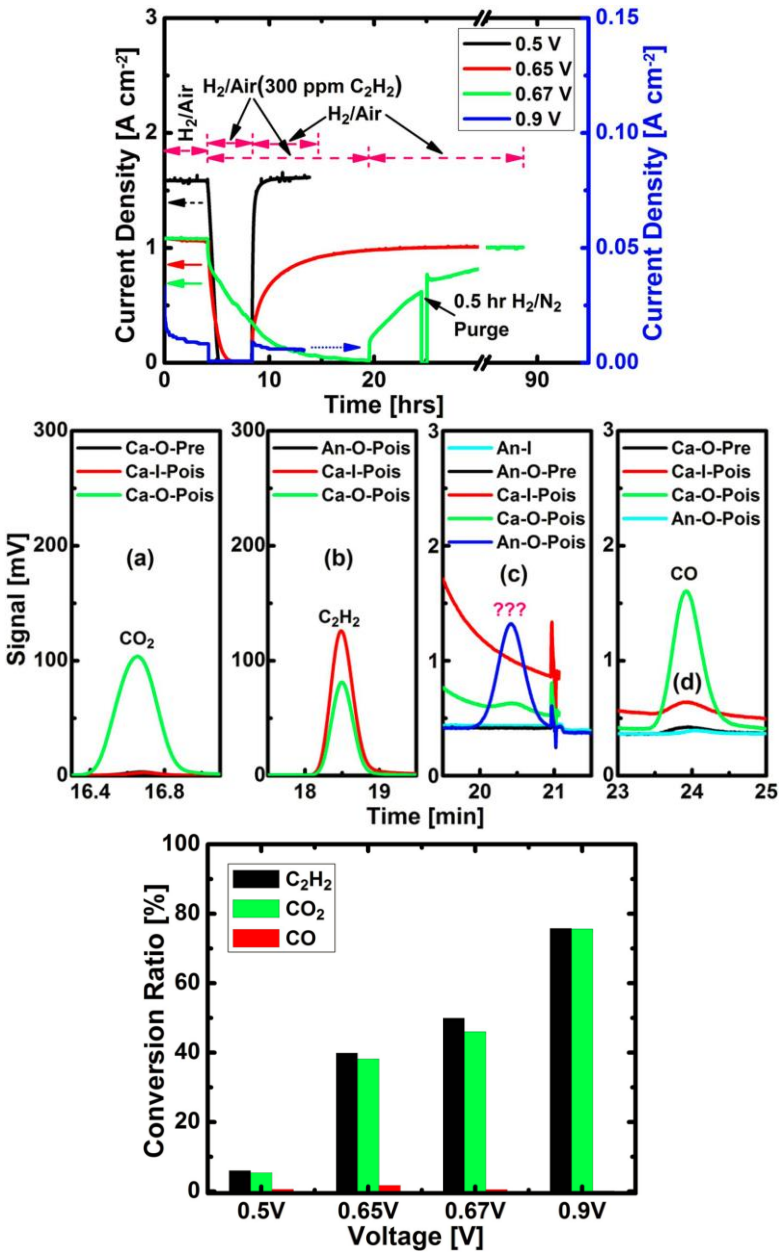

Figure 2.3.24. Chronopotentiometric transients (top) for a fuel cell exposed to a mixture of C_2H_2 in air. Representative gas chromatographs (middle). Acetylene conversion and product distribution (bottom).

Impedance data collected during milestone 2 (operating conditions effects, figures 2.3.1 and 2.3.2) will be analyzed to obtain additional mechanistic clues (figure 2.3.25).

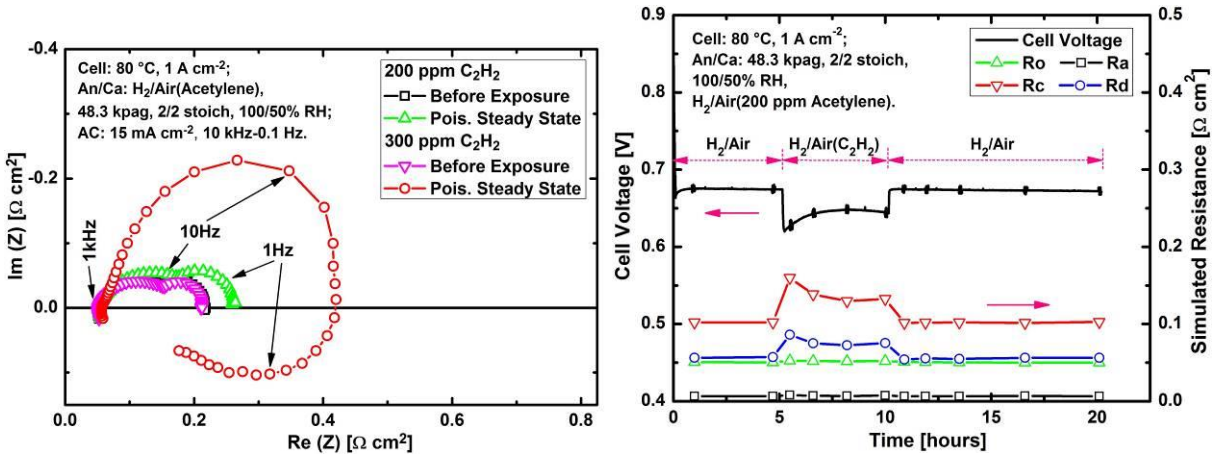

Figure 2.3.25. Impedance spectra for a fuel cell before and during an exposure to acetylene (left). Kinetic (anode and cathode), ohmic and mass transfer resistance transients derived from impedance spectroscopy data (right).

2.3.2 *Acetonitrile (section 3.1, reference J20)*

Fuel cell impedance measurements have shown that acetonitrile increases the high frequency ohmic resistance (figure 2.3.1). However, *ex situ* membrane conductivity measurements by chronopotentiometry have also shown that acetonitrile does not have an impact on membrane conductivity (figure 2.3.26). An acetonitrile decomposition intermediate or product was deemed responsible for the change in ohmic resistance during fuel cell operation.

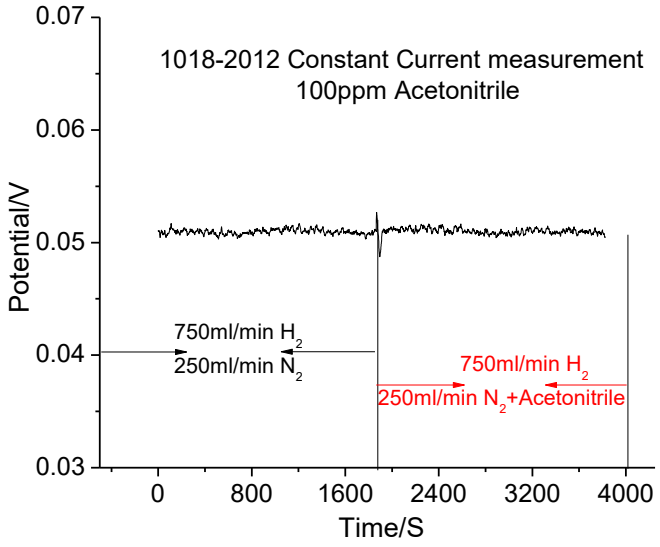

Figure 2.3.26. Nafion XL membrane conductivity measurements in a BekkTech cell flowing a mixture of H_2/N_2 without or with 100 ppm CH_3CN. Measurements were completed by chronopotentiometry.

A nitrogen (N) compound was detected in the fuel cell outlet liquid water samples using an ammonium ion selective electrode when the cell is contaminated with acetonitrile. Additional ion

chromatography tests confirmed that the N compound is exclusively the ammonium ion NH_4^+ because the ion selective electrode cannot discriminate against the existence of an organic species containing a nitrogen based group. Ammonium cations displace the ionomer and membrane protons by ion exchange and decrease ionic conductivity. Acetonitrile hydrolysis (figure 2.3.27) is a possibility (acetaldehyde and acetic acid were also detected but not hydrogen cyanide or methane). Other paths to NH_4^+ may also exist.

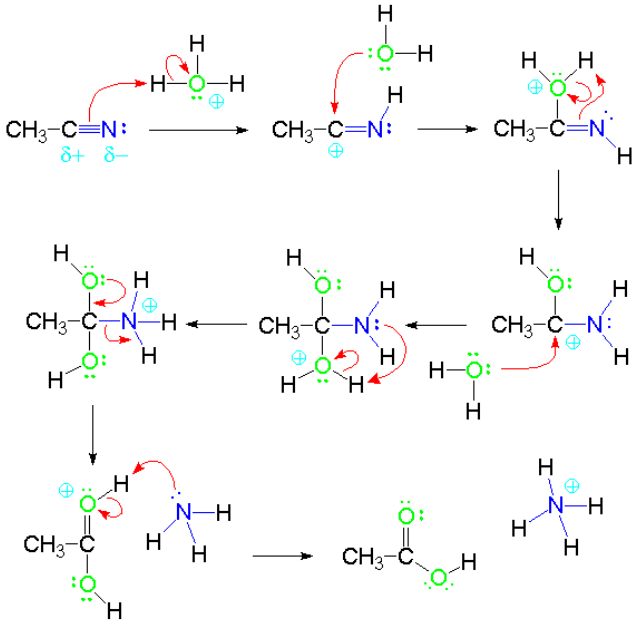

Figure 2.3.27. Acetonitrile hydrolysis reactions leading to acetic acid and ammonium products.

2.3.3 *Ca^{2+} (section 3.1, references J4, J11, J12, J18)*

In section 2.1, it was mentioned that fuel cell operating conditions were changed to accelerate contamination by cations. The modified conditions highlighted the possibility of salt precipitation within the fuel cell and its strong link with water management. Calcium salt precipitation locally takes place on the bipolar plate (near the cell outlet) and gas diffusion layer surfaces as well as within the gas diffusion layer (figure 2.3.28). The Ca to S atomic ratio is consistent with the formation of $CaSO_4.xH_2O$. Salt precipitation negatively influences oxygen mass transfer and blocks access to the catalyst. Salt precipitation has not been reported in prior studies.

Local polarization curves obtained with a segmented cell before contamination (figure 2.3.29, left) indicate a fairly regular distribution with larger current densities near the cell inlet. Such a distribution is expected on the basis of the gradual consumption of oxygen along the flow field length. Segments that are out of sequence are attributed to the cell design and data acquisition system. After contamination by Ca^{2+} (figure 2.3.29, right), changes in the kinetic (low current densities), ohmic (linear region between low and high current densities), and mass transfer (high current densities) regions are noted. Such modifications in cell voltage have been discussed [3] but not on a local basis, which emphasizes the need to include such a cation contamination effect into models for more accurate predictions.

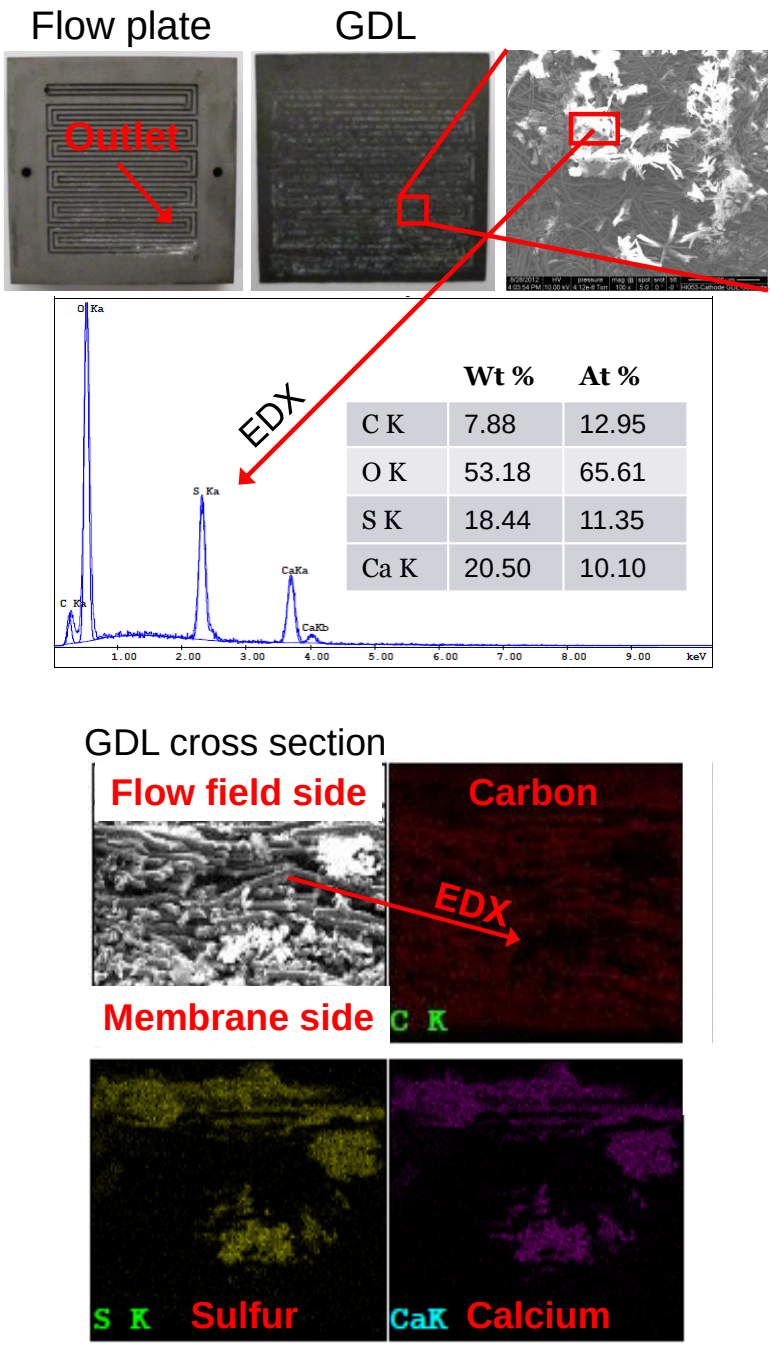

Figure 2.3.28. Photographs of the cathode flow field plate and gas diffusion electrode after contamination by Ca^{2+} (top). Scanning electron microscopy and energy dispersive X-ray spectroscopy of the white deposits on the gas diffusion layer surface indicate the presence of $CaSO_4$ crystals. Similar tests completed with a cross section of the gas diffusion layer also revealed $CaSO_4$ crystals within the structure (bottom). The top figure is reprinted and reformatted with permission from *J. Electrochem. Soc.*, **161**, F1006 (2014). Copyright 2014, The Electrochemical Society.

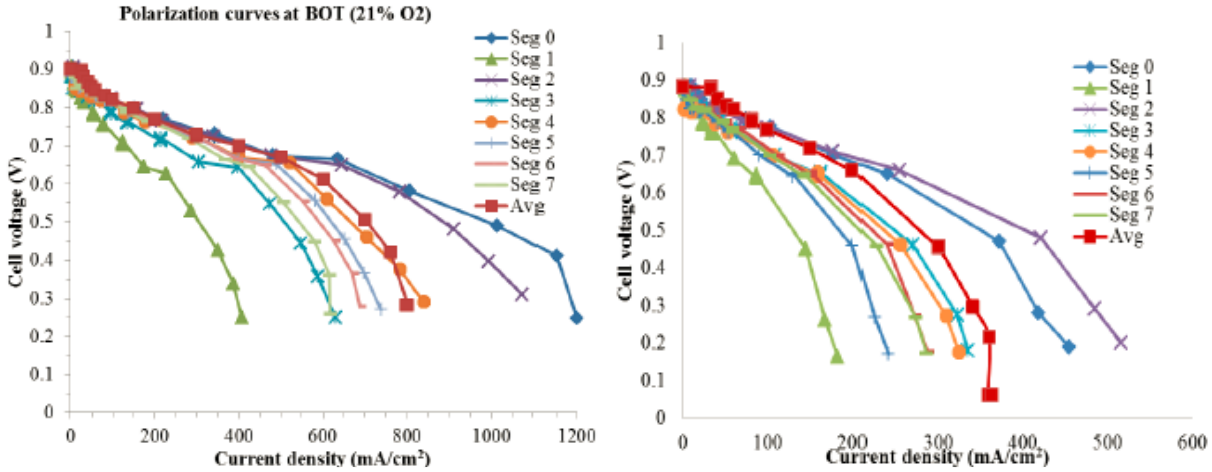

Figure 2.3.29. Polarization curves obtained with a segmented cell before (left) and after (right) contamination by Ca^{2+}.

The active catalyst surface area was measured by cyclic voltammetry (figure 2.3.30, left) before and after contamination by a foreign cation and was found to decrease (change in positive hydrogen oxidation current from 0.1 to 0.3 V). This is attributed to ion exchange of Ca^{2+} with H^+ leading to ionomer contraction due to expelled water, a decrease in the catalyst coverage by the ionomer and a lower catalyst active surface area. This mechanism is different than specific cation adsorption on the catalyst which is not expected in view of a generally more stable water solvation sheath. The adsorption of perchlorate anions is negligible on Pt. Figure 2.3.30, right summarizes the decreases in catalyst electrochemical surface area for several perchlorate salts. Differences reflect cation properties such as charge and size.

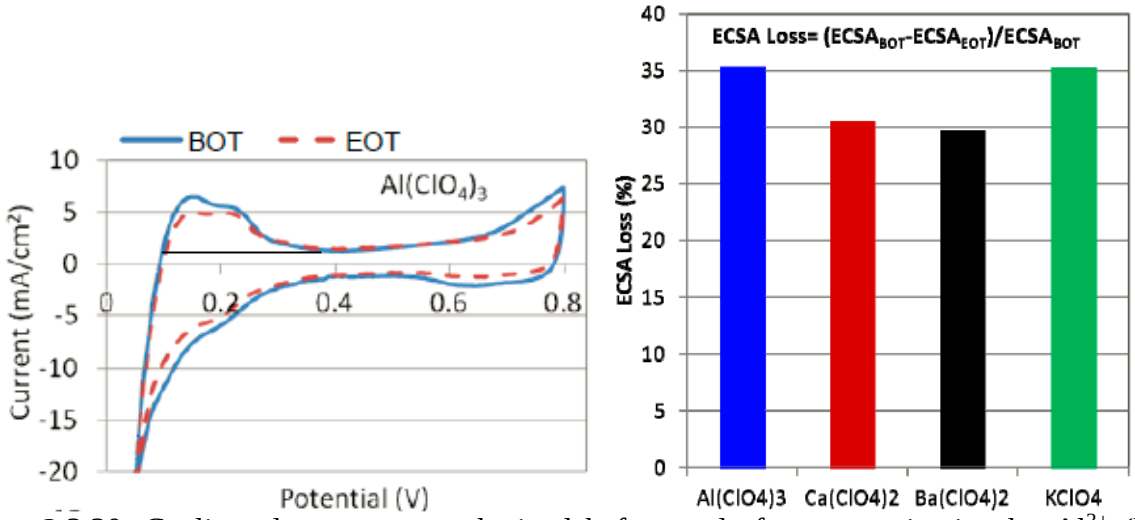

Figure 2.3.30. Cyclic voltammograms obtained before and after contamination by Al^{3+} (left). Summary of the losses in catalyst electrochemical surface area resulting from contamination by different cations (right).

The segmented cell also showed that transient, local, normalized currents are progressively redistributed and do not reach a steady state at the end of the Ca^{2+} contamination period (figure 2.3.31). The still evolving situation, even after 100 h of testing, supports the notion that Ca^{2+}

accumulation in the ionomer and membrane is still progressing and that contamination is initiated near the cell inlet (lowest current at segment 0) and is sequentially followed at downstream segments (segment 1 current starts to decrease after segment 0, etc.). Recovery does not significantly take place after contaminant injection is stopped. This is presumably due to the low concentration of protons in the injected water that does not favor ion exchange with Ca^{2+} ions.

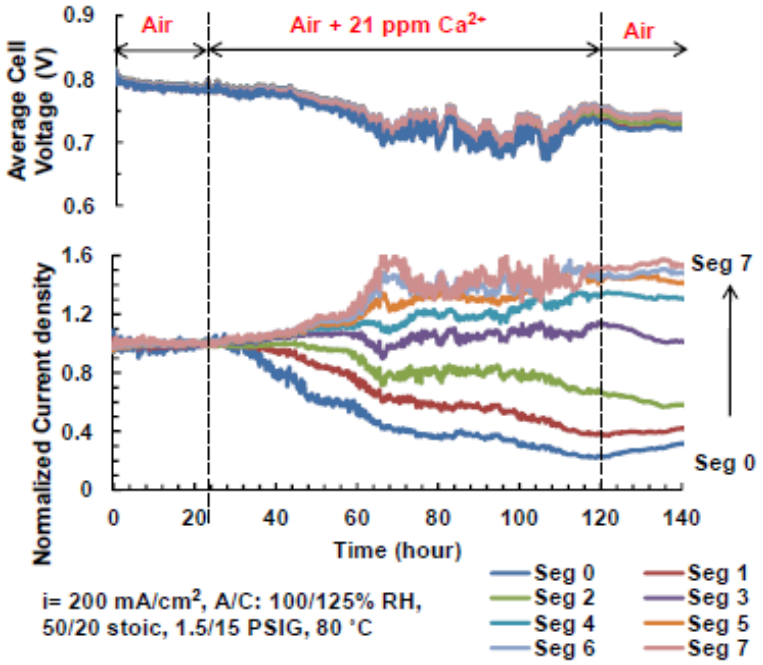

Figure 2.3.31. Segmented cell voltage and normalized current density transients for a temporary Ca^{2+} contamination period. Reprinted and reformatted with permission from *ECS Trans.*, **61** (12), 49 (2014). Copyright 2013, The Electrochemical Society.

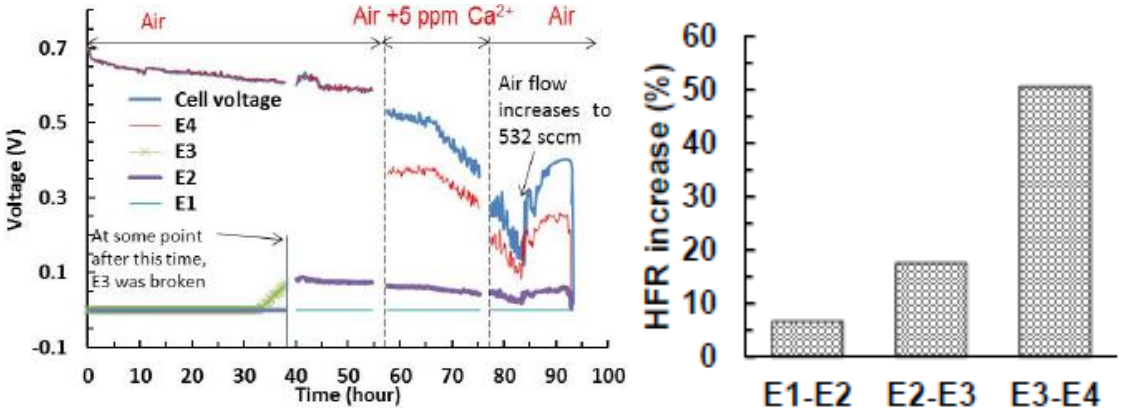

Figure 2.3.32. Through-plane segmented membrane/electrode assembly (figure 2.3.7, top, right and bottom) cell voltage and potential difference transients before, during and after a temporary Ca^{2+} contamination period (left). High frequency resistance increases calculated from potential differences between Pt electrodes inserted in the 5 layer membrane (right). Probe E1 is close to the anode. Reprinted and reformatted with permission from *ECS Trans.*, **61** (12), 37 (2014). Copyright 2014, The Electrochemical Society.

The presence of 2 different cations in the membrane (H^+, Ca^{2+}) modifies the concentration and potential distributions. The unreactive Ca^{2+} accumulates at the cathode modifying the thermodynamic potential, kinetic overpotential, ohmic overpotential and transport of O_2, H^+ and H_2O [3] due to different membrane properties associated with a Ca^{2+} form ionomer. A membrane/electrode assembly was fabricated using a stack of 5 separate membranes (figure 2.3.7, top, right and bottom). Thin Pt probes were inserted between the membranes to measure the local potential drops and confirm the presence of a steep potential gradient. Figure 2.3.32, left illustrates the cell voltage and Pt probe potentials before, during and after a temporary Ca^{2+} contamination period. The Pt probe potentials are significantly affected by the presence of Ca^{2+} especially near the cathode. Potential differences between Pt probes were used to calculate high frequency resistances with Ohm's law (figure 2.3.32, right), which demonstrated *in situ* the existence of a steep potential gradient within the relatively thin membrane. In contrast, a previous *ex situ* attempt used in-plane membrane measurements (several cm in length sample) to establish the cation concentration distribution [14]. The steep potential gradient has a positive benefit because the ion exchange at the interface is limited because the foreign ion concentration is larger than its average value.

In section 2.2, the effect of operating conditions on the outcome of Ca^{2+} contamination was reported. A sample of these data are replotted in figure 2.3.33. As indicated, these tests included contaminant exposures of 100 h. It was established by hydrogen crossover measurements (table 2.3.1) that despite the relatively short cell operation time, a significant increase in gas leakage (membrane pinhole formation?) was caused by contamination especially with a higher Ca^{2+} concentration and current density. Such conditions are expected to create the largest local Ca^{2+} concentration at the cathode (largest potential gradient in the ionomer/membrane pushing cations against the cathode). In turn, this situation enables localized electro-striction. The higher cation charge (2+ versus 1+ for the proton) pulls sulfonate sites closer together and expels water which acts as a membrane plasticizer. The drier membrane is more susceptible to damage by mechanical stresses with a locally more brittle material.

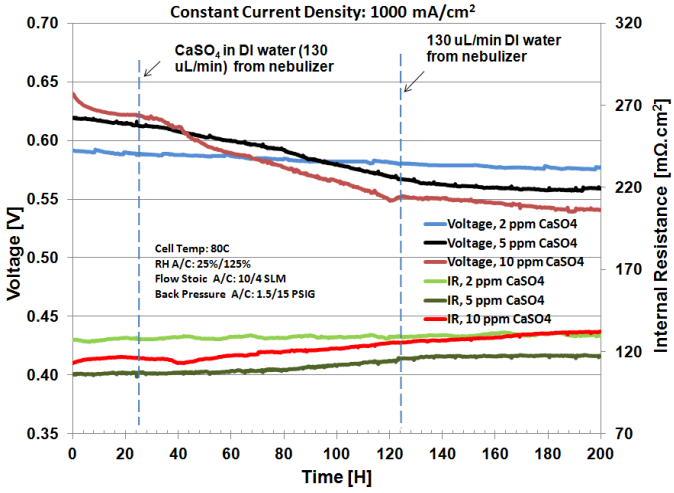

Figure 2.3.33. Effect of contaminant concentration on cell voltage and cell resistance for a fuel cell temporarily contaminated with Ca^{2+} (replotted data from figure 2.2.6, top and bottom, left). Reprinted and reformatted with permission from *ECS Trans.*, **58** (1), 529 (2013). Copyright 2013, The Electrochemical Society.

Table 2.3.1. Summary of membrane crossover measurements before and after contamination by Ca^{2+}.

Cell No.	H_2 CO (BOT) mA/cm²	H_2 CO (EOT) mA/cm²
1000 mA/cm² with 2 ppm $CaSO_4$	2.68	2.93
1000 mA/cm² with 5 ppm $CaSO_4$	2.75	90.7
1000 mA/cm² with 10 ppm $CaSO_4$	2.94	Very large CO
600 mA/cm² with 5 ppm $CaSO_4$	2.56	8.68
200 mA/cm² with 5 ppm $CaSO_4$	2.89	3.55

Table 2.3.2. Summary of *ex situ* and *in situ* diagnostic methods' results for 7 airborne contaminants and 1 foreign cation to resolve contamination mechanisms.

Contaminant	Kinetic current (% loss in air at 30 °C and 0.9 V vs RHE)	Electrochemical catalyst area (% loss in N_2 at 30 °C)	H_2O_2 current (% gain in air at 30 °C and 0.5 V vs RHE)[a]	Membrane conductivity (% loss at 80 °C and 50 % relative humidity)	GDE water content	Dimensionless local current (maximum % loss and gain in air at 80 °C)		Contaminant conversion (% in air at 80 °C)[b]
						Contamination phase	Recovery phase	
Acetonitrile	79-84 (16.9 mM)	>76 (16.9 mM)	850-1300 (16.9 mM)	0 (100 ppm), N product detected by ISE (IC confirmed NH_4^+ product)	TBD	Step change followed by a cell potential triggered evolution reaching –15 to 12 at steady state (20 ppm)	Traveling current wave reaching –28 to 22 to values approximately equal to initial values (20 ppm)	20 to 45 for 0.55 to 0.65 V (20 ppm)
Acetylene	100 (4030 ppm)	100 (4040 ppm)	2700-3800 (4030 ppm)	1-2 (500 ppm)	TBD	Traveling current wave of –99 to 100 synchronized with voltage transient followed by –17 to 18 at steady state (300 ppm)	Step change to values approximately equal to initial values (300 ppm)	0.8 to 100 for 0.55 to 0.85 V (300 ppm)
Bromomethane	54 (400 ppm)	43 (400 ppm)	56 (400 ppm)	No ohmic loss in fuel cell	TBD	Gradual change starts after voltage steady state reaching –19 to 13 (5 ppm)	Trend continues reaching –21 to 21 (5 ppm)	0 for 0.1 to ~1 V (10 ppm)
Iso-propanol	12 (1 mM)	7 (1 mM)	18 (1 mM)	No ohmic loss in fuel cell	TBD	Step change of –9 to 5 (5300 ppm)	Reverse step change (5300 ppm)	Not applicable
Methyl methacrylate	65 (1 mM)	43 (H_{UPD}) and 82 (PtO reduction) (1 mM)	1300 (1 mM)	No ohmic loss in fuel cell	TBD	Step change of –7 to 6 (20 ppm)	Reverse step change (20 ppm)	49 to 57 for 0.55 to 0.68 V (20 ppm)
Naphthalene	66 (sat soln)[c]	90 (sat soln)[c]	780 (sat soln)[c]	No ohmic loss in fuel cell	TBD	Traveling current wave of –25 to 14 synchronized with voltage transient (2.3 ppm)	Traveling current wave of –39 to 40 synchronized with voltage transient (2.3 ppm)	Detectable but not quantifiable for 0.5 to 0.85 V (1.4 ppm)
Propene	53 (1010 ppm)	26 (H_{UPD}) and ~50 (PtO reduction) (1010 ppm)	620-960 (1010 ppm)	No ohmic loss in fuel cell	TBD	Step change of –8 to 6 (100 ppm)	Reverse step change (100 ppm)	43 to 89 for 0.55 to 0.85 V (100 ppm)
Ca^{2+}	37 (90 mM $Ca(ClO_4)_2$), 21 (5 ppm)[d]	2 (90 mM $Ca(ClO_4)_2$), 16-46 (5 ppm)[d]	660 (90 mM $Ca(ClO_4)_2$)	1.1-11 (5 ppm)[e]	TBD	Gradual change up to –50 to 20 (5 ppm)[f]	Gradual change up to –60 to 40 (5 ppm)[f]	-

[a] The total current is still mostly due to oxygen reduction in spite of a large peroxide production rate increase. [b] In all cases, observed products include the unaltered contaminant, CO and CO_2. [c] 0.25 mM solubility at 25 °C. [d] Derived from in situ polarization curve and cyclic voltammetry tests. [e] In situ result by current interrupt for 0.6-1 A cm^{-2} and 125 % relative humidity before a steady state is reached at 100 h. [f] 0.6 rather than 1 A cm^{-2} and before a steady state is reached at 100 h. ISE: ion selective electrode, IC: ion chromatography.

2.3.4 *Summary for all contaminants*

Table 2.3.2 summarizes key metrics obtained from the *in situ* and *ex situ* diagnostic tests. Electrochemical catalyst areas and peroxide production currents indicate that the change in kinetic resistance associated with contamination (figure 2.3.2, top, left) is not only due to a

decrease in surface area, but also to a modification of the oxygen reduction mechanism in favor of a 2 rather than a 4 electrons path leading to increased amounts of hydrogen peroxide. For Ca^{2+}, the electrochemical surface area is also affected (figure 2.3.30, left) but the change is not expected to be due to adsorption on the catalyst surface. Generally, organic contaminants undergo chemical or electrochemical reactions within the fuel cell as detected by gas chromatography/mass spectrometry analysis of outlet gases. Only bromomethane was electrochemically inactive (section 3.1, references J21, J24). Iso-propanol could not be analyzed because the sample gas stream drying step, which is necessary to avoid equipment damage, entrains a significant portion of iso-propanol. Ca^{2+} is not expected to be converted to Ca in the fuel cell because the electrode potentials are not sufficiently low. Acetonitrile and Ca^{2+} were the only contaminants that led to an ohmic resistance change. For acetonitrile, the change was ascribed to a decomposition product because the membrane conductivity measured *ex situ* was not affected by acetonitrile (figure 2.3.26). Ammonium was detected in the fuel cell outlet water. For Ca^{2+}, ion exchange with the ionomer proton modifies ionic conductivity as well as other physico-chemical parameters. The current distribution was minimally affected by iso-propanol, methyl methacrylate and propene. This observation is consistent with relatively slow catalyst surface kinetics, rapid transport processes, and a relatively uniform contaminant concentration across the cell. However, the other contaminants revealed varied behaviors that may be useful to facilitate mechanism identification and generalize contamination mechanisms. It is hypothesized that a change in rate determining step along the sequence of contaminant transport to the catalyst surface, catalyst surface kinetics, contaminant and products transport away from the catalyst surface is responsible for the change in behavior. From that standpoint, it is likely that a change in operating conditions would modify the cell response to iso-propanol, methyl methacrylate and propene. The gas diffusion electrode water content has not yet been measured because the increase in mass transport loss in the presence of organic contaminants was largely attributed to contaminant adsorption on the catalyst (discussion related to figure 2.3.3). However, this aspect is worth pursuing to confirm its existence.

The presence of elevated levels of peroxide for all contaminants (table 2.3.2) is expected to affect cell durability and is explored in section 2.4. The presence of contaminant products, the uneven current distribution, and the variety of contamination behaviors may complicate performance recovery strategies.

Table 2.3.3 provides a different yet complementary qualitative summary to table 2.3.2 of reaction mechanisms. It is emphasized that the oxygen reduction Tafel slope generally increases in the presence of organic contaminants (this feature remains to be demonstrated for Ca^{2+}). Only bromomethane and Ca^{2+} did not lead to a significant recovery after contaminant exposure was interrupted. A method based on a sequence of specific operating conditions was devised to recover performance after bromomethane contamination (section 1.3). For Ca^{2+}, a few options were explored but the extent of recovery still needs to be improved. Contamination mechanisms were separated into overpotential types because they conformed to the study methods. More quantitative reaction mechanisms were requested by project reviewers. However, such an objective would require a significant amount of resources. For example, figure 2.3.14 (current redistribution during acetylene contamination) suggests at least a 2D model (or a 1D + 1D simplified model) to represent the main mechanistic features. In addition, equations 2.3.6 to 2.3.11 (acetylene reactions) imply the knowledge of all intermediates adsorption isotherms and

reaction rate constants, and their relationships with oxygen reduction parameters. Similar conclusions apply to Ca^{2+} contamination. A new feature was added to the cation contamination model (the oxygen permeability is dependent on the cation concentration in the ionomer, section 3.5.3). Ion exchange at the ionomer surface and a treatment of the liquid water within the gas diffusion electrode (cation transport path) still need to be added. However, two-phase flow in the gas diffusion electrode is an active research area that is not yet settled. Therefore, research efforts should rather concentrate on preventive and recovery strategies and the development of simpler performance loss correlations (section 3.1, reference J19).

Table 2.3.3. Summary of contamination and recovery mechanism features for both organic and cation species.

Cathode contaminant type	Performance losses			Recovery
	Kinetic	Ohmic	Mass transfer	
Organic (acetonitrile: an, acetylene: ae, bromomethane: b, iso-propanol: i, methyl methacrylate: m, naphthalene: n, propene: p)	• Catalyst surface area loss due to contaminant adsorption (all) • Interactions between catalyst adsorbates lead to ORR mechanism changes -More peroxide (all) with long duration test in progress to assess impact (TBD) -Tafel slope increase (an, ae, m, n, p)	• Acetonitrile intermediate displaces protons in the ionomer (NH_4^+)	• Observed increase in impedance loop at low frequencies (all) requires assignment confirmation -Initial explanation: decrease in active surface area increases oxygen path to reaction sites -Recent re-interpretation based on additional impedance data: contaminant coverage potential dependency -Contaminant adsorption on C modifying water management (TBD) • Distributed effects along the channel length (scale up) (an, ae, b, n)	• 90 % of initial cell performance restored after contaminant injection stopped at 80 °C (an, ae, i, m, n, p) • For bromomethane, supersaturated operation and potential excursions recovers performance within 90 %
Foreign cation (Ca^{2+})	• Catalyst surface area loss due to foreign cation accumulation in the ionomer • Interactions between catalyst adsorbates and cation lead to ORR mechanism changes -More peroxide with long duration test in progress to assess peroxide and electrostriction (membrane crossover resulting from brittleness increase) impact (TBD) -Tafel slope change?	• Ca^{2+} displaces protons in the ionomer which is also leading to kinetic and mass transfer losses during operation	• Salt precipitation causes flow field and gas diffusion layer blockages -Increase in gas diffusion layer hydrophilicity (water management) (TBD) • Distributed effects along the channel length (scale up)	• Ex situ and in situ methods (acid and surfactant) did not fully recover performance -MEAs were contaminated by both ex situ soaking or in situ injection

2.4 Real world operation (task 2.1)

In section 2.3, it was mentioned that all 8 contaminants selected for detailed studies led to larger hydrogen peroxide production rates (table 2.3.2). In addition, Ca^{2+} contamination led to larger membrane crossover rates under specific operating conditions (table 2.3.1). It was deemed important to carry out longer term tests with both types of contaminants to assess degradation. These tests were also supplemented by a contaminant mixture test to evaluate interactions between different species. For these tests, a lower cathode Pt loading of 0.1 mg cm^{-2} and reduced contaminant concentrations were used to better reproduce field conditions. The Ca^{2+} concentration was not altered in view of its smaller contamination rate.

2.4.1 *Long duration acetonitrile exposure*

A concentration of 5 ppm was selected which is close to its concentration in atmospheric air (~2 ppm). An extensive set of tests were considered to extract the maximum amount of information from the long term test. These include non-destructive as well as destructive tests: polarization, cyclic voltammetry, high frequency resistance, impedance spectroscopy, linear sweep voltammetry, chronoamperometry, ion chromatography, inductively coupled plasma mass spectrometry, scanning electron microscopy, transmission electron microscopy, and high

resolution transmission electron microscopy. Membrane/electrode assembly samples were sent to Oak Ridge National Laboratory for additional tests.

Figure 2.4.1 shows cell voltage and high frequency resistance transients for a test that includes a temporary acetonitrile contamination period of ~1000 h and a baseline test. It is noted that the Gore catalyst coated membranes are not stable with a significant degradation rate. This earlier design was not as stable as later ones. Furthermore, the high frequency resistance increases during the contamination period (figure 2.4.1, left), an observation that is consistent with impedance spectroscopy data (figure 2.3.1) and the proposed contamination mechanism (tables 2.3.2 and 2.3.3).

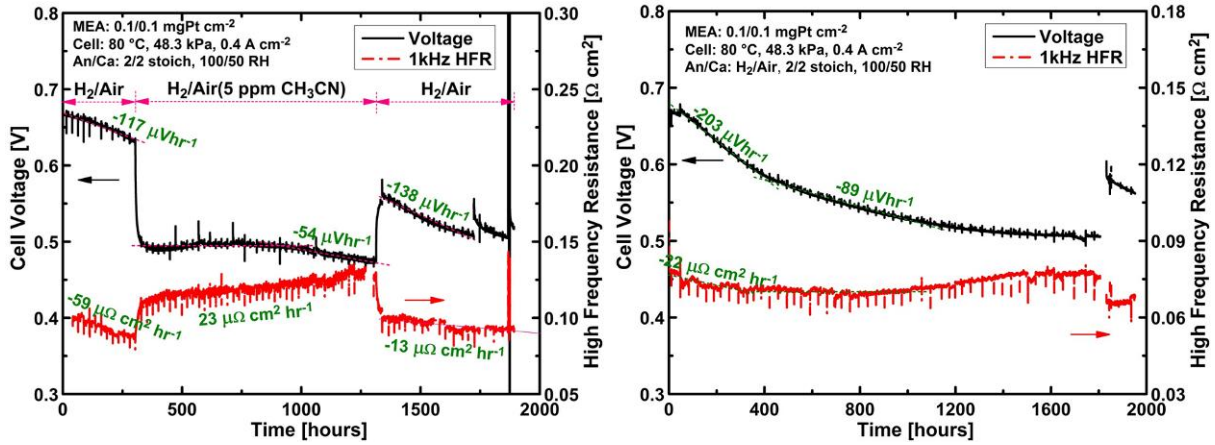

Figure 2.4.1. Long duration contamination test cell voltage and high frequency resistance transients. Acetonitrile (left), Baseline (right).

Figure 2.4.2, left illustrates the ion chromatography results of outlet water samples collected during the 1000 h exposure to 5 ppm acetonitrile. The presence of acetonitrile decreases the fluoride concentration in water samples. In particular, it is noted that after the contaminant is introduced, the fluoride concentration decreases whereas after the contaminant injection is interrupted, the fluoride concentration increases. The average fluoride concentration in the cathode outlet water is respectively 0.15 and 0.05 mg L^{-1} during the recovery and contamination period corresponding to a 67 % decrease during the contamination period. The F^- concentration in outlet water samples is relatively constant for the blank case in comparison to the contamination case (figure 2.4.2, right). It is hypothesized that acetonitrile acts as a scavenger for the radicals and/or peroxide generated at the cathode. The present results contrast with iron [15] and sulfur dioxide [16] data which demonstrated an increase rather than a decrease in fluoride concentration. Therefore, the scavenging effect is contaminant specific and needs to be ascertained for each contaminant. Membrane resistances (figure 2.4.1, left) and membrane thicknesses (figure 2.4.3) after the recovery period were not affected by the long term exposure to acetonitrile and support the acetonitrile as scavenger hypothesis. However, catalyst layers were thinned but not as extensively in the presence of CH_3CN. Scanning electron microscopy micrographs for the blank test show thinning of electrode layers (19 % reduction for the cathode, figure 2.4.3, bottom, left). In comparison, micrographs for the acetonitrile contaminated case also show thinning but to a smaller extent (9 % reduction for the cathode, figure 2.4.3, bottom, right).

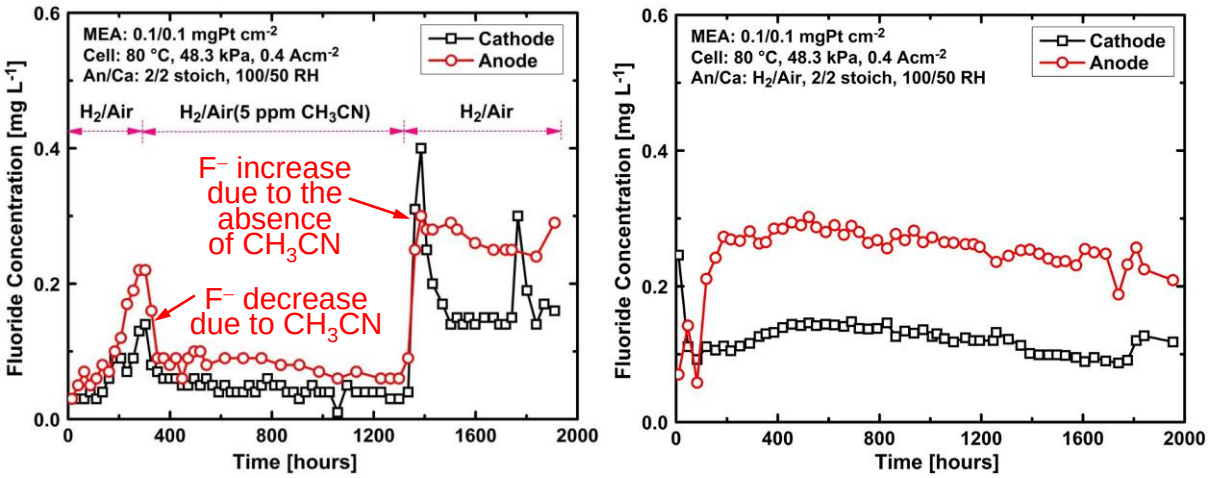

Figure 2.4.2. Fluoride concentration in liquid water samples extracted from fuel cell cathode and anode outlet streams as a function of time before, during and after an exposure to 5 ppm acetonitrile in air (left). Baseline data (right).

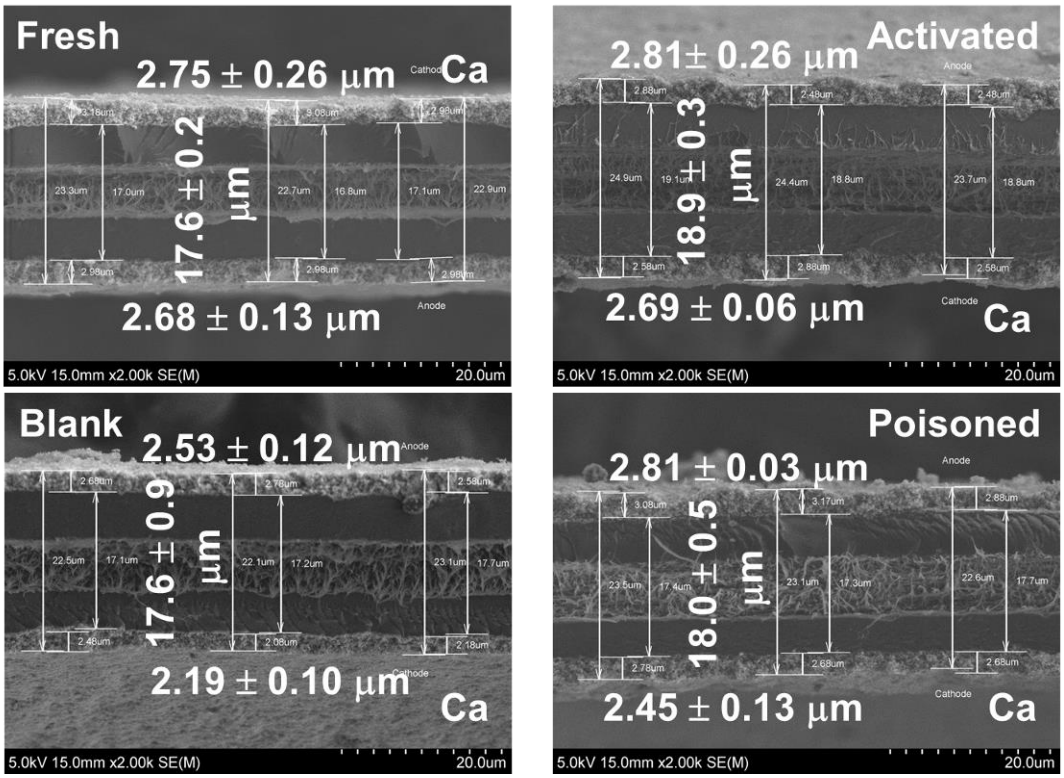

Figure 2.4.3. Scanning electron microscopy micrographs of membrane/electrode assembly (MEA) cross sections. Fresh MEA (top left), activated (conditioned) MEA (top right), baseline MEA (bottom left) and contaminated MEA (bottom right). 7 to 10 samples, 3 measurements at different locations for each sample.

In section 2.3, it was mentioned that acetonitrile undergoes a hydrolysis reaction in a fuel cell leading to ammonium ions (figure 2.3.27). Ammonium ions were also detected (near the detection limit) during the long term test (figure 2.4.4). The accumulation of ammonium cations is reversible as the concentration returns to its initial value after the contamination period.

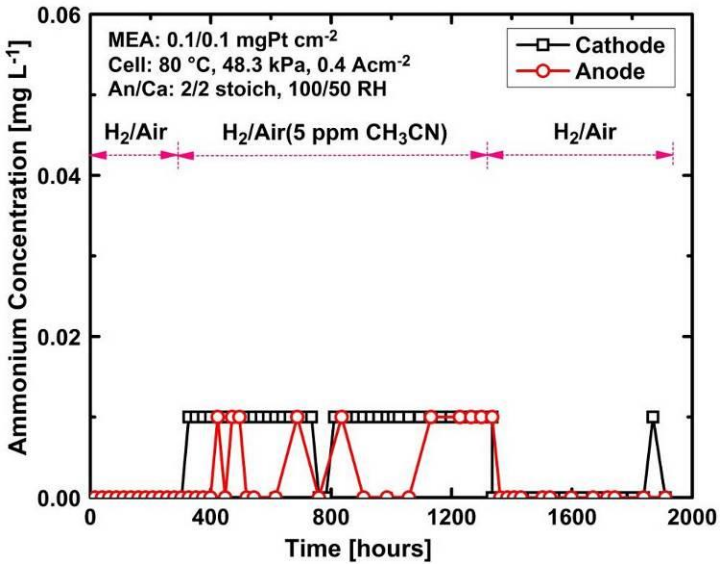

Figure 2.4.4. Ammonium concentration in outlet water samples collected during a long term fuel cell contamination test with acetonitrile.

Impedance spectroscopy data show that the membrane and ionomer have not significantly degraded after the recovery period (figure 2.4.5) confirming results from figures 2.4.1 and 2.4.3. The high frequency resistance returns to its original value after the recovery period for the contamination case (figure 2.4.5, left). In contrast, the baseline cell high frequency resistance is not affected. The catalyst layers thickness change (figure 2.4.3) is a negligible contribution to the total resistance, therefore, it is not noticeable. However, for a longer acetonitrile exposure test, the degradation may become more severe. All physical (scanning electron microscopy, figure 2.4.3) and electrochemical (high frequency resistance, figure 2.4.1, impedance spectroscopy, figure 2.4.5, oxygen polarization curves, figure 2.4.9) measurements support the insignificant resistance change observation (table 2.4.1).

Impedance spectra also show that contamination temporarily affects catalyst processes (figure 2.4.5). In the 10 Hz to 1 kHz range, the oxygen reduction kinetic resistance increases (increase in loop size) but the change is reversed after recovery. Below 10 Hz, the oxygen mass transfer resistance increases and/or an acetonitrile related reaction appears. The increase in mass transport resistance due to contaminant adsorbates on Pt decreasing its active area was already mentioned in relation to figure 2.3.3. For the overlapping presence of an acetonitrile related reaction, the similar propene case was discussed in relation to figure 2.3.4.

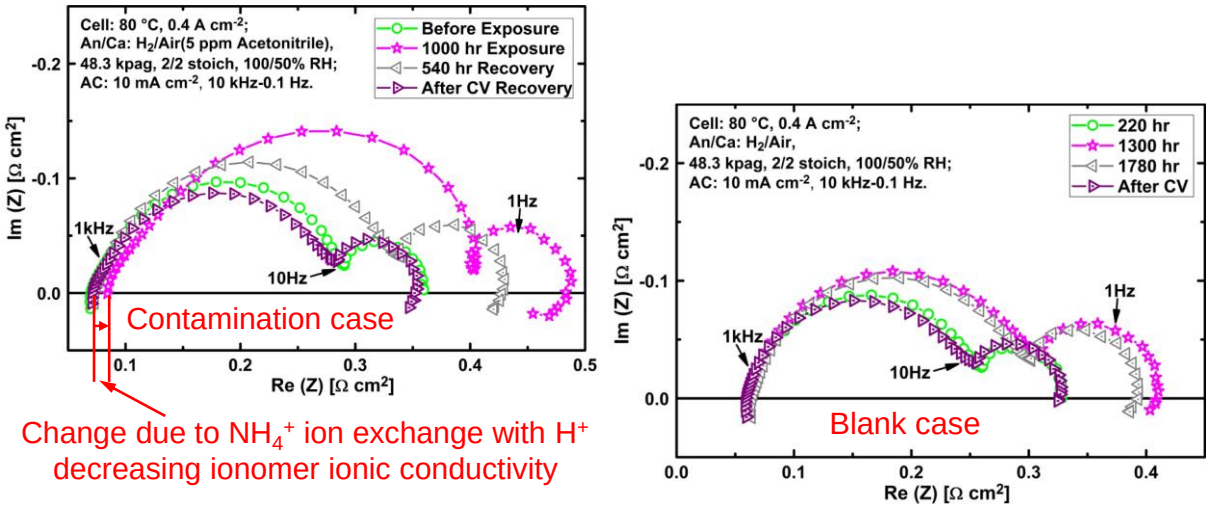

Figure 2.4.5. Impedance spectra obtained during the long duration acetonitrile contamination test (left) and for the baseline test (right).

Table 2.4.1. Summary of the resistance changes measured by different methods resulting from the long term tests with and without acetonitrile exposure.

Case		Resistance change (%) and measurement method			
		SEM[1]	HFR	IS	IV[2]
Contamination	Irreversible degradation	–1	~0	~0	~0
	Reversible degradation	-	44	17	-
Blank		–2	~0	~0	~0

[1] Cathode catalyst layer thickness change divided by the activated CCM thickness.
[2] Using O_2 polarization curves.

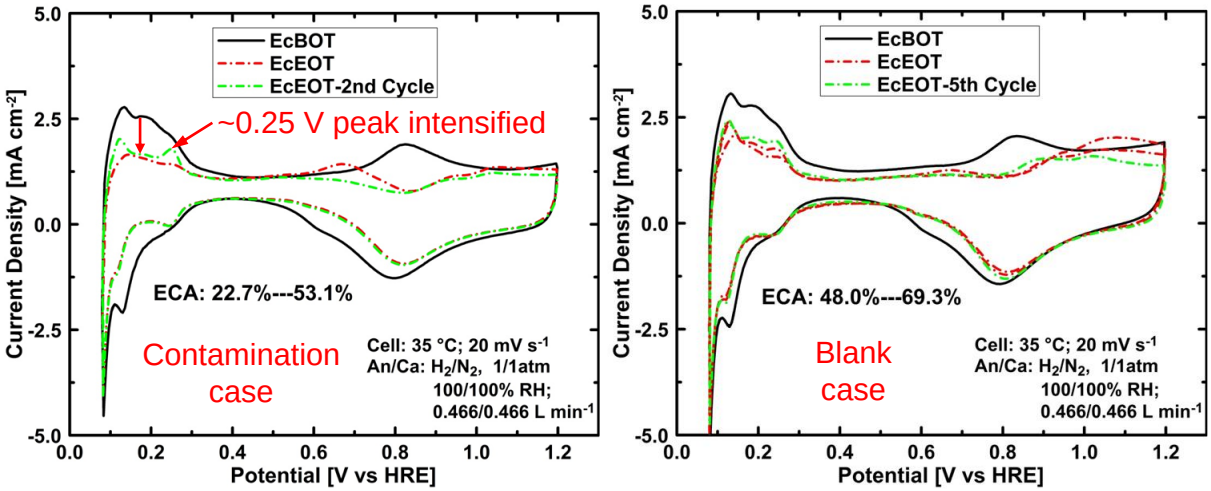

Figure 2.4.6. Cyclic voltammograms obtained before and after the long duration acetonitrile contamination test (left) and for the baseline test (right).

Figure 2.4.6 cyclic voltammograms indicate that the cathode catalyst active area is relatively smaller after recovery (decrease in positive hydrogen oxidation current in the 0.1-0.4 V vs HRE range). The catalyst active area decreases by 47 % with acetonitrile exposure but only 31 % in its absence. The change is partly ascribed to ionomer loss on the basis of scanning electron microscopy data (figure 2.4.3). However, the Pt crystal face distribution also appears to be modified because the 0.25 V vs HRE peak is relatively more intense after acetonitrile exposure than for the baseline case. Cyclic voltammogram findings contrast with the approximately constant kinetic resistance before contaminant exposure and after recovery (figure 2.4.5). The apparent inconsistency may be resolved by a concurrent increase in catalyst utilization, the appearance or intensification of a more active Pt site for the oxygen reduction or other causes.

Transmission electron microscopy data show a larger Pt nano-particle growth at the cathode exposed to acetonitrile (figure 2.4.7). This result is consistent with the decrease in Pt surface area measured by cyclic voltammetry (figure 2.4.6). The estimated maximum cathode potential during the test (~0.7 V vs HRE) is too low to induce Pt corrosion. Therefore, the Pt nano-particle growth mechanism is likely associated with particle migration on the support surface (acetonitrile adsorption modifies carbon surface properties?). The effect of acetonitrile on the anode is presently not as clear.

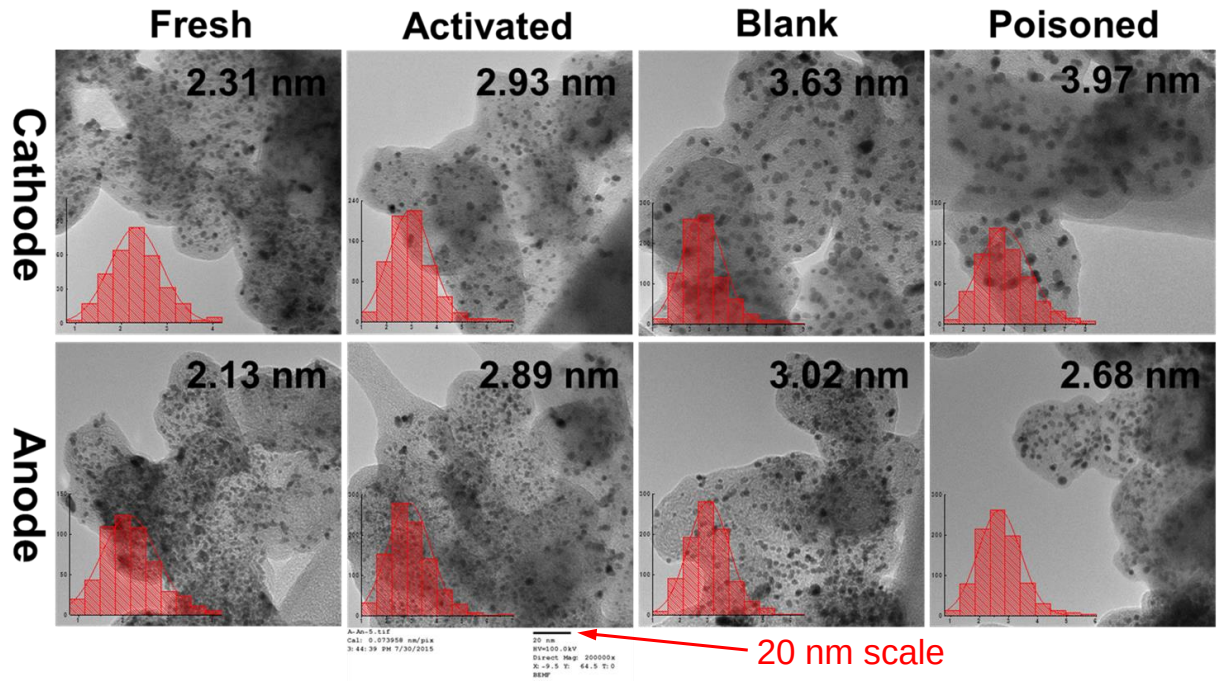

Figure 2.4.7. High resolution transmission electron microscopy pictures of cathode and anode catalysts after different operation condition sets.

Analysis of fuel cell outlet water samples by inductively coupled plasma mass spectrometry showed very low Pt concentrations of less than 0.5 part per trillion (figure 2.4.8). However, as stated in the previous paragraph, Pt is not expected to dissolve below 0.7 V vs RHE. Therefore, the observed trends are not yet explained. It is noted that experimental variability was improved by pre-concentrating samples (relatively small error bars in figure 2.4.8).

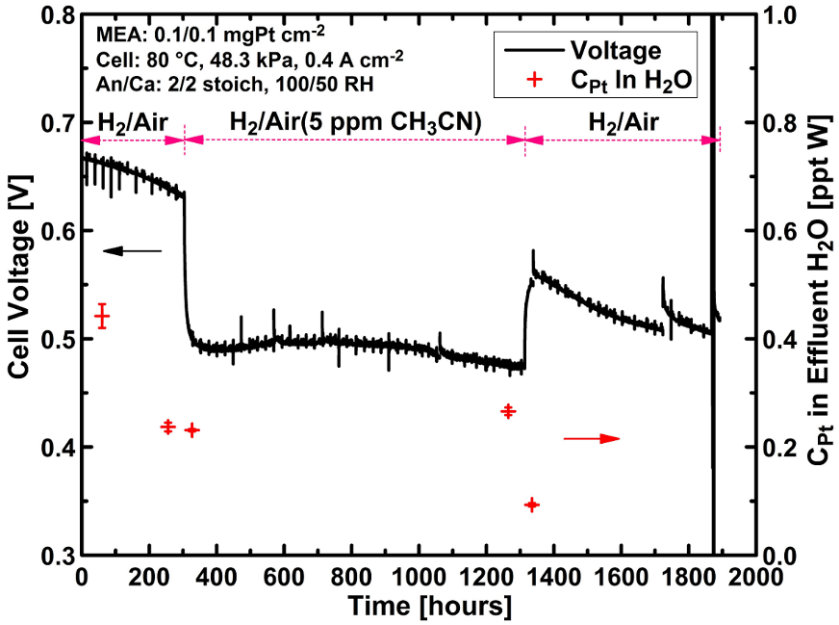

Figure 2.4.8. Pt concentration in the fuel cell outlet water samples. The cell voltage transient is also displayed to indicate sampling times.

Polarization curves (figure 2.4.9) support the hypothesis of a catalyst structural change (decrease in Pt active area, larger Pt nano-particles) with a translation to lower cell voltage values in the low current density (kinetic) region. The polarization curve translation is not as important for the baseline case, which is consistent with a smaller decrease in Pt active area and increase in Pt particle size. The small increase in the ohmic resistance derived from air polarization curves is assigned to carbon surface group formation improving water management (such a pseudo-ohmic mass transfer contribution was discussed [17]). Associated Tafel plots (figure 2.4.10) are not conclusive because most data points after recovery and cyclic voltammetry are located in the region associated with a doubling of the Tafel slope (below 0.8 V). For the air polarization data, the cell voltage loss is respectively 150 and 100 mV at 0.4 A cm^{-2} for the contamination and blank cases. These values are consistent with those derived from the cell voltage transients (figure 2.4.1). However, the full recovery of the impedance spectra after both tests (figure 2.4.5, right) still remains to be reconciled with cell voltage transients (figure 2.4.1) and polarization data (figure 2.4.9).

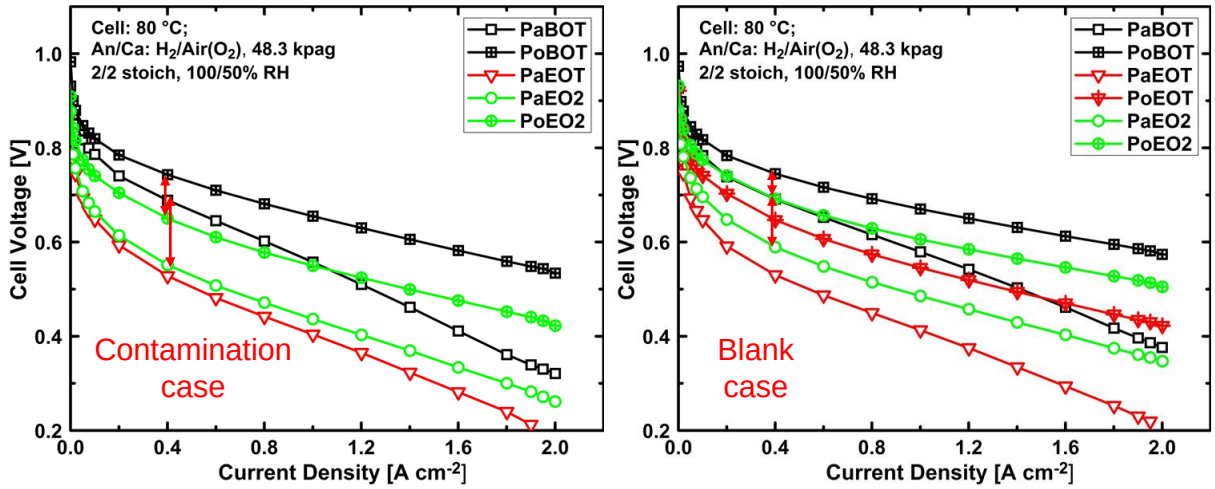

Figure 2.4.9. Polarization curves obtained at the beginning and end of the long duration acetonitrile contamination test (left) and baseline test (right). Polarization curves with air are denoted PaBOT (beginning of test) or PaEOT (end of test) or PaEO2 (repeat polarization at end of test). Polarization curves with O_2 are denoted PoBOT (beginning of test) or PoEO2 (repeat polarization at end of test).

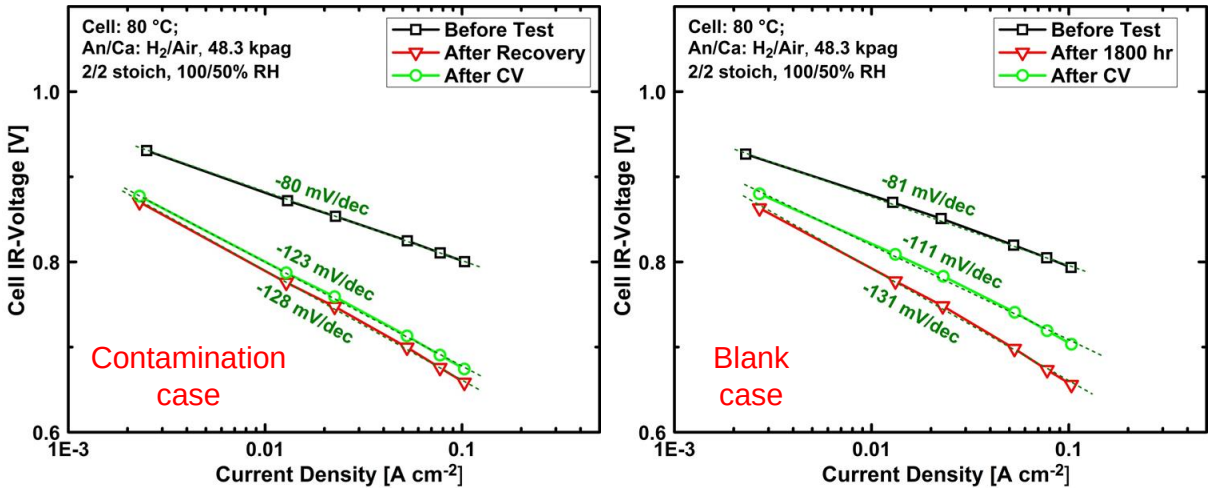

Figure 2.4.10. Tafel plots derived from polarization curves (figure 2.4.9) obtained at the beginning and end of the long duration acetonitrile contamination test (left) and baseline test (right).

Table 2.4.2 summarizes the oxygen reduction kinetic parameters derived from physical and electrochemical methods during long term tests with and without acetonitrile exposure. The effect of acetonitrile on Pt nano-particle aging is clear. However, characterization methods yielded results that are not yet consistent with impedance spectroscopy data.

The long term tests with and without acetonitrile yielded the following key conclusions. An exposure to 5 ppm acetonitrile significantly decreased fuel cell performance especially for a low 0.1 mg Pt cm^{-2} catalyst loading. Paradoxically, acetonitrile also acts as an imperfect scavenger for hydrogen peroxide and radical species because ionomer degradation still took place. These results contrast with fuel cells contaminated with SO_2 and Fe that have shown elevated F^- levels

in outlet water samples [15,16]. Acetonitrile contamination creates additional irreversible changes to the Pt catalyst nano-particles. Conflicting impedance spectroscopy observations need to be reconciled into a cohesive degradation mechanism.

Table 2.4.2. Summary of oxygen reduction kinetic parameters derived from the different characterization methods during long term tests with and without acetonitrile exposure.

Case	Parameter change or parameter and measurement method							
	TEM				CV	IS	IV	
	Particle diameter increase (%)[1]	Surface area decrease (%)[2]	ORR kinetic performance loss increase (mV)[3]	ORR kinetic resistance change (Ω cm^2)[4]	Catalyst surface area decrease (%)	ORR kinetic resistance change (Ω cm^2)	Cell voltage loss at 0.4 A cm^{-2} with O_2/air (mV)	Tafel slope before the test and after CV (mV/decade)
Contamination	35	24	17	0.11	47	~0	100/150	–80/–123
Blank	24	19	12	0.08	31	~0	50/100	–81/–111

[1] Cathode catalyst particle diameter change in comparison to its value after activation divided by the cathode catalyst particle diameter after activation.

[2] The change in surface area for a constant catalyst loading and spherical particles is $(1/D–1/D')/(1/D)$.

[3] For a cathode kinetic loss of the form $V=b\ln i$ (Tafel behavior), the change in kinetic loss is $(b'–b)\log i$.

[4] For a cathode kinetic loss of the form $V=b\ln i$ (Tafel behavior), the kinetic resistance is $dV/di=R=b/i$. The change in cathode resistance is the difference between the after CV and before test values $(b'–b)/i$.

2.4.2 *Long duration Ca^{2+} exposure*

The Ca^{2+} test was operated for ~450 h (figure 2.4.11, left) and the performance is compared to a baseline test with only de-ionized water injection. During the contaminant test, the $CaSO_4$ solution was injected at the cathode inlet using a nebulizer (figure 2.1.5). During the $CaSO_4$ solution injection (corresponding to 5 ppm in dry air), the cell voltage starts to fall rapidly. The pressure drop was monitored between the cathode inlet and outlet (Figure 2.4.11, right). The increased pressure drop over time is due to salt precipitation in the cathode gas diffusion layer and flow field channels. Moreover, the pressure gain trend coincides with the voltage loss. The cell test was stopped after 350 h of $CaSO_4$ injection due to a flow obstruction by precipitates located at the cathode outlet (figure 2.4.12, right). The voltage spikes for both $CaSO_4$ and baseline tests in figure 2.4.11 are due to impedance measurements. The cell voltage noise observed between 320 to 370 h for the $CaSO_4$ test is an artifact of the test system, which was subsequently fixed.

Figure 2.4.12 shows the salt deposits on the gas diffusion layer and the cathode flow field. These deposits lead to a severe mass transfer limitation. Polarization curves demonstrate this large mass transfer loss (figure 2.4.13, left) by a large decrease in limiting current density. The polarization curve was obtained with less than the target oxygen stoichiometry owing to the salt blockage. Once the oxygen is depleted, the cell performance is even lower than depicted for the end of test. Impedance spectra obtained before and during the long duration test not only show a large increase in mass transport resistance (right loop) but also showed a significant increase in oxygen reduction (left loop) resistance (figure 2.4.13, right). The oxygen reduction resistance increase conflicts with overlapping polarization curves at low current densities in the kinetic regime (figure 2.4.13, left). A similar observation was reported in section 2.4.1 for acetonitrile. Impedance spectra also indicate that the high frequency resistance has not significantly changed (spectra intercepts of ~0.003 ohm for low real resistance values).

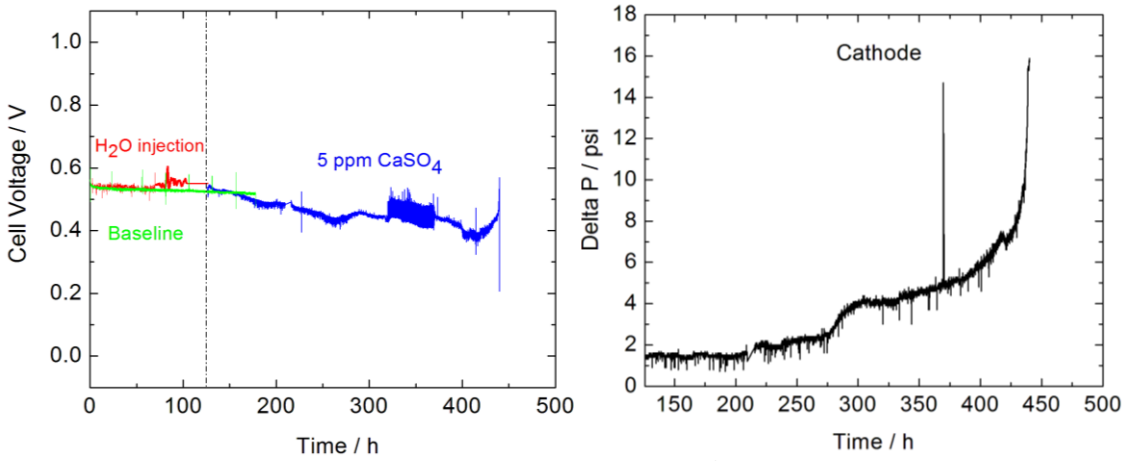

Figure 2.4.11. Long duration contamination test with Ca^{2+}. Cell voltage transient (left) and cathode pressure drop transient (right). Reprinted and reformatted with permission from *ECS Trans.*, **66** (24), 19 (2015). Copyright 2015, The Electrochemical Society.

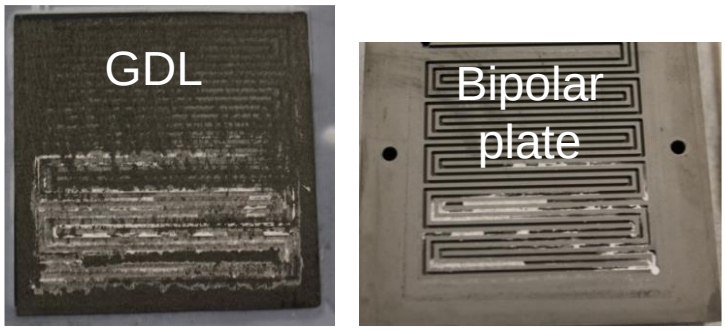

Figure 2.4.12. Calcium salt deposits responsible for the long duration test interruption. Cathode flow field channel side of the gas diffusion layer (left) and cathode flow field side of the bipolar plate (right). Reprinted and reformatted with permission from *ECS Trans.*, **66** (24), 19 (2015). Copyright 2015, The Electrochemical Society.

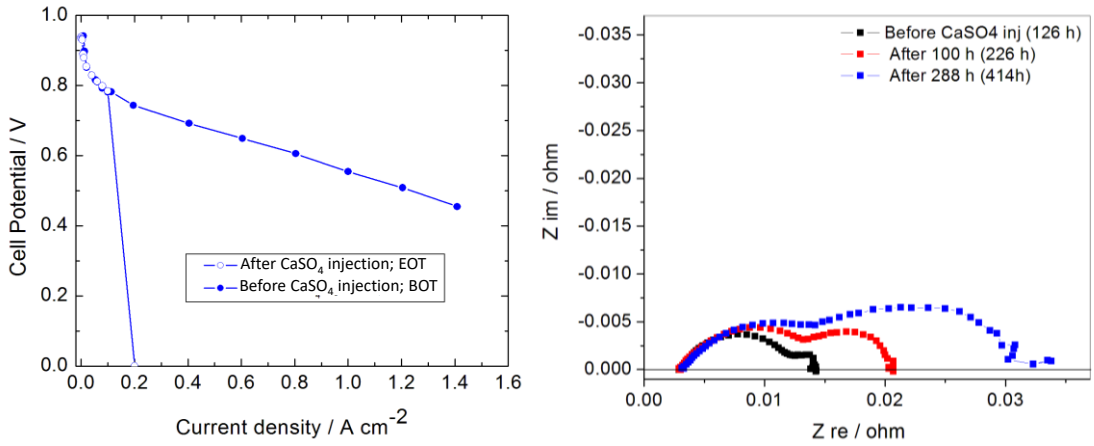

Figure 2.4.13. Polarization curves obtained before and after the test with Ca^{2+} (left). Impedance spectra obtained before and during the test with Ca^{2+} (right). The right figure is reprinted and reformatted with permission from *ECS Trans.*, **66** (24), 19 (2015). Copyright 2015, The Electrochemical Society.

The impact of Ca^{2+} on metal corrosion was assessed by measuring the presence of cations in outlet water samples collected during the long term test with inductively coupled plasma mass spectroscopy. Materials exposed to Ca^{2+} include stainless steel tube fittings, aluminum end plate, gold coated copper bus plate and platinum catalyst. Figure 2.4.14 indicates that Ca^{2+} promoted stainless steel corrosion with an increase in iron, chromium and nickel concentrations. Gold was below the detection limit and copper was not affected by Ca^{2+}. Aluminum was also observed below the detection limit. As aluminum is prone to corrosion in contact with an aqueous solution, the end plate inlet and outlet ports were lined with Teflon. Hence, aluminum was not affected by Ca^{2+}. The amount of Pt leached at the cathodes was almost the same for both baseline and $CaSO_4$ injection cases. The results indicate the Ca^{2+} does not significantly influence the Pt oxidation reaction because the cathode potential is lower than 0.7 V vs HRE (section 2.4.1).

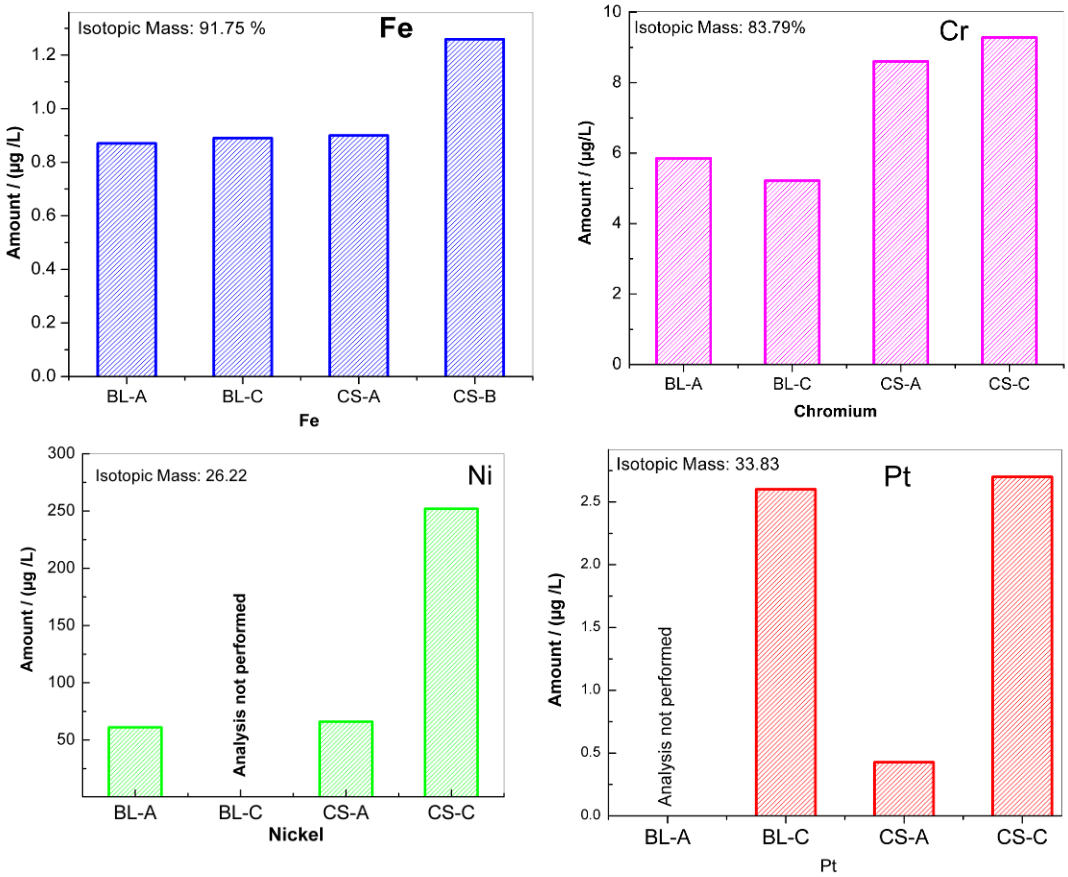

Figure 2.4.14. Selected metal concentrations in outlet water samples collected during a long term fuel cell contamination test with Ca^{2+} (BL-A: anode baseline, BL-C: cathode baseline, CS-A: anode sample for calcium sulfate injected in the cathode case, CS-C: cathode sample for calcium sulfate injected in the cathode case). The bottom, right figure is reprinted and reformatted with permission from *ECS Trans.*, **66** (24), 19 (2015). Copyright 2015, The Electrochemical Society.

Evidence of carbon corrosion was noticed (figure 2.4.15). Membrane/electrode assembly cross sections and Pt concentration maps obtained by scanning electron microscopy and energy dispersive X-ray spectroscopy revealed a thinner cathode catalyst layer. A greater rate of platinum dissolution was discounted because it was not supported by outlet water sample analyses (figure 2.4.14). Furthermore, the Pt concentration at the cathode appears to be higher

after the long duration test suggesting that the Pt was not affected but is effectively concentrated in a smaller volume (figure 2.4.15, bottom). These observations suggest that the increase in hydrogen peroxide due to the presence of Ca^{2+} is not as large as for acetonitrile even if scavenging is taking place (section 2.4.1) leading to a less intense ionomer degradation. This statement is also consistent with table 2.3.2 rotating ring/disc electrode results for iso-propanol and Ca^{2+}.

An earlier test did not show clear evidence of carbon corrosion (micrographs not shown, cell B in section 3.1, reference J4). It is possible that the effect was masked because the cathode catalyst loading was higher at 0.4 rather than 0.1 mg Pt cm^{-2} and the cell was run for a shorter period of time of 70 rather than ~450 h. The carbon corrosion mechanism in the presence Ca^{2+} is currently unknown (no related report was found).

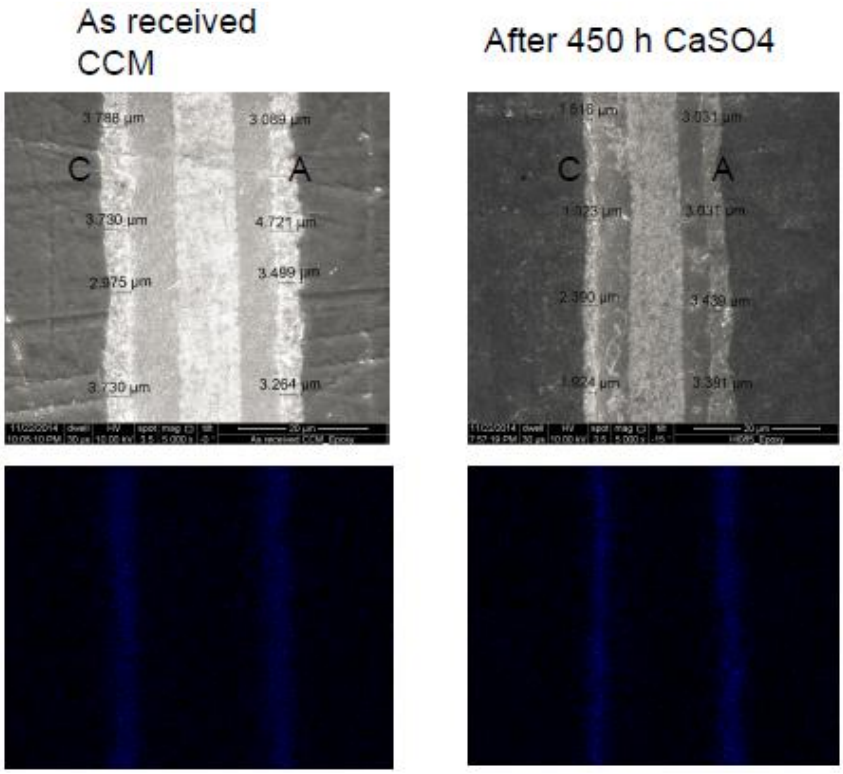

Figure 2.4.15. Membrane/electrode assembly cross sections imaged by scanning electron microscopy (top) and corresponding energy dispersive X-ray spectroscopy Pt maps (bottom) before and after the long duration fuel cell test with Ca^{2+} (for each image, the cathode is on the left). The right figures are reprinted and reformatted with permission from *ECS Trans.*, **66** (24), 19 (2015). Copyright 2015, The Electrochemical Society.

Additional tests were completed to confirm the presence of carbon corrosion during Ca^{2+} contamination. Figure 2.4.16 shows the potentiostatic test performance results in the presence of Ca^{2+}. A potentiostatic test was preferred as carbon corrosion is potential dependent. The cell voltage oscillations appearing at ~125 h are due to the load bank operating near its lower power limit.

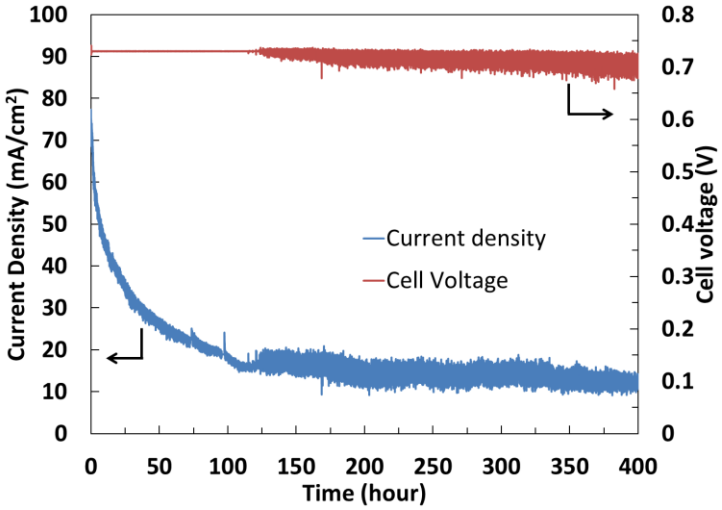

Figure 2.4.16. Cell voltage and current density during a long duration fuel cell contamination test with Ca^{2+}. Reprinted and reformatted with permission from *ECS Trans.*, **66** (24), 29 (2015). Copyright 2015, The Electrochemical Society.

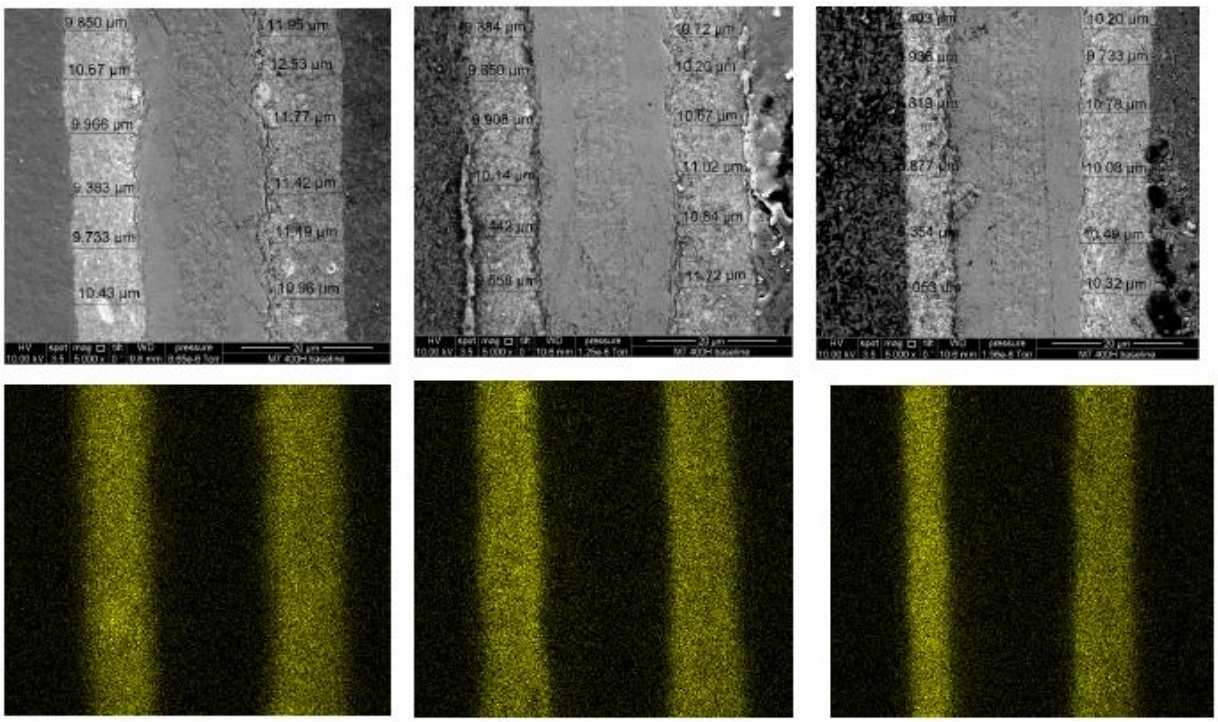

Figure 2.4.17. Membrane/electrode assembly cross sections imaged by scanning electron microscopy (top) and corresponding energy dispersive X-ray spectroscopy maps (bottom) after a long duration fuel cell baseline test (for each image, the cathode is on the left). At the inlet (left) and at the outlet (center and right). The left and right figures are reprinted and reformatted with permission from *ECS Trans.*, **66** (24), 29 (2015). Copyright 2015, The Electrochemical Society.

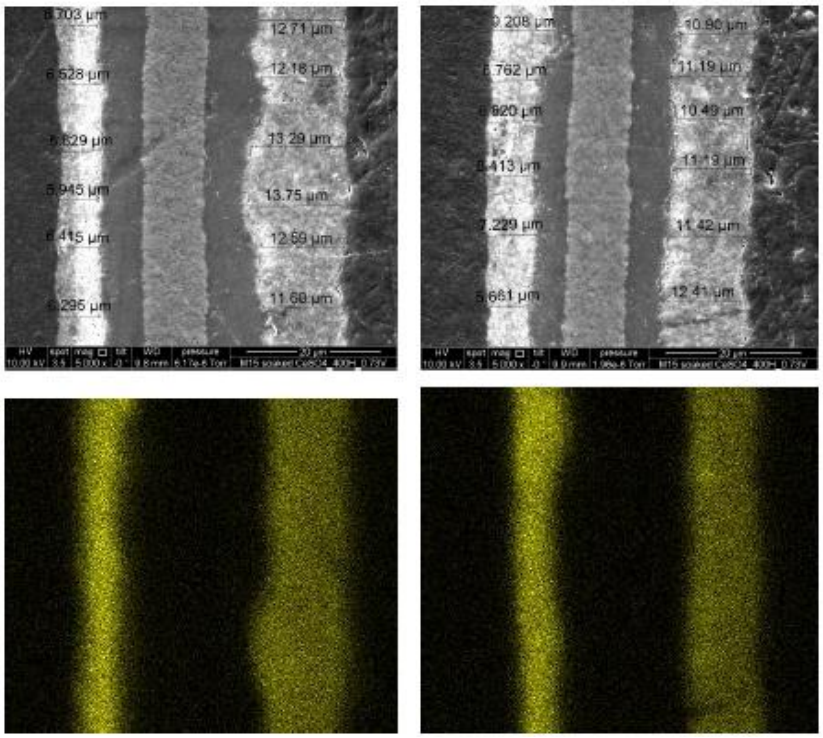

Figure 2.4.18. Membrane/electrode assembly cross sections imaged by scanning electron microscopy (top) and corresponding energy dispersive X-ray spectroscopy Pt maps (bottom) after a long duration fuel cell test with Ca^{2+} (for each image, the cathode is on the left). At the inlet (left) and at the outlet (right). The right figures are reprinted and reformatted with permission from *ECS Trans.*, **66** (24), 29 (2015). Copyright 2015, The Electrochemical Society.

Figures 2.4.17 and 2.4.18 illustrate the membrane/electrode assembly cross sections (scanning electron microscopy) and corresponding Pt maps (energy dispersive X-ray spectroscopy) for baseline and Ca^{2+} contamination tests. Table 2.4.3 summarizes the catalyst layer thicknesses derived from these figures. It is noted that the cathode catalyst layer is indeed thinner at the cell inlet and outlet. Interestingly, the baseline test also showed a locally thinner cathode catalyst layer at the cell outlet. For each test, the anode catalyst layer is unaffected. The cathode catalyst layer thinning is consistent for both membrane/electrode assemblies soaked with Ca^{2+} and cells with Ca^{2+} injected during operation. These results indicate that the Ca^{2+} ion either directly or indirectly promotes the carbon oxidation reaction or catalyst layer thinning process at the cathode. The development of a detailed mechanism is an outstanding activity that could rely on a specific test to discriminate between carbon corrosion and ionomer degradation (for example, the air outlet carbon dioxide concentration could be linked to carbon corrosion).

In retrospect, the long duration Ca^{2+} exposure test highlighted exacerbated corrosion of stainless steel and carbon. In contrast, ionomer degradation by increased levels of hydrogen peroxide does not appear to have a significant impact during the ~300 h exposure. Similarly to acetonitrile contamination (section 2.4.1), conflicting impedance spectroscopy observations need to be reconciled into a cohesive degradation mechanism.

Table 2.4.3. Average cathode and anode catalyst layer thickness after baseline and Ca^{2+} contamination tests.

Test	Average cathode thickness (μm)		Average anode thickness (μm)	
	Cell inlet	Cell outlet	Cell inlet	Cell outlet
Baseline	10	9.7 and 6.9[a]	11.6	10.9 and 10.3[a]
Contaminated with Ca^{2+}	6.3	7	12.7	11.3

[a] For the baseline cell outlet case, 2 images were analyzed (figure 2.4.17, center and right).

2.4.3 *Acetonitrile, bromomethane and propene mixture*

The long term mixture test with 0.5 ppm acetonitrile, 1 ppm bromomethane, and 2 ppm propene was completed to assess the impact of lower contaminant concentrations closer to atmospheric values and synergy between contaminants. Acetonitrile was selected because it is the only 2nd tier organic contaminant that led to ohmic losses (figure 2.3.1). Bromomethane was selected because it is the only 2nd tier contaminant that led to irrecoverable losses (table 2.1.5). Propene, another 2nd tier contaminant, was also included because it leads to small gains in performance after recovery (table 2.1.5). The mixture was limited to 3 species to minimize injection logistics and facilitate data interpretation.

Figure 2.4.19 illustrates the transients in cell voltage and high frequency resistance resulting from the organic contaminant mixture. A significant degradation of approximately 200 mV was observed after an exposure of 100 h (a short and rapid initial drop of ~50 mV is observed and followed by a large and approximately constant voltage decay rate of ~1.5 mV h^{-1}). A steady state was not reached during that time period. The slight and reversible increase in high frequency resistance is tentatively ascribed to the presence of acetonitrile in the membrane (hydrolysis leads to ammonium ions, figure 2.3.27). In spite of a substantial decrease in concentration, the cell performance loss is still significant (most operating conditions tests were completed with 20, 5 and 100 ppm for respectively acetonitrile, bromomethane, and propene, table 2.2.1). It is also noted that the performance is only partially recovered after the contaminant mixture is no longer introduced into the cell (the steady state value is significantly lower than the original value by ~100 mV). This observation is tentatively ascribed to bromomethane, the only tested organic contaminant that led to irrecoverable losses.

Figure 2.4.20, left illustrates impedance spectra acquired at different stages during the organic contaminant mixture test. The medium frequency loop ascribed to the oxygen reduction reaction (~10-1000 Hz) and the low frequency loop ascribed to oxygen mass transfer in the absence of contamination (<10 Hz) increased in size as a result of contamination. The ohmic resistance (the high frequency intercept) also slightly increased. These observations are consistent with the recorded transients (figure 2.4.19). Impedance spectra were fitted to an equivalent circuit model (figure 2.3.1) to extract resistance values and these are plotted in figure 2.4.20, right. The key contributors to the performance loss are the oxygen reduction kinetic resistance and mass transfer resistance increases. These resistances do not return to their original values after the recovery period.

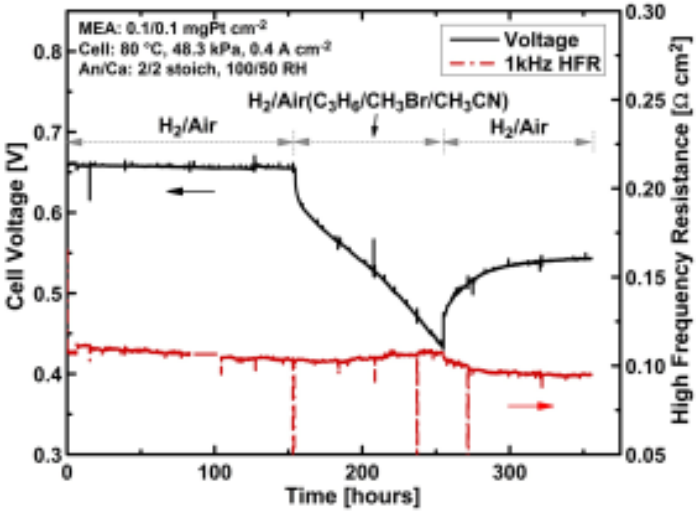

Figure 2.4.19. Cell voltage and high frequency resistance transients for a cell exposed to a temporary contaminant mixture of 0.5 ppm acetonitrile, 1 ppm bromomethane, and 2 ppm propene.

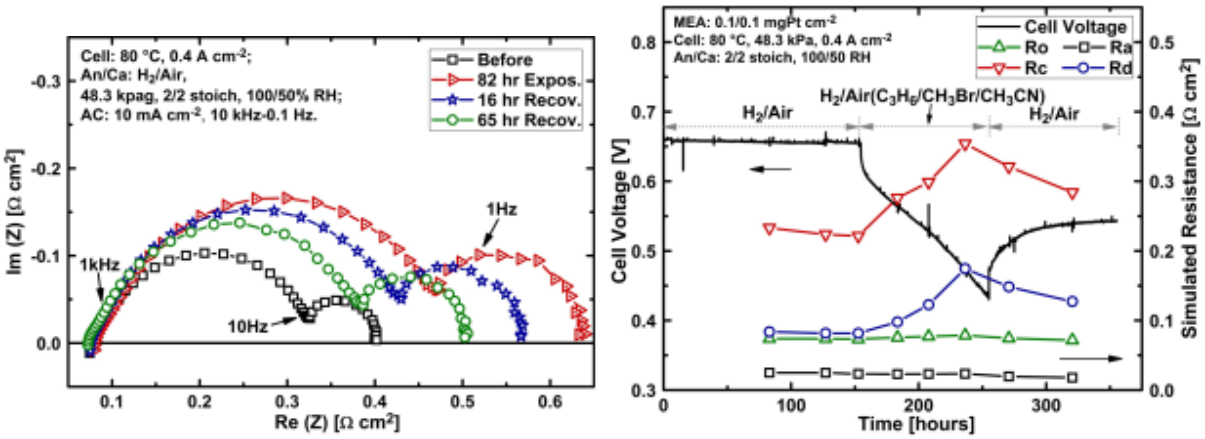

Figure 2.4.20. Impedance spectra obtained during the contamination mixture test (left). Hydrogen oxidation kinetic resistance Ra, oxygen reduction kinetic resistance Rc, ohmic resistance Ro and mass transfer resistance Rd obtained from an equivalent circuit model fit to the impedance spectra (right).

Figure 2.4.21, top, left depicts the cyclic voltammograms recorded after the recovery period and at the operating cell temperature. The presence of new peaks at approximately 0.6 and 0.9 V vs HRE during the anodic sweep suggests the presence of presently unidentified species on the catalyst surface which partly account for the smaller active Pt surface area. Potential cycling recovers a significant portion of the Pt active surface area up to 64 % of the original value. Additional cyclic voltammograms obtained at a lower temperature of 35 °C also indicate a significant loss in Pt active surface area at the cathode. The decrease at the anode is smaller and accounted for by other aging mechanisms.

Polarization curves illustrated in figure 2.4.22 are also consistent with other results. They indicate only a partial recovery and kinetic losses (curve translation to lower cell voltages at low current densities). The decrease in air polarization curve slope after the test (figure 2.4.22, left) is

assigned to mass transport because such a change is absent on oxygen polarization curves (figure 2.4.22, right). A similar change was noted for the long term acetonitrile contamination test (figure 2.4.9, left). The cell voltage could not be lowered further with air and, as a result, it is not possible (equipment limitations) to evaluate the changes in oxygen mass transport.

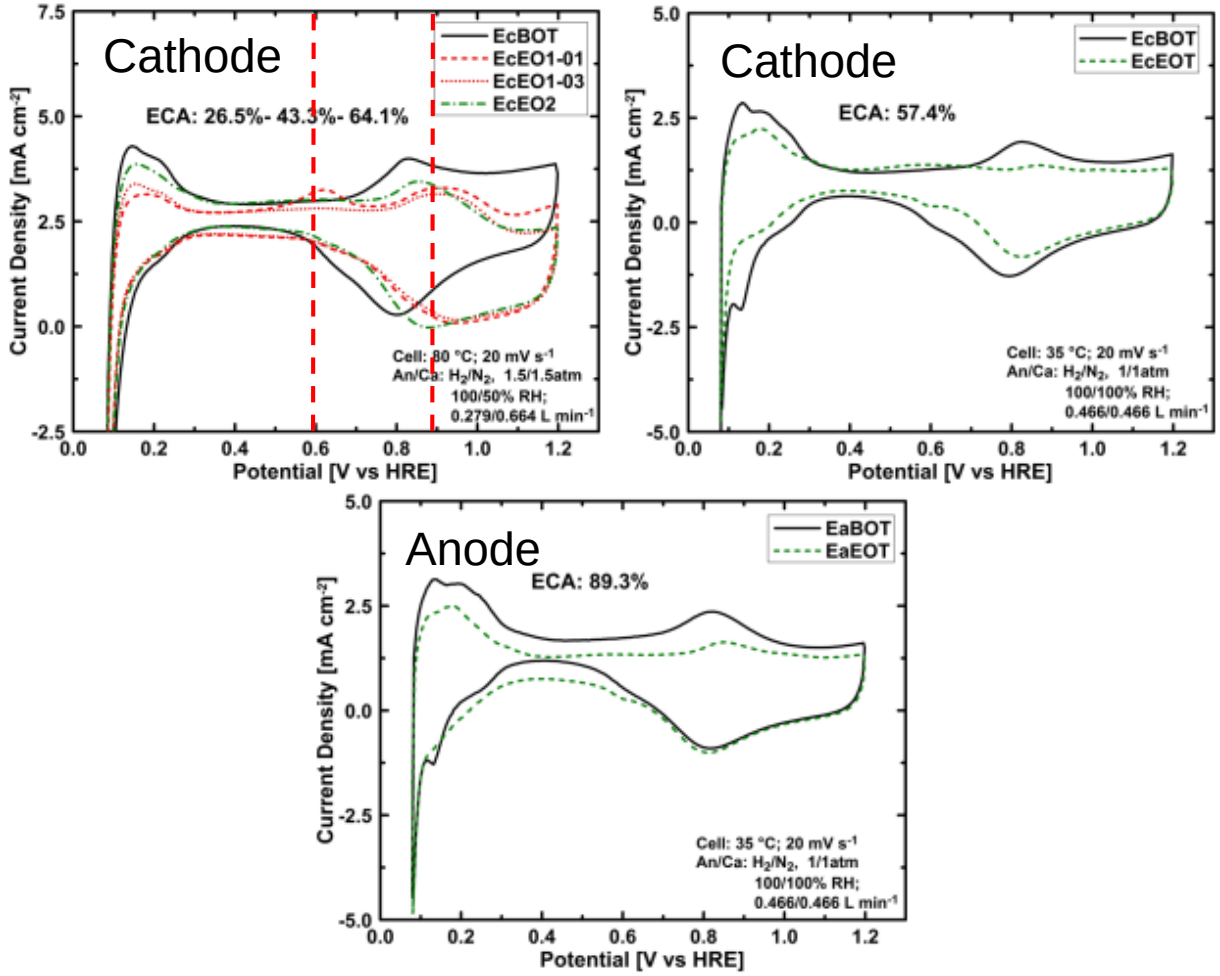

Figure 2.4.21. Cyclic voltammograms obtained before and after the organic contaminant mixture test at the operating cell temperature (top, left). Cyclic voltammograms obtained before and after the organic contaminant mixture test. Cathode (top, right) and anode (bottom). EC: cathode, EA: anode, BOT: beginning of test, EOT: end of test, EO1-01: first cycle after end of test, EO1-03: third cycle after end of test, EO2: repeat cyclic voltammogram after end of test.

Although signatures from the single contaminants are noted in figures 2.4.19 and 2.4.20 with the exception of propene, data are insufficient to evaluate the presence of interactions between the three mixture species. This situation is in part due to the dual decrease in catalyst loading and contaminant concentration. For a larger catalyst loading of 0.4 mg Pt cm^{-2}, the decrease in acetonitrile and propene concentration to respectively 0.5 and 2 ppm was not expected to modify the cell voltage because these values are below the 5 % voltage loss tolerance limit (table 1.2.1). However, the cell voltage loss due to bromomethane was expected to be still significant at 1 ppm as it is weakly dependent on concentration (a 49 % to 38 % loss in cell voltage for a decrease from 20 to 2 ppm, table 2.2.1). For the relatively large and fixed contaminant concentrations

employed for the determination of mechanisms, a decrease in Pt loading from 0.4 to 0.1 mg cm^{-2} promoted an increase in cell voltage loss of respectively 58, −10 (the negative value corresponds to an increase in cell voltage), and 224 % for acetonitrile, bromomethane, and propene (section 2.6.1). Data were not obtained for changes in both contaminant concentration and catalyst loading. Even if interactions between the three contaminants cannot be evaluated (unidentified cyclic voltammetry peaks may support their existence, figure 2.4.21), the dilute ternary contaminant mixture creates a large cell voltage loss for a commercially relevant catalyst loading. Additional work should be pursued in this area to revise and predict contaminant tolerance limits for mixtures and commercially relevant cathode catalyst loadings.

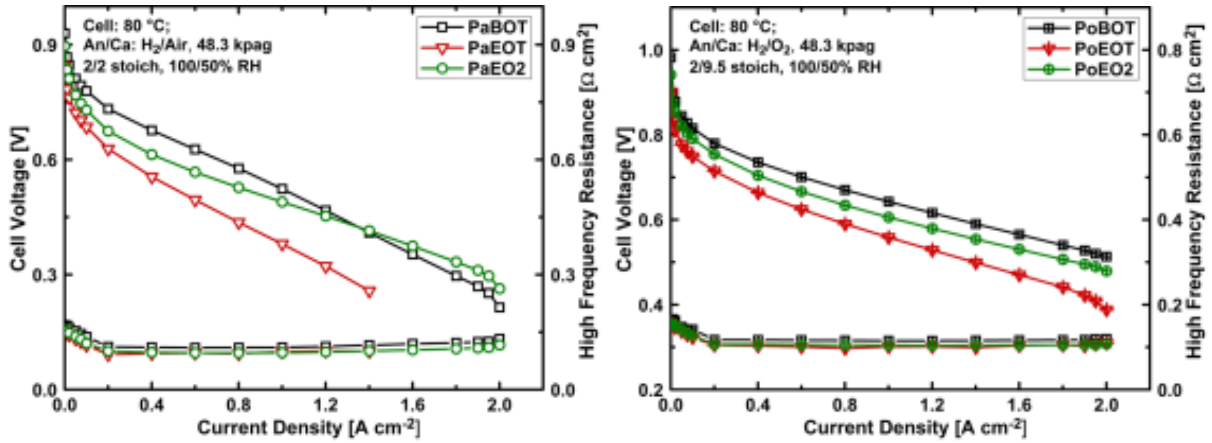

Figure 2.4.22. Polarization curves obtained at the beginning and end of the organic contaminant mixture test. Air (left) and oxygen (right) polarization curves. Polarization curves with air are denoted PaBOT (beginning of test) or PaEOT (end of test) or PaEO2 (repeat polarization at end of test). Polarization curves with O_2 are denoted PoBOT (beginning of test) or PoEOT (end of test) or PoEO2 (repeat polarization at end of test).

2.5 Mitigation strategies (milestone 4, task 2.2)

Only two 2nd tier contaminants led to an incomplete recovery after injection was interrupted (bromomethane, figure 2.2.5, Ca^{2+}, figure 2.2.6, top, left, figure 2.2.7, right). Recovery tests exclusively focused on these two species which also meant that milestone 4 was not completed as stated (demonstrate successful mitigation of the impact of the most important 4 airborne contaminants).

2.5.1 *Ca^{2+} (section 3.1, reference 22)*

Both *ex situ* and *in situ* contamination procedures were used to investigate the effectiveness of recovery methods, which mirror the two key impacts of cation contamination: salt precipitation and ion exchange with ionomer materials (table 2.3.3). The *ex situ* contamination methods (table 2.5.1, figure 2.5.1) all involve dipping the catalyst coated membrane into a solution. The catalyst coated membrane area directly exposed to the solution, the solution exposure duration and the solution composition were varied. Fuel cell operation with Ca^{2+} injection (figure 2.1.5) represents the *in situ* contamination procedure which leads to salt deposition. The Ca^{2+} injection

influences not only the membrane but also the gas diffusion electrode transport properties and water management by precipitation of hydrophilic salt.

Table 2.5.1. Summary of the methods used to contaminate catalyst coated membranes *ex situ* and membrane/electrode assemblies *in situ* with foreign cations.

Method	Method description	Soaking time	Wetting Agent
A	The CCM is in direct contact with the Ca^{2+} solution	24 h	-
B	Portion of the CCM is in direct contact with the Ca^{2+} solution	100 h	-
C	The CCM is not in direct contact with the solution being separated by both the GDL and a gasket	100 h	-
D	Method C with wetting agent	100 h	1 % IPA
E	Method C with wetting agent	100 h	15 % IPA

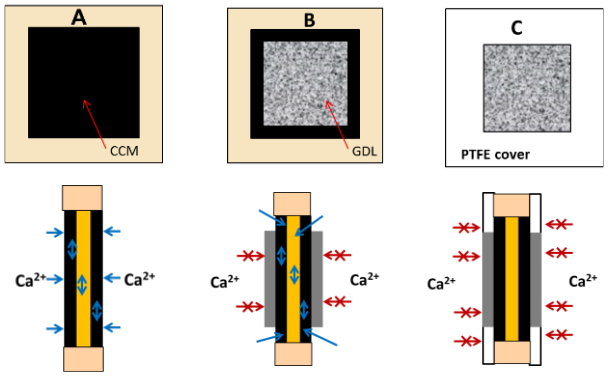

Figure 2.5.1. Membrane/electrode assembly contamination methods A (the catalyst coated membrane (CCM) is in direct contact with the Ca^{2+} solution), B (the Ca^{2+} solution is only in direct contact with the catalyst coated membrane at its periphery because the solution does not wet the gas diffusion layer) and C (the Ca^{2+} solution is not in direct contact with the catalyst coated membrane being separated by both the gas diffusion layer (GDL) and a gasket). Reprinted and reformatted with permission from *ECS Trans.*, **64** (3), 537 (2014). Copyright 2014, The Electrochemical Society.

Figure 2.5.2 illustrates that contamination methods A and B lead to a significant cell performance drop whereas method C has a marginal effect even if the soaking period is extended by a factor of 4 in comparison to method A (table 2.5.1). The marginal effect of contamination method C is attributed to the gas diffusion layer which acts as a barrier to the transport of Ca^{2+} ions. The contamination effect becomes less severe as the access to the ionomer and membrane is more constricted by the gas diffusion layer and gasket. Additional procedures were also investigated by modifying the solution composition for procedure C. Procedures D and E (table 2.5.1), which are the same as procedure C with the addition of a surfactant (respectively 1 and 15 % iso-propanol (IPA)), also demonstrate in figure 2.5.3 the important role of the gas diffusion layer (the wetter gas diffusion layer promotes the transport of Ca^{2+} to the ionomer). Iso-propanol was selected over methanol, ethanol, and Triton X because its contaminant effect is relatively

small and reversible (table 2.1.5, figure 2.2.8, bottom). The iso-propanol concentration was limited to 15 % because higher values also led to catalyst coated membrane damage.

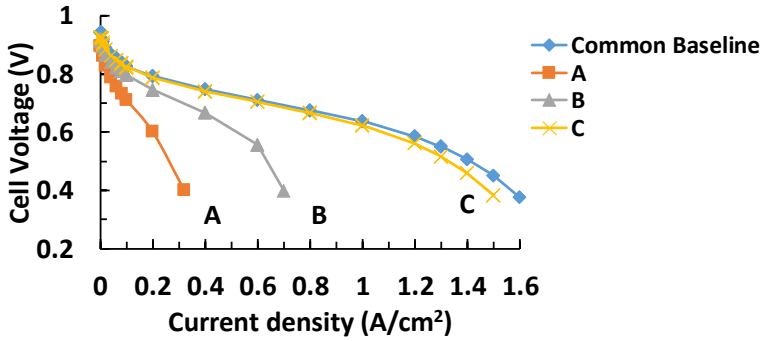

Figure 2.5.2. Comparison between a baseline polarization curve and others obtained after different Ca^{2+} exposure methods A to C (table 2.5.1). Reprinted and reformatted with permission from *ECS Trans.*, **64** (3), 537 (2014). Copyright 2014, The Electrochemical Society.

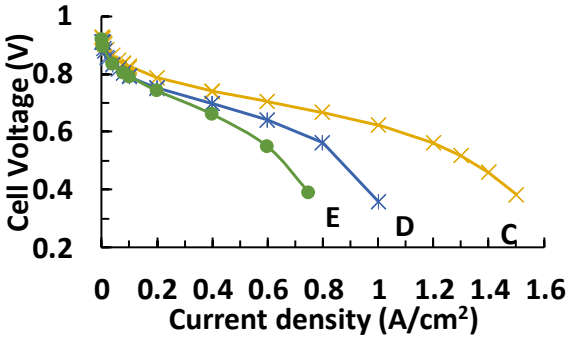

Figure 2.5.3. Comparison between a baseline polarization curve and others obtained after different Ca^{2+} exposure methods D and E (table 2.5.1). Reprinted and reformatted with permission from *ECS Trans.*, **64** (3), 537 (2014). Copyright 2014, The Electrochemical Society.

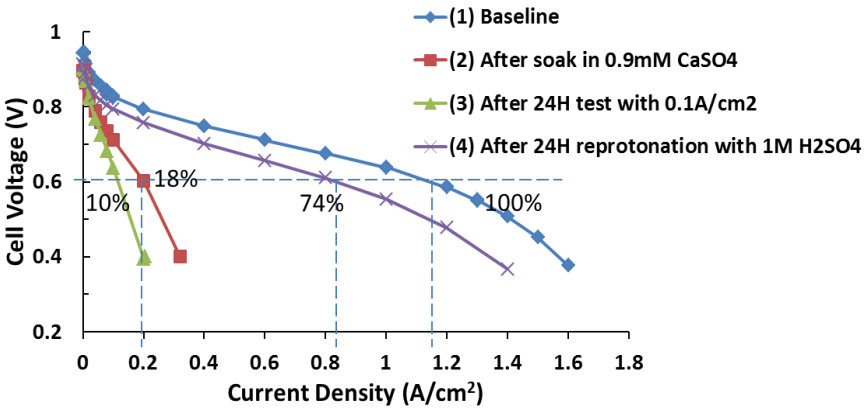

Figure 2.5.4. Comparison between a baseline polarization curve and others obtained after Ca^{2+} exposure method A (table 2.5.1) followed by recovery at a low current density and after a soak of the catalyst coated membrane in an acid solution. Reprinted and reformatted with permission from *ECS Trans.*, **64** (3), 537 (2014). Copyright 2014, The Electrochemical Society.

The effectiveness of an *ex situ* recovery with an acid solution soak of the catalyst coated membrane contaminated *ex situ* with the cell A configuration (table 2.5.1) was explored to help define the maximum recovery extent (the catalyst coated membrane is in direct contact with the solution favoring ion exchange). However, the test was only partly effective and only 74 % of the current density at 0.6 V was recovered (figure 2.5.4).

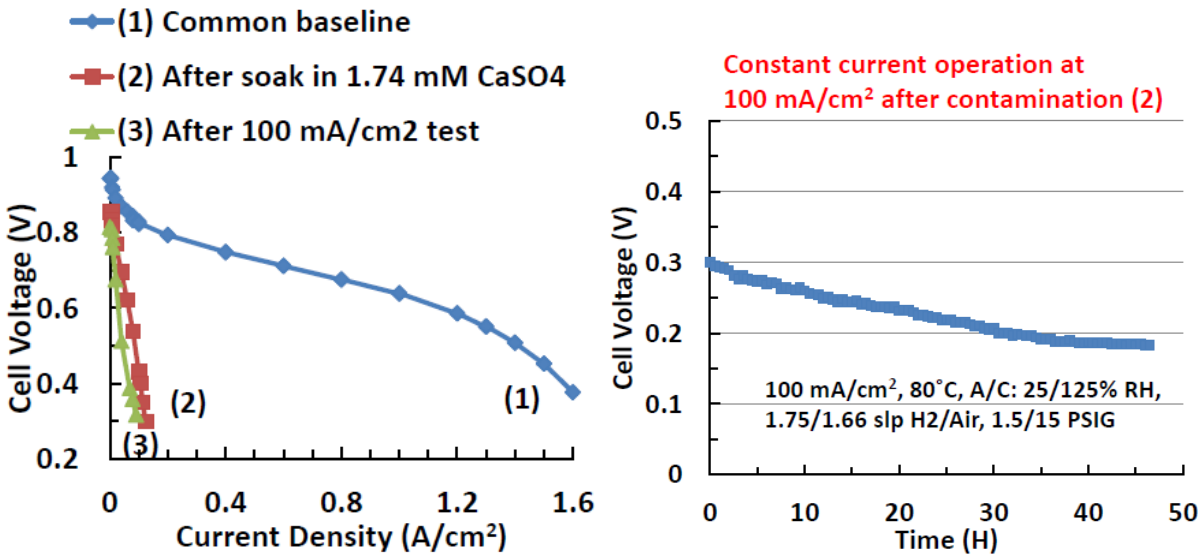

Figure 2.5.5. Comparison between a baseline polarization curve and others obtained after a $CaSO_4$ exposure (contamination method A, table 2.5.1) and operation at a low cell voltage after contaminant exposure (left). Subsequent transient cell performance data under different and wetter operating conditions after step 2 in the left figure (right).

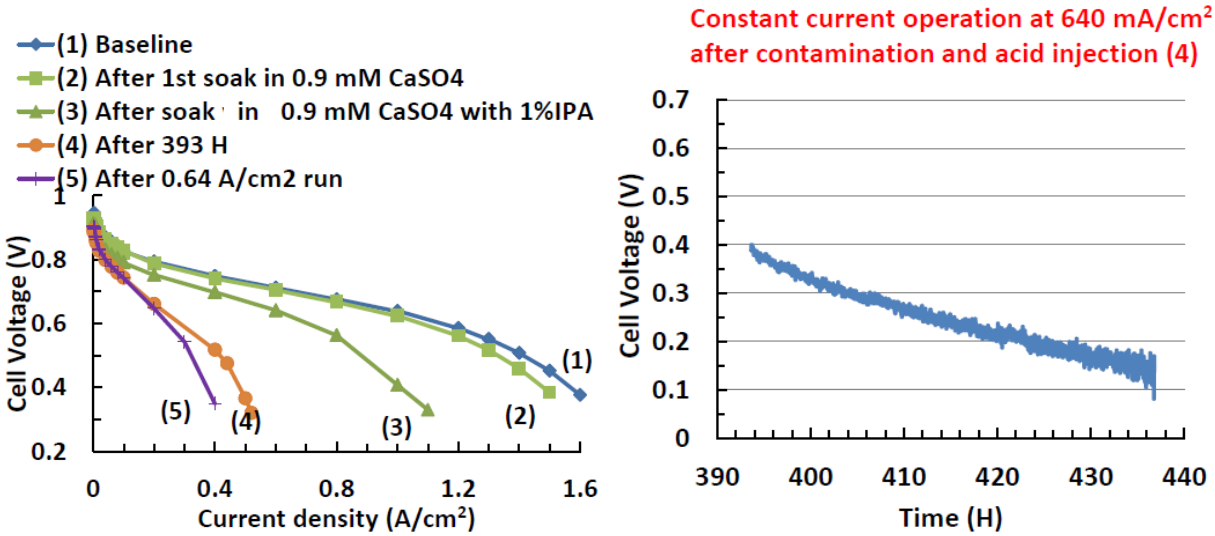

Figure 2.5.6. Comparison between a baseline polarization curve and others obtained after a $CaSO_4$ exposure (contamination method D, table 2.5.1) and operation at a low cell voltage after contaminant exposure (left). Subsequent transient cell performance data under different and wetter operating conditions after step 4 in the left figure (right).

The effect of a low cell voltage operation with a membrane/electrode assembly subjected to contamination method A (table 2.5.1) is shown in figure 2.5.5. This method assists foreign cation removal from the membrane by the high rate of water production at the cathode and the displacement of the foreign cations towards the cathode due to the predominant electric field effect. This particular recovery method was not effective. Cell operation under different and wetter operating conditions showed a decrease rather than an increase in cell voltage (figure 2.5.5, left). A similar conclusion was reached using the contamination method D (table 2.5.1). The polarization curve does not show any improvement (figure 2.5.6, left) even after the cell was operated up to 393 h with 10 mM H_2SO_4 at 0.4 V before operating the cell with a low voltage to remove the contaminant by ion exchange. Cell operation under different and wetter operating conditions for a substantial duration resulted in a continuous decrease in voltage (figure 2.5.6, right). In conclusion, cell operation at a low voltage does not have a significant impact on recovery irrespective of the contamination method.

The transient performance of a cell that was contaminated *ex situ* using method E (table 2.5.1) is shown in figure 2.5.7. It is observed that the initial injection of liquid water (baseline to separate the acid effect) decreases the cell performance by approximately 50 mV (section denoted 1). The subsequent and multiple step injection of an acid solution with or without iso-propanol (sections denoted 3 to 9) recovered a portion of the initial cell performance. A last injection with water only minimally affected the outcome (section denoted 10). *Ex situ* catalyst coated membrane analyses to determine the amount of Ca^{2+} remaining indicated similar trends with a significant loss in ion exchange capacity after contamination (although with contamination method B rather than E, table 2.5.1) and an incomplete recovery of the ion exchange capacity after the figure 2.5.7 test (figure 2.5.8).

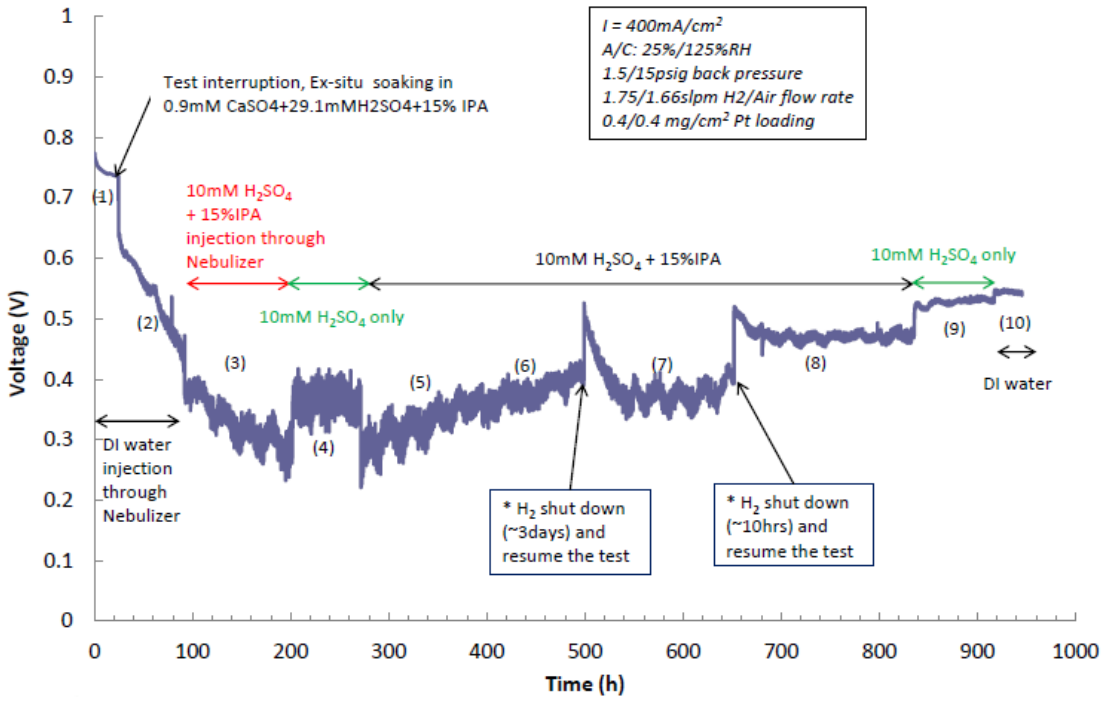

Figure 2.5.7. Transient cell performance obtained during in situ recovery of a membrane/electrode assembly contaminated ex situ with Ca^{2+}. Reprinted and reformatted with permission from *ECS Trans.*, **66** (24), 91 (2015). Copyright 2015, The Electrochemical Society.

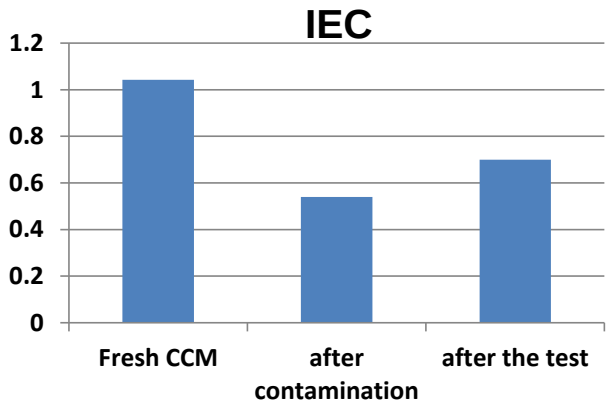

Figure 2.5.8. Catalyst coated membrane ion exchange capacity before and after contamination with Ca^{2+} and after the test. The after the test case includes recovery procedures. Reprinted and reformatted with permission from *ECS Trans.*, **66** (24), 91 (2015). Copyright 2015, The Electrochemical Society.

Water management significantly affects contamination by Ca^{2+} which may result in salt precipitation (mass transfer loss, figure 2.3.28, table 2.3.3). An *ex situ* wash with a dilute acidic solution was effective in removing salt deposits from the bipolar plate and gas diffusion layer (figure 2.5.9). Water was not able to remove salt from a gas diffusion layer.

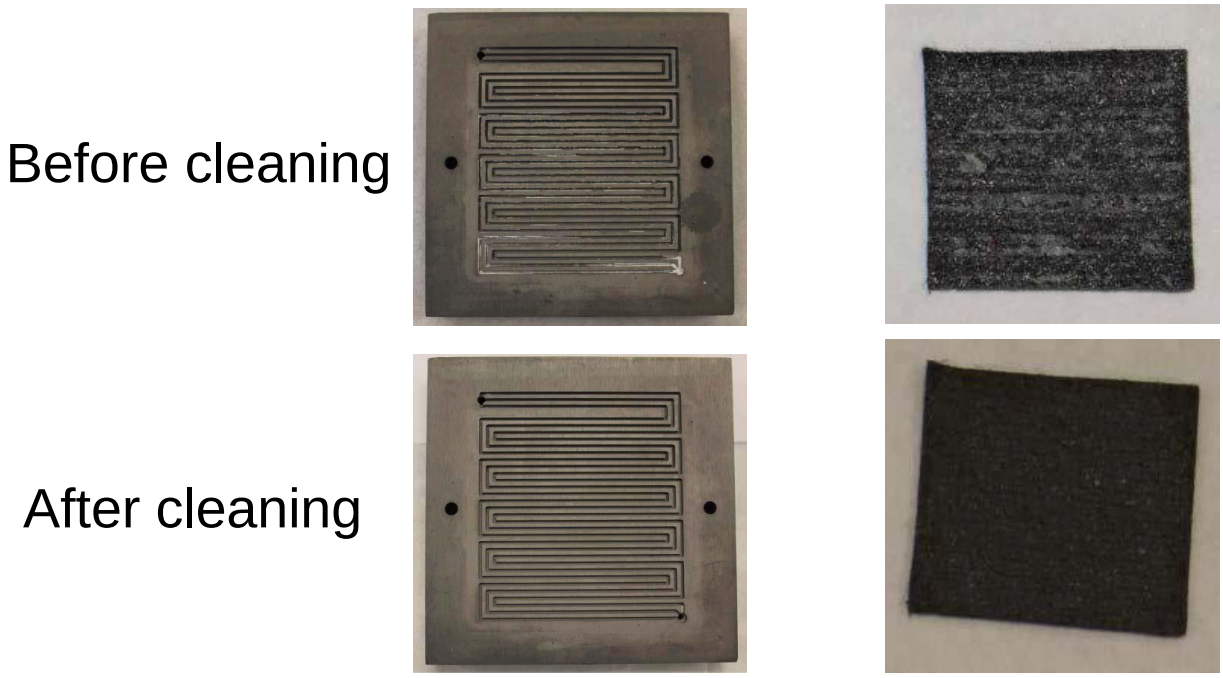

Figure 2.5.9. $CaSO_4$ salt deposits on a bipolar plate (top, left) and a gas diffusion layer (top, right). Exposure to a 1 mM H_2SO_4 solution for respectively 24 (bottom, left) and 60 h (bottom right) is sufficient to remove the salt deposits on the bipolar plate and gas diffusion electrode.

The effectiveness of recovery methods (*ex situ* or *in situ* acid wash, figures 2.5.4 and 2.5.7, low cell voltage operation, figures 2.5.5 and 2.5.6) for cells that were contaminated *ex situ* (without

salt precipitates) all showed an incomplete recovery. Sophisticated methods will be required to verify the contact between the acid solution and the ionomer, and improve the performance recovery. Furthermore, the impact of operating conditions on the salt dissolution rate may also play a role and therefore they should be investigated as well. For cells contaminated *in situ*, an *ex situ* acid wash was effective in removing salt precipitates (figure 2.5.9). It was deemed important to also determine the effectiveness of the in situ acid wash for an *in situ* contaminated cell, the most relevant situation for applications. These results are discussed in section 1.3 (figures 1.3.1, 1.3.2 and 1.3.3).

2.5.2 *Bromomethane*

Section 1.3 already contains data demonstrating the effectiveness of a two-steps recovery procedure following bromomethane contamination. Additional cyclic voltammetry data (not shown) indicated relatively clean cathode and anode Pt surfaces but lower catalyst active areas owing to significant operation times (several hundred h) for the unstable low 0.1 mg cm^{-2} cathode Pt loading catalyst coated membranes that were used.

2.6 Other activities not included in original milestones

2.6.1 *Pt loading effect*

The commercialization of fuel cell vehicles requires further reduction in cost. The Pt catalyst loading plays a significant role. However, at an early phase of the project, stable catalyst coated membranes with a low Pt loading were not available. Therefore, most tests were completed with a high catalyst loading of 0.4 mg Pt cm^{-2}. However, for the real world operation and mitigation strategies tasks (sections 2.4 and 2.5), most tests were completed with a commercially relevant loading of 0.1 mg Pt cm^{-2}. Additional tests were added to establish the effect of catalyst loading on the outcome of contamination by 2nd tier organic contaminants. These tests used operating conditions for the 1 A cm^{-2} and 80 °C case and contaminant concentrations that were common to other current density and temperature cases (table 2.2.1).

Figure 2.6.1 illustrates an exemplary comparison for the effect of acetylene with catalyst loadings of 0.1 and 0.4 mg Pt cm^{-2}. The dramatic increase in voltage loss during the contamination period (figure 2.6.1, left) indicated that a lower Pt loading is more sensitive to contaminants. Impedance spectra show increases in both mid-frequency (~10 Hz to ~1 kHz) and high frequency (~1 to ~10 Hz) loops respectively ascribed to respectively oxygen reduction and mass transfer (figure 2.6.1, right). These changes are more intense for the lower Pt loading.

Table 2.6.1 illustrates that the 75 % reduction in Pt catalyst loading from 0.4 to 0.1 mg cm^{-2} leads to a decrease in cell voltage at steady state due to contamination (the difference between the cell voltage before contamination and during contamination) that corresponds to a normalized increase in cell voltage loss generally exceeding 75 % and reaching values of 92 to 6,325 % (the difference in cell voltage loss at steady state between the 0.1 and 0.4 mg Pt cm^{-2} cells divided by the cell voltage loss for the 0.4 mg Pt cm^{-2} cell). As a result, filter system specifications either need to be revised or should be determined for commercially relevant Pt catalyst loadings. It is possible that for acetonitrile and bromomethane, their lesser effect is

related to hydrolysis, a reaction that is operative at all electrode potentials (figure 2.3.27, section 3.1, reference J23) and was not detected or suspected for the other contaminants.

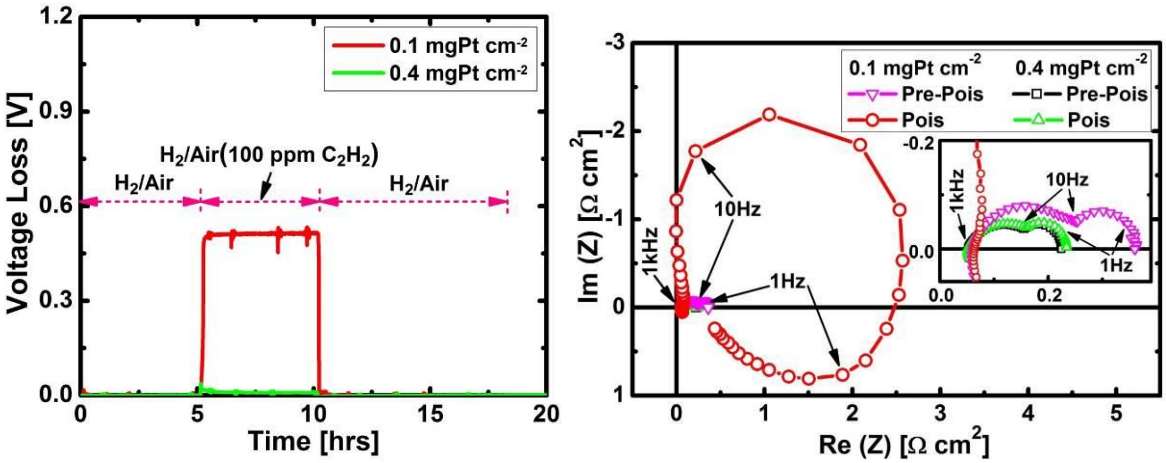

Figure 2.6.1. Cell voltage transients for a temporary acetylene contamination and different cathode catalyst loadings (left). Impedance spectra before and during acetylene contamination for different cathode catalyst loadings (right). The right figure inset is an enlargement of the main figure part located near the origin. Pre-Pois and Pois respectively refer to the period preceding contaminant injection and the contamination phase.

Table 2.6.1. Summary of the impact of a cathode catalyst loading reduction on steady state cell performance loss for seven airborne contaminants.

Contaminant	Acetonitrile	Acetylene	Bromomethane	Iso-propanol	Methyl methacrylate	Naphthalene	Propene
Cell voltage loss (% gain for a Pt loading reduction of 0.4 to 0.1 mg cm^{-2} in air at 80 °C)	58 (20 ppm)	6325 (100 ppm)	–10 (5 ppm)	92 (~8000 ppm)	104 (20 ppm)	187 (1.4 ppm)	224 (100 ppm)

2.6.2 *Cleansers screening*

The project scope was expanded with the objective to screen a number of commercially available cleansers and determine their impact on fuel cell performance. Eight cleansers were selected out of ~60 candidates and tested. A user survey (United States Fuel Cell Council, SAE International) was conducted. Availability and cost, absence of regulatory restrictions and safety hazards were employed as down selection criteria. It is emphasized that the cleansers are not specifically named to avoid issues with anti-trust legislation. A common cell design and operating conditions to maximize cleanser transport toward the cathode were used: 25 cm^2 cell, Gore membrane/electrode assembly (0.4/0.4 mg Pt cm^{-2}), 1 A cm^{-2}, 80 °C, air/H_2, 125/25 % relative humidity, 4/10 stoichiometry, ambient/ambient pressure at outlet, nebulizer injection for low vapor pressure and direct injection followed by vaporization for high vapor pressure cleansers (figure 2.1.5), 5 % (dilution by a factor of 20) of manufacturer's suggested full strength concentration (after 2 rinses). Other values were also studied for cleanser D, G and H. The test protocol follows the sequence: break in, diagnostics, baseline, diagnostics, contamination, diagnostics, clean up (deionized water flush) and diagnostics. Diagnostics include polarization

curve, impedance spectroscopy, cyclic voltammetry, and linear sweep voltammetry (gas crossover).

The major components of cleanser B include triethanolamine, ethoxylated alcohol and propylene glycol butyl ether (table 2.6.2). Figure 2.6.2 illustrates cleanser B results. A large performance loss >0.2 V is observed over a period of approximately 10 h. This loss was partially recovered by interrupting the cleanser injection with a cell voltage gain >0.1 V. Results for all eight cleansers are summarized (table 2.6.3) and already justify the need for such a study. None of the cleansers are well-suited for fuel cells either because the cell voltage was partially recoverable within a single vehicle fuel fill (~14 h), or the cell voltage fell below the power electronics low end operating point (0.45 V). Therefore, additional work is needed to identify a suitable cleanser, design an appropriate cleanser composition or develop cleaning alternatives for fuel cell components (such as cleanser removal).

Table 2.6.2. Cleanser B composition listed in the material safety data sheet.

Ingredient	CAS Number	Percent Range
Water	7732-18-5	≥ 78%
Triethanolamine	102-71-6	≤ 10%
Ethoxylated Alcohol	68439-46-3	≤ 5%
Propylene Glycol Butyl Ether	5131-66-8	≤ 5%
Tetrapotassium Pyrophosphate	7320-34-5	≤ 1%
Potassium Silicate	1312-76-1	≤ 1%
Colorant	Proprietary	≤ 1%

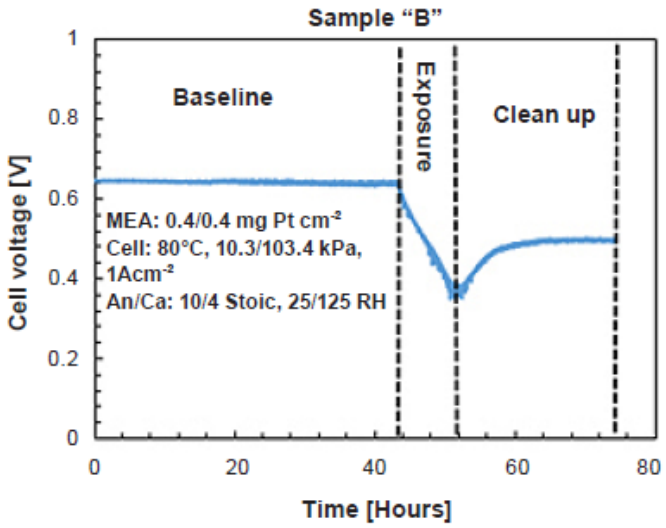

Figure 2.6.2. Voltage transients recorded during cleanser B evaluation.

2.6.3 *PtCo alloy contamination with SO_2*

It was deemed important to obtain information about Pt alloys under realistic operating conditions and reduce commercialization risks. Pt alloys are developed to minimize energy

losses associated with the reduction of oxygen to water [18]. The overwhelming majority of contamination studies were devoted to Pt (estimate of more than 99 %, section 3.1, reference C12). The impact of SO_2 was measured for both Pt and PtCo commercial catalysts with a concentration of 134 ppb (of the same order as the 75 ppb daily maximum over a 1 h period). A temporary sulfur dioxide injection of 20 min was used and diagnostics were completed before and after the contaminant injection period (polarization, cyclic voltammetry).

Table 2.6.3. Summary of the screened fuel cell components' cleansers, experimental parameters and key results.

Sample	Class	Principal component	Injection method	Concentration (%)	Injection rate (μL min^{-1})	Decay rate[a] (mV h^{-1})	Recovery (%)[b]
A	cationic	2-butoxyethanol	nebulizer	5	130	~1.4	~0
B	amine	triethanolamine	nebulizer	5	130	~22	~46
C	cationic	sodium dodecylbenzenesulfonate	nebulizer	5	130	<1.4	<0[c]
D	citrate	citrus terpenes	nebulizer	5	130	~1500	~96
				0.5	130	~2	~60
E	amine	sodium lauryl ether sulfate	nebulizer	5	130	<15	~25
F	amine	ethylenediaminetetraacetic acid	nebulizer	5	130	~3.3	<0[c]
G	organic	naphtha	nebulizer followed by vaporization	0.2	10	5[d]	~100
				1	50	100[d]	~100
				3	250	150[d]	~100
				3	250	240[d,e]	~100
H	organic	isopropanol	nebulizer followed by vaporization	0.2	10	70[d]	~90

[a] Baseline decay rate is ~0.2 mV h^{-1}. [b] After interruption of cleanser injection. [c] The cell voltage continues to drop during the recovery period. [d] Step change in mV. [e] 100 % relative humidity at the cathode.

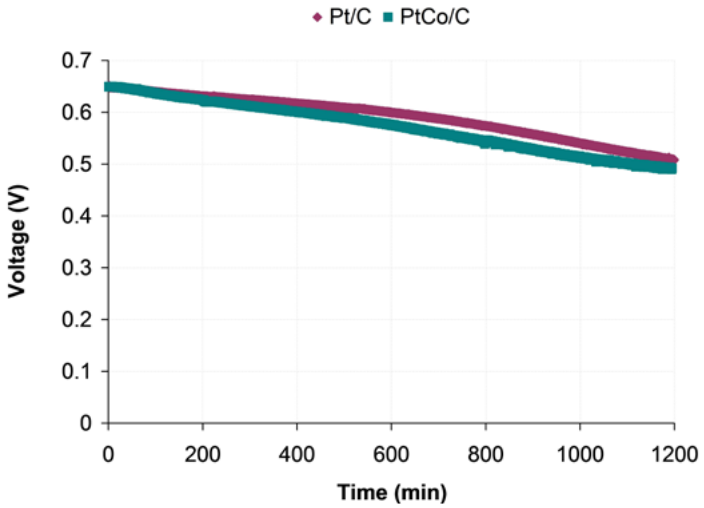

Figure 2.6.3. Comparison between single cell performance transients resulting from the injection of 134 ppb SO_2 in air for a Pt and a PtCo catalyst. 75 °C, 1.5 A cm^{-2}, 21.6 psig, 100 % relative humidity, air stoichiometry of 4, 20 h SO_2 exposure, 45 cm^2 active area, 0.4/0.1 mg Pt cm^{-2} for the cathode/anode.

Figure 2.6.3 summarizes the impact of a temporary exposure to SO_2 on Pt and PtCo catalysts. The cell voltage for both catalysts linearly decreases by ~150 mV without reaching a steady state.

After the contaminant injection was interrupted, the cell voltage partly recovered leaving 70 mV in irrecoverable losses after the polarization curve that followed the contamination period (not shown). Therefore, the alloy does not have an advantage in terms of contamination. This statement may not necessarily apply to other contaminants or other PtCo alloy compositions or structures. Also, results are consistent with other SO_2 contamination work which reveal that a recoverable contribution is present [19].

2.7 Outlook

The effects of 8 selected airborne contaminants that were not previously studied on the operation of a proton exchange membrane fuel cell were determined for different temperatures, current densities and contaminant concentrations. Additional tests and mathematical models were completed to derive contamination mechanisms and support the design of recovery procedures. It is emphasized that the material presented in this report only provides an overview of all data generated in this project. Therefore, the reader is directed to the published literature for a detailed account (section 3.1).

A substantial amount of work remains to be completed in this fuel cell degradation area. Only a few key topics are presented here to highlight this point. Many contaminants are worth investigating in more detail. For instance, 1,1-difluoroethane, chlorobenzene, ozone, toluene and vinyl acetate, which were only characterized to select species (table 2.1.3), all lead to a cell voltage loss at steady state that exceeds 0.1 V (table 2.1.5). Also, many contaminants that were identified (more than 200) could not be tested due to limited resources. Therefore, issues resulting from field tests of fuel cell vehicles are expected. Many contamination aspects are still poorly understood especially for low Pt loading electrodes which increase commercialization risks. These aspects include predictive capabilities, cleanser identification or development, stack effects, drive cycle impact, synergy between species in contaminant mixtures, etc. Several of these aspects will be explored by HNEI during the 2017 calendar year using Office of Naval Research funds and support from NIST. More specifically, planned activities include:

- Demonstration of the amplification effect of an airborne contaminant (benzene or propene) on the stack cell voltage (mal)distribution and the role of uneven air flow using different O_2 diluents (N_2, He, C_3F_8), gas flow configurations (U and Z type manifolding) and reactant stoichiometries
- Completion of binary air contaminant mixture tests to supplement previous test results using a ternary mixture (acetonitrile, bromomethane, propene, section 2.4.3) and single contaminants for the understanding of contaminant interactions
- Determination of the impact of contaminants (propene, methyl methacrylate) on the cathode hydrophilicity, water content and water management using the NIST neutron imaging facility
- Development of a method to predict cell degradation by contamination (oxygen reduction focus) based on rotating ring/disk electrode tests

3 Products

3.1 Publications, proceedings and presentations (task 4)

These project products are identified with a letter followed by a number (J for journal, C for conference proceedings and M for conference presentations). The total number of these products is currently equal to 75 (26 journal papers, 20 conference proceedings and 29 conference presentations). A significant amount of material has not yet been published. As a result, journal papers J27 to J43 are planned to be completed during the 2017 calendar year (J33, J34, J36 and J41 manuscripts have already been submitted).

J43. T. T. H. Cheng, J. St-Pierre, 'SO_2 Contamination in PEMFC - A Comparison between Membrane Electrode Assemblies with Pt/C and PtCo/C Cathodes', *J. Power Sources*, in preparation.

J42. J. St-Pierre, J. Qi, Y. Zhai, 'PEMFC Contamination Model: Neutral Species Sorption by Ionomer', *J. Electrochem. Soc*., in preparation.

J41. J. Qi, J. Ge, M. A. Uddin, Y. Zhai, U. Pasaogullari, J. St-Pierre, 'Evaluation of Cathode Catalyst Contamination with Ca^{2+} in Proton Exchange Membrane Fuel Cells using a Rotating Ring Disk Electrode', *Electrochim. Acta*, submitted.

J40. Y. Zhai, J. St-Pierre, J. Ge, J. Qi, K. More, 'Long Term Effects of an Airborne Contaminant on a Proton Exchange Membrane Fuel Cell', *J. Electrochem. Soc*., in preparation.

J39. J. Ge, Y. Zhai, J. St-Pierre, 'Effects of Propene Redox Behavior on the AC Impedance Responses of a PEMFC during Contamination - Overlapping Kinetic and Mass Transfer Contributions', *Energy Environ. Sci*., in preparation.

J38. J. St-Pierre, Y. Zhai, 'Impact of the Cathode Pt Loading on PEMFC Contamination by several Airborne Contaminants', *J. Electrochem. Soc*., in preparation.

J37. J. St-Pierre, Y. Zhai, 'Proton Exchange Membrane Fuel Cell Contamination Models - Validation of Cathode Kinetic Contributions with Airborne Species', *J. Electrochem. Soc*., in preparation.

J36. T. V. Reshetenko, J. St-Pierre, 'Study of Spatial PEMFC Performance under Propylene, Methyl Methacrylate and Isopropanol Exposure', *J. Power Sources*, in preparation.

J35. J. Qi, Y. Zhai, J. St-Pierre, 'Airborne, Organic Contaminant Mixtures' Effects on PEMFCs', *J. Electrochem. Soc*., in preparation.

J34. Y. Zhai, J. St-Pierre, 'Tolerance and Mitigation Strategies of PEMFCs Subject to Acetylene Contamination', *J. Power Sources*, submitted.

J33. Y. Zhai, J. St-Pierre, 'Impact of Operating Conditions on the Acetylene Contamination in the Cathode of PEM Fuel cells', *J. Power Sources*, submitted.

J32. Y. Zhai, J. St-Pierre, J. Ge, 'Acetonitrile Contamination Reactions in a PEMFC', *ChemElectroChem*, in preparation.

J31. Y. Zhai, J. St-Pierre, 'Impact of Operating Conditions on Acetonitrile Contamination of a PEMFC', *J. Power Sources*, in preparation.

J30. Y. Zhai, J. St-Pierre, 'Contamination Impact of Propene on a PEMFC', *J. Power Sources*, in preparation.

J29. Y. Zhai, J. Ge, J. St-Pierre, 'Contamination Impact of 2-propanol on a PEMFC', *J. Electrochem. Soc*., in preparation.

J28. Y. Zhai, J. St-Pierre, 'Contamination Impact of Naphthalene on a PEMFC', *J. Power Sources*, in preparation.

J27. Y. Zhai, J. St-Pierre, 'Contamination Impact of Methyl Methacrylate on a PEMFC', *J. Electrochem. Soc*., in preparation.

J26. C. J. Banas, L. Bonville, U. Pasaogullari, 'Linking Foreign Cationic Contamination of PEM Fuel Cells to the Local Water Distribution', *J. Electrochem. Soc*., **164** (2017) F1100.

J25. Y. Zhai, J. St-Pierre, 'Acetylene Contamination Mechanisms in the Cathode of Proton Exchange Membrane Fuel Cells', *ChemElectroChem*, **4** (2017) 655.

J24. T. V. Reshetenko, K. Artyushkova, J. St-Pierre, 'Spatial Proton Exchange Membrane Fuel Cell Performance Under Bromomethane Poisoning', *J. Power Sources*, **342** (2017) 135.

J23. T. V. Reshetenko, J. St-Pierre, 'Study of the Aromatic Hydrocarbons Poisoning of Platinum Cathodes on Proton Exchange Membrane Fuel Cell Spatial Performance Using a Segmented Cell System', *J. Power Sources*, **333** (2016) 236.

J22. M. A. Uddin, J. Park, L. Bonville, U. Pasaogullari, 'Effect of Hydrophobicity of Gas Diffusion Layer in Calcium Cation Contamination in Polymer Electrolyte Fuel Cells', *Int. J. Hydrogen Energy*, **41** (2016) 14909.

J21. Y. Zhai, O. Baturina, D. Ramaker, E. Farquhar, J. St-Pierre, K. Swider-Lyons, 'Bromomethane Contamination in the Cathode of Proton Exchange Membrane Fuel Cells', *Electrochim. Acta*, **213** (2016) 482.

J20. Y. Zhai, J. Ge, J. St-Pierre, 'The Ionic Conductivity and Catalyst Activity Effects of Acetonitrile on Proton Exchange Membrane Fuel Cells', *Electrochem. Commun*., **66** (2016) 49.

J19. J. St-Pierre, Y. Zhai, J. Ge, 'Relationships between PEMFC Cathode Kinetic Losses and Contaminants' Dipole Moment and Adsorption Energy on Pt', *J. Electrochem. Soc.*, **163** (2016) F247.

J18. M. A. Uddin, J. Qi, X. Wang, U. Pasaogullari, L. J. Bonville, 'Distributed Cation Contamination from Cathode to Anode Direction in Polymer Electrolyte Fuel Cells', *Int. J. Hydrogen Energy*, **40** (2015) 13099.

J17. M. A. Uddin, X. Wang, J. Qi, M. O. Ozdemir, U. Pasaogullari, L. Bonville, T. Molter, 'Effect of Chloride on PEFCs in Presence of Various Cations', *J. Electrochem. Soc.*, **162** (2015) F373.

J16. Y. Zhai, O. Baturina, D. Ramaker, E. Farquhar, J. St-Pierre, K. Swider-Lyons, 'Chlorobenzene Poisoning and Recovery of Platinum-Based Cathodes in Proton Exchange Membrane Fuel Cells', *J. Phys. Chem. C*, **119** (2015) 20328.

J15. T. V. Reshetenko, J. St-Pierre, 'Study of the Acetonitrile Poisoning of Platinum Cathodes on Proton Exchange Membrane Fuel Cell Spatial Performance Using a Segmented Cell System', *J. Power Sources*, **293** (2015) 929.

J14. T. V. Reshetenko, J. St-Pierre, 'Study of Acetylene Poisoning of Pt Cathode on Proton Exchange Membrane Fuel Cell Spatial Performance Using a Segmented Cell System', *J. Power Sources*, **287** (2015) 401.

J13. Y. Zhai, J. St-Pierre, 'Proton Exchange Membrane Fuel Cell Cathode Contamination - Acetylene', *J. Power Sources*, **279** (2015) 165.

J12. M. A. Uddin, X. Wang, J. Park, U. Pasaogullari, L. Bonville, 'Distributed Effects of Calcium Ion Contaminant on Polymer Electrolyte Fuel Cell Performance', *J. Power Sources*, **296** (2015) 64.

J11. J. Qi, X. Wang, M. O. Ozdemir, M. A. Uddin, L. Bonville, U. Pasaogullari, T. Molter, 'Effect of Cationic Contaminants on Polymer Electrolyte Fuel Cell Performance', *J. Power Sources*, **286** (2015) 18.

J10. J. Ge, J. St-Pierre, Y. Zhai, 'PEMFC Cathode Catalyst Contamination Evaluation with a RRDE - Propene and Naphthalene', *Electrochim. Acta*, **138** (2014) 437.

J9. J. Ge, J. St-Pierre, Y. Zhai, 'PEMFC Cathode Catalyst Contamination Evaluation with a RRDE - Acetonitrile', *Electrochim. Acta*, **134** (2014) 272.

J8. J. Ge, J. St-Pierre, Y. Zhai, 'PEMFC Cathode Catalyst Contamination Evaluation with a RRDE - Acetylene', *Electrochim. Acta*, **133** (2014) 65.

J7. J. Ge, J. St-Pierre, Y. Zhai, 'PEMFC Cathode Catalyst Contamination Evaluation with a RRDE - Methyl Methacrylate', *Int. J. Hydrogen Energy*, **39** (2014) 18351.

J6. J. St-Pierre, B. Wetton, Y. Zhai, J. Ge, 'Liquid Water Scavenging of PEMFC Contaminants', *J. Electrochem. Soc.*, **161** (2014) E3357.

J5. M. A. Uddin, U. Pasaogullari, 'Computational Modeling of Foreign Cation Contamination in PEFCs', *J. Electrochem. Soc.*, **161** (2014) F1081.

J4. X. Wang, J. Qi, O. Ozdemir, A. Uddin, U. Pasaogullari, L. J. Bonville, T. Molter, 'Ca^{2+} as an Air Impurity in Polymer Electrolyte Membrane Fuel Cells', *J. Electrochem. Soc.*, **161** (2014) F1006.

J3. J. St-Pierre, Y. Zhai, M. S. Angelo, 'Effect of Selected Airborne Contaminants on PEMFC Performance', *J. Electrochem. Soc.*, **161** (2014) F280 and *J. Electrochem. Soc.*, **162** (2015) X7.

J2. J. Qi, X. Wang, U. Pasaogullari, L. Bonville, T. Molter, 'Effect of Al^{3+} Contaminant on Polymer Electrolyte Fuel Cell Performance', *J. Electrochem. Soc*., **160** (2013) F916.

J1. J. St-Pierre, Y. Zhai, M. Angelo, 'Quantitative Ranking Criteria for PEMFC Contaminants', *Int. J. Hydrogen Energy*, **37** (2012) 6784.

C20. J. Banas, U. Pasaogullari, 'Computational Modelling of Cationic Transport in PEFCs: a Multiphase Mixture Approach', *Electrochem. Soc. Trans*., **75**(14) (2016) 671.

C19. C. J. Banas, U. Pasaogullari, 'Statistical Analysis of Salt Deposition inside PEFC GDL from X-Ray Tomography', *Electrochem. Soc. Trans*., **69**(17) (2015) 511.

C18. J. Park, M. A. Uddin, S. Ganesan, U. Pasaogullari, L. Bonville, T. Molter, 'Effects on Wetting Agents in Cationic Contamination and Mitigation in PEFCs', *Electrochem. Soc. Trans.*, **66**(24) (2015) 91.

C17. M. A. Uddin, J. Park, S. Ganesan, U. Pasaogullari, L. Bonville, T. Molter, 'A Cationic Contamination in PEFC Cathode: A Cause and Effect Study', *Electrochem. Soc. Trans.*, **66**(24) (2015) 29.

C16. S. Ganesan, M. A. Uddin, J. Park, U. Pasaogullari, L. Bonville, T. Molter, 'Impact of Cationic Impurities on Low-Pt Loading PEFC Cathodes', *Electrochem. Soc. Trans.*, **66**(24) (2015) 19.

C15. Y. Zhai, J. St-Pierre, J. Ge, 'PEMFC Cathode Contamination Evaluation with Membrane Conductivity Cell, CA, CP, CV, EIS, GC/MS and ISE - Acetonitrile', *Electrochem. Soc. Trans*., **64**(3) (2014) 805.

C14. M. A. Uddin, U. Pasaogullari, T. Molter, 'Computational Modelling of Cation Contamination in PEFCs', *Electrochem. Soc. Trans*., **64**(3) (2014) 705.

C13. M. A. Uddin, J. Park, X. Wang, J. Qi, U. Pasaogullari, L. J. Bonville, T. Molter, 'The Role of Gas Diffusion Layer in Cationic Contamination and Mitigation in Polymer Electrolyte Fuel Cells', *Electrochem. Soc. Trans.*, **64**(3) (2014) 537.

C12. J. St-Pierre, M. Angelo, K. Bethune, J. Ge, S. Higgins, T. Reshetenko, M. Virji, Y. Zhai, 'PEMFC Contamination - Fundamentals and Outlook', *Electrochem. Soc. Trans.*, **61**(23) (2014) 1.

C11. M. A. Uddin, X. Wang, M. O. Ozdemir, J. Qi, L. Bonville, U. Pasaogullari, T. Molter, 'Distributed PEFC Performance during Cationic Contamination', *Electrochem. Soc. Trans.*, **61**(12) (2014) 49.

C10. M. A. Uddin, J. Qi, X. Wang, M. O. Ozdemir, N. Khajeh-Hosseini-Dalasm, L. Bonville, U. Pasaogullari, T. Molter, 'Study of Through Plane Cation Contamination in Polymer Electrolyte Fuel Cell', *Electrochem. Soc. Trans.*, **61**(12) (2014) 37.

C9. M. A. Uddin, X. Wang, J. Qi, M. O. Ozdemir, L. Bonville, U. Pasaogullari, T. Molter, 'Effects of Chloride Contamination on PEFCs', *Electrochem. Soc. Trans.*, **58**(1) (2013) 543.

C8. J. Qi, X. Wang, M. O. Ozdemir, M. A. Uddin, L. Bonville, U. Pasaogullari, T. Molter, 'Effect of Cationic Contaminants on Polymer Electrolyte Fuel Cell Performance', *Electrochem. Soc. Trans.*, **58**(1) (2013) 537.

C7. X. Wang, J. Qi, O. Ozdemir, U. Pasaogullari, L. J. Bonville, T. Molter, 'Effect of Ca^{2+} as an Air Impurity on Polymer Electrolyte Fuel Cells', *Electrochem. Soc. Trans.*, **58**(1) (2013) 529.

C6. J. St-Pierre, J. Ge, Y. Zhai, T. V. Reshetenko, M. Angelo, 'PEMFC Cathode Contamination Mechanisms for Several VOCs - Acetonitrile, Acetylene, Bromomethane, Iso-propanol, Methyl Methacrylate, Naphthalene and Propene', *Electrochem. Soc. Trans.*, **58**(1) (2013) 519.

C5. Y. Zhai, J. St-Pierre, J. Ge, 'PEMFC Cathode Contamination with Acetylene - Potential Dependency', *Electrochem. Soc. Trans.*, **58**(1) (2013) 507.

C4. B. Wetton, J. St-Pierre, 'Liquid Water Scavenging of PEMFC Contaminants', *Electrochem. Soc. Trans.*, **50**(2) (2012) 649.

C3. Y. Zhai, J. St-Pierre, M. Angelo, 'The Impact of Operating Conditions on the Performance Effect of Selected Airborne PEMFC Contaminants', *Electrochem. Soc. Trans.*, **50**(2) (2012) 635.

C2. J. St-Pierre, 'PEMFC Contamination Model: Neutral Species Sorption by Ionomer', *Electrochem. Soc. Trans.*, **41**(1) (2011) 307.

C1. J. St-Pierre, M. S. Angelo, Y. Zhai, 'Focusing Research by Developing Performance Related Selection Criteria for PEMFC Contaminants', *Electrochem. Soc. Trans.*, **41**(1) (2011) 279.

M29. T. Reshetenko, J. St-Pierre, 'Influence of Aromatic Hydrocarbons in Air on Spatial PEMFC Performance', in Meeting Abstracts, Electrochemical Society volume 2016-2, The

Electrochemical Society, Pennington, NJ, 2016, abstract 2716 (230th Electrochemical Society meeting poster presentation).

M28. T. Reshetenko, K. Artyushkova, J. St-Pierre, 'Comprehensive Studies of Spatial PEMFC Performance Under CH_3Br Poisoning of Cathode', in Meeting Abstracts, Electrochemical Society volume 2016-2, The Electrochemical Society, Pennington, NJ, 2016, abstract 2701 (230th Electrochemical Society meeting poster presentation).

M27. Y. Zhai, O. Baturina, D. Ramaker, J. St-Pierre, K. Swider-Lyons, 'The Effect of Airborne Bromomethane Contamination on PEMFC Performance', in Meeting Abstracts, Electrochemical Society volume 2016-2, The Electrochemical Society, Pennington, NJ, 2016, abstract 2520 (230th Electrochemical Society meeting oral presentation).

M26. J. St-Pierre, Y. Zhai, J. Ge, 'Prediction Method for PEMFC Cathode Kinetic Losses Induced by Contaminants', in *Meeting Abstracts*, Electrochemical Society volume 2015-2, The Electrochemical Society, Pennington, NJ, 2015, abstract 1528 (228th Electrochemical Society meeting oral presentation).

M25. Y. Zhai, J. Ge, J. St-Pierre, 'Long Term Effects of Airborne Contaminants in PEMFC Cathode', in *Meeting Abstracts*, Electrochemical Society volume 2015-2, The Electrochemical Society, Pennington, NJ, 2015, abstract 1508 (228th Electrochemical Society meeting oral presentation).

M24. C. J. Banas, U. Pasaogullari, 'Statistical Analysis of Salt Deposition inside PEFC GDL from X-Ray Tomography', in *Meeting Abstracts*, Electrochemical Society volume 2015-2, The Electrochemical Society, Pennington, NJ, 2015, abstract 1358 (228th Electrochemical Society meeting oral presentation).

M23. Y. Zhai, J. Ge, J. Qi, K. More, J. St-Pierre, 'Long Term Effects of an Airborne Contaminant on a Proton Exchange Membrane Fuel Cell', 3rd International Workshop on Degradation Issues of Fuel Cells and Electrolysers, Santorini, Greece, September 29 - October 1, 2015 (oral presentation).

M22. Y. Zhai, J. Ge, J. St-Pierre, 'Long Term Effects of an Airborne Contaminant on a Proton Exchange Membrane Fuel Cell', 15th International Symposium on Electroanalytical Chemistry, Changchun, China, August 13-16, 2015, abstract K-4 (oral presentation).

M21. M. A. Uddin, J. Park, U. Pasaogullari, L. J. Bonville, 'Cation Contamination in Polymer Electrolyte Fuel Cells: Impacts, Mechanisms, and Mitigation', in *Meeting Abstracts*, Electrochemical Society volume 2015-3, The Electrochemical Society, Pennington, NJ, 2015, abstract 647 (Electrochemical Society Conference on Electrochemical Energy Conversion & Storage with SOFC-XIV, poster presentation).

M20. J. Park, S. Ganesan, M. A. Uddin, U. Pasaogullari, L. J. Bonville, 'A Study of Cationic Contamination and Mitigation on GDL/MPL Wettability and Metallic Plate Corrosion for PEFCs', in *Meeting Abstracts*, Electrochemical Society volume 2015-3, The Electrochemical

Society, Pennington, NJ, 2015, abstract 614 (Electrochemical Society Conference on Electrochemical Energy Conversion & Storage with SOFC-XIV, oral presentation).

M19. T. V. Reshetenko, J. St-Pierre, 'Study of Spatial PEMFC Performance under CH_3CN Poisoning', in 2014 Fuel Cell Seminar & Energy Exposition Abstracts, South Carolina Hydrogen and Fuel Cell Alliance, Columbia, SC, 2014, abstract 56 (oral presentation).

M18. Y. Zhai, J. St-Pierre, J. Ge, 'PEMFC Cathode Contamination Evaluation with Membrane Conductivity Cell, CA, CV and GC/MS - Acetonitrile', in *Meeting Abstracts*, Electrochemical Society volume 2014-2, The Electrochemical Society, Pennington, NJ, 2014, abstract 1271 (226th Electrochemical Society meeting oral presentation).

M17. Y. Zhai, O. Baturina, D. E. Ramaker, J. St-Pierre, K. E. Swider-Lyons, 'Contamination and Recovery of PEMFC Cathodes with Organohalides: Chlorobenzene and Bromomethane', in *Meeting Abstracts*, Electrochemical Society volume 2014-2, The Electrochemical Society, Pennington, NJ, 2014, abstract 1268 (226th Electrochemical Society meeting oral presentation).

M16. M. A. Uddin, J. Park, X. Wang, J. Qi, M. O. Ozdemir, U. Pasaogullari, L. J. Bonville, T. Molter, 'The Role of Gas Diffusion Layer in Cationic Contamination and Mitigation in Polymer Electrolyte Fuel Cells', in *Meeting Abstracts*, Electrochemical Society volume 2014-2, The Electrochemical Society, Pennington, NJ, 2014, abstract 1229 (226th Electrochemical Society meeting oral presentation).

M15. M. A. Uddin, U. Pasaogullari, T. Molter, 'Computational Modelling of Cation Contamination in PEFCs', in *Meeting Abstracts*, Electrochemical Society volume 2014-2, The Electrochemical Society, Pennington, NJ, 2014, abstract 1033 (226th Electrochemical Society meeting oral presentation).

M14. J. St-Pierre, M. Angelo, K. Bethune, J. Ge, Scott Higgins, T. Reshetenko, M. Virji, Y. Zhai, 'PEMFC Contamination – Fundamentals and Outlook', in *Meeting Abstracts*, Electrochemical Society volume 2014-1, The Electrochemical Society, Pennington, NJ, 2014, abstract 796 (225th Electrochemical Society meeting oral presentation).

M13. M. A. Uddin, X. Wang, M. O. Ozdemir, J. Qi, L. Bonville, U. Pasaogullari, T. Molter, 'Distributed PEFC Performance during Cationic Contamination', in *Meeting Abstracts*, Electrochemical Society volume 2014-1, The Electrochemical Society, Pennington, NJ, 2014, abstract 638 (225th Electrochemical Society meeting oral presentation).

M12. M. A. Uddin, J. Qi, X. Wang, M. O. Ozdemir, N. K. H. Dalasm, L. Bonville, U. Pasaogullari, T. Molter , 'Study of through Plane Cation Contamination in Polymer Electrolyte Fuel Cell', in *Meeting Abstracts*, Electrochemical Society volume 2014-1, The Electrochemical Society, Pennington, NJ, 2014, abstract 637 (225th Electrochemical Society meeting oral presentation).

M11. M. A. Uddin, X. Wang, J. Qi, M. O. Ozdemir, L. Bonville, U. Pasaogullari, T. Molter, 'Effects of Chloride Contamination on PEFCs', in *Meeting Abstracts*, Electrochemical Society

volume 2013-2, The Electrochemical Society, Pennington, NJ, 2013, abstract 1334 (224th Electrochemical Society meeting oral presentation).

M10. J. Qi, X. Wang, M. O. Ozdemir, M. A. Uddin, L. Bonville, U. Pasaogullari, T. Molter, 'Effect of Cationic Contaminants on Polymer Electrolyte Fuel Cell Performance', in *Meeting Abstracts*, Electrochemical Society volume 2013-2, The Electrochemical Society, Pennington, NJ, 2013, abstract 1333 (224th Electrochemical Society meeting oral presentation).

M9. X. Wang, J. Qi, O. Ozdemir, U. Pasaogullari, L. J. Bonville, T. Molter, 'Effect of Ca^{2+} as an Air Impurity on Polymer Electrolyte Fuel Cells', in *Meeting Abstracts*, Electrochemical Society volume 2013-2, The Electrochemical Society, Pennington, NJ, 2013, abstract 1332 (224th Electrochemical Society meeting oral presentation).

M8. J. St-Pierre, J. Ge, Y. Zhai, T. Reshetenko, M. Angelo, 'PEMFC Cathode Contamination Mechanisms for Several VOCs - Acetonitrile, Acetylene, Bromomethane, Iso-Propanol, Methyl Methacrylate, Naphthalene and Propene', in *Meeting Abstracts*, Electrochemical Society volume 2013-2, The Electrochemical Society, Pennington, NJ, 2013, abstract 1330 (224th Electrochemical Society meeting oral presentation).

M7. Y. Zhai, J. St-Pierre, J. Ge, 'PEMFC Cathode Contamination with Acetylene - Potential Dependency', in *Meeting Abstracts*, Electrochemical Society volume 2013-2, The Electrochemical Society, Pennington, NJ, 2013, abstract 1329 (224th Electrochemical Society meeting oral presentation).

M6. T. Reshetenko, J. St-Pierre, 'The Impact of Selected Air Pollutants on Spatial PEMFC Performance', in *Meeting Abstracts*, Electrochemical Society volume 2013-2, The Electrochemical Society, Pennington, NJ, 2013, abstract 1328 (224th Electrochemical Society meeting oral presentation).

M5. J. Ge, Y. Zhai, J. St-Pierre, 'An RRDE Evaluation of the C_2H_2 Effect on the ORR', in *Meeting Abstracts*, Electrochemical Society volume 2013-2, The Electrochemical Society, Pennington, NJ, 2013, abstract 1302 (224th Electrochemical Society meeting oral presentation).

M4. B. Wetton, J. St-Pierre, 'Liquid Water Scavenging of PEMFC Contaminants', in *Meeting Abstracts*, Electrochemical Society volume 2012-2, The Electrochemical Society, Pennington, NJ, 2012, abstract 1296 (222th Electrochemical Society meeting oral presentation).

M3. Y. Zhai, M. Angelo, J. St-Pierre, 'The Impact of Operating Conditions on the Performance Effect of Selected Airborne PEMFC Contaminants', in *Meeting Abstracts*, Electrochemical Society volume 2012-2, The Electrochemical Society, Pennington, NJ, 2012, abstract 1294 (222th Electrochemical Society meeting oral presentation).

M2. J. St-Pierre, K. O'Leary, 'PEMFC Contamination Model: Neutral Species Sorption by Ionomer', in *Meeting Abstracts*, Electrochemical Society volume 2011-2, The Electrochemical Society, Pennington, NJ, 2011, abstract 1132 (220th Electrochemical Society meeting oral presentation).

M1. J. St-Pierre, M. Angelo, Y. Zhai, 'Focusing Research by Developing Performance Related Selection Criteria for PEMFC Contaminants', in *Meeting Abstracts*, Electrochemical Society volume 2011-2, The Electrochemical Society, Pennington, NJ, 2011, abstract 1035 (220th Electrochemical Society meeting oral presentation).

3.2 Networks or collaborations (task 4)

3.2.1 *DOE programs*

The project team regularly attended and contributed to the DOE durability working group (Feb. 28 and Dec. 18, 2013, Jun. 16 and Dec. 16, 2014, May 28, 2015 and May 11-12, 2016 workshops). A rotating ring/disc electrode was used to evaluate the impact of contaminants on the oxygen reduction mechanism (section 2.3). The inverted rotating disc electrode technique was used to coat the disc with a more uniform catalyst ink film which was developed by collaborators at the Naval Research Laboratory, transferred to HNEI and cross validated with NRL [20] for use within this project. Subsequently, technique details were submitted to the DOE RFI DE-FOA-0000926, RDE method development for catalyst characterization. The PI also attended project ID # FC048 team meetings for mutual support including activities overlap avoidance. Discussions took place with the Argonne National Laboratory to extend mechanistic studies for foreign cation contaminants with the use of X-ray scattering and Pt single crystals to determine the shortest distance of approach between foreign cations and the Pt surface (changes in ion charge and size were considered). It was assumed that the change in charge distribution near the Pt surface impacts the oxygen reduction mechanism (including the hydrogen peroxide formation side reaction). In section 2.4.1, it was mentioned that membrane/electrode assembly samples were sent Oak Ridge National Laboratory for characterization to supplement data analysis.

3.2.2 *Other collaborations*

For the first milestone (section 2.1), the Fuel Cell Tech Team (coolants) as well as Nuvera (indoor contaminants) suggested 4 additional atmospheric species for screening. General Motors, Nuvera, and UTC Power provided air filters for residue analysis to support the selection of road side contaminants. The amended list of contaminants was subsequently circulated to a wide audience of stakeholders for validation (LANL, NREL, ANL, FCHEA, NRL, SAE, NIST, Praxair, Air Liquide, Air Products, Carrier, CaFCP, CaSFCC, EPA, NCAR, Nuvera, CARB, AFCC, NASA, NEDO/JARI). General Motors also provided a nebulizer design and operation instructions and a heating tube for, respectively, the injection of foreign cation contaminants dissolved in aqueous solutions and the sublimation of solids (naphthalene, 2,2-bis(4-hydroxyphenyl)propane).

For the third milestone (section 2.3), equipment acquired by HNEI using an Office of Naval Research award (rotating ring/disc electrode, membrane conductivity cell, gas chromatograph/mass spectrograph) were employed to support the development of contamination mechanisms. Along the same line, the Naval Research Laboratory and George Washington University provided halogenated compounds (bromomethane, chlorobenzene) X-ray absorption spectroscopy measurements to clarify contamination mechanisms (section 3.1, references J16

and J21). Finally, metallic bipolar plates manufactured by TreadStone Technologies were acquired to study interactions with bromomethane and Ca^{2+} contaminants.

General Motors provided ethylene glycol (coolant) data to validate a model for membrane contamination by a chemically and electrochemically inactive species (section 3.5.2). The liquid water scavenging of a gaseous contaminant model (section 3.5.1) was developed in collaboration with the University of British Columbia.

Air composition and filter specification definition support were provided to Nuvera and ClearEdge Power at their request. More recently, Nuvera requested filter characterization tests to support fuel cell deployments using HNEI filter test stand. These outreach activities were supplemented by presentations (in addition to those listed in section 3.1) to General Motors (Jun. 9, 2014) and SAE (Jun. 10, 2014, Mar. 10 and Nov. 3, 2015).

3.3 Technologies or techniques

In section 3.2.2, it was mentioned that General Motors supplied the University of Connecticut and HNEI with respectively a nebulizer design (figure 2.1.5) and operation instructions and a heating tube for the injection of foreign cation contaminants dissolved in aqueous solutions and the sublimation of solids.

3.4 Provisional patent

The following provisional patent was inspired by mechanistic contamination knowledge generated in this project. It pertains to a method to measure the active area of a catalyst covered by an ionomer using the same sample. Work is currently ongoing to demonstrate the concept.

J. St-Pierre, J. Ge, 'Fuel cell catalyst ink active surface area measurement', United States provisional patent 62/262,137, December 2, 2015.

A new fuel cell contamination recovery procedure inspired by this project results is also planned for demonstration within an Office of Naval Research funded program at HNEI during the 2017 calendar year. However, details cannot be provided at this time to safeguard patenting options.

3.5 Mathematical models (task 3)

Three mathematical models were conceived during the project. Only one is described in some detail here (section 3.1, reference J5) because the other two yielded easily implemented analytical solutions (section 3.1, references J6, C2).

3.5.1 *Product liquid water scavenging of contaminants (J6)*

The scavenging effect of the product liquid water on the numerous and, in some cases, soluble contaminant species (figure 3.5.1) was considered because it affects the effective contaminant concentration and has not been previously studied.

The estimation of the relevant time scales indicated that the liquid water accumulation in the gas diffusion electrode is much slower than other time scales that include diffusion in the gas or liquid phase and contaminant absorption in the liquid phase (interface transport and accumulation). Thus the liquid water phase is always saturated with the contaminant (equilibrium between gas and liquid phases). Under this condition, a contaminant mass balance (figure 3.5.2) leads to the following contaminant concentration expression assuming the ideal gas law, an isobaric, isothermal and saturated gas stream, Henry's law, the absence of water crossover, a constant volumetric gas flow rate, a uniform current distribution and the absence of a contaminant reaction:

$$c(x)/c(0) = 1/(1+W_1 x),\ c(0) = \frac{c_{in} c_r}{c_a},\ W_1 = \frac{2\varphi_O H c_r}{r} \quad (3.5.1)$$

where c represents the contaminant concentration, x the dimensionless flow field channel length, W_1 a parameter, c_{in} the inlet contaminant X concentration in the ambient air on a dry basis, c_r the molar concentration of non-vapor gases at saturation conditions within the fuel cell, c_a the molar concentration of an ideal gas at a pressure of 1 atmosphere, φ_O the fraction of oxygen in dry air, H the solubility constant and r the hypothetical oxygen stoichiometry.

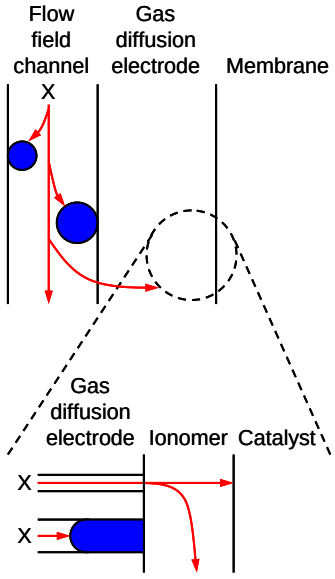

Figure 3.5.1. Contaminant X transport pathways with a simplified gas diffusion electrode/ionomer/catalyst structure illustrating elementary processes. The gas phase contamination path follows the flow field channel and an empty gas diffusion electrode pore to the ionomer and the catalyst. Along the same path the contaminant X dissolves into liquid water drops located in the flow field channel and a partially filled gas diffusion electrode pore decreasing the average contaminant concentration. Reprinted with permission from *ECS Trans.*, **50** (2), 649 (2012). Copyright 2012, The Electrochemical Society.

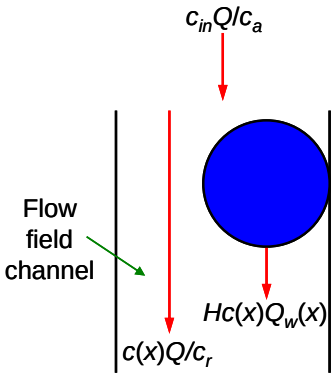

Figure 3.5.2. Contaminant X molar mass balance. The inlet atmospheric stream containing contaminant X saturates the product water leaving a depleted contaminated reactant stream. Reprinted and reformatted with permission from *ECS Trans.*, **50** (2), 649 (2012). Copyright 2012, The Electrochemical Society.

The average contaminant concentration is calculated by integrating equation 3.5.1:

$$\bar{c} / c(0) = \ln(1+W_1)/W_1 \quad (3.5.2)$$

where $\bar{c}$ represents the average contaminant concentration. For W_1 equal to 2.51, the average dimensionless contaminant concentration is equal to 0.5. Figure 3.5.3 indicates that the scavenging effect widely varies with the contaminant (the contaminant solubility H has a large impact) and is very significant especially for the relevant ethylene glycol species (an automotive coolant).

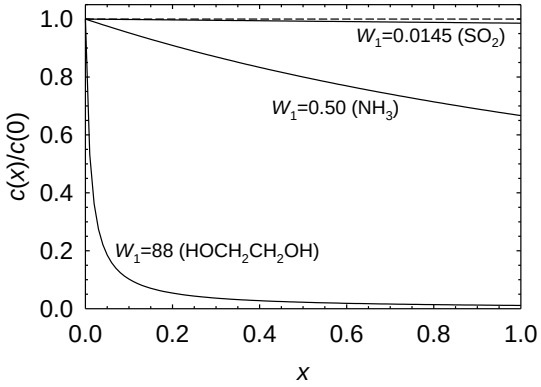

Figure 3.5.3. Dimensionless contaminant concentration in the liquid water (equation 3.5.1) as a function of the dimensionless flow field channel length x and parameter W_1. Reprinted with permission from *ECS Trans.*, **50** (2), 649 (2012). Copyright 2012, The Electrochemical Society.

The model was extended by a generic single ionization reaction (contaminant species dissociation) to demonstrate the importance of this process for low contaminant concentrations. Sulfur dioxide is a model species for this generic ionization reaction and a common air pollutant.

$$SO_2+H_2O \rightarrow H_2SO_3,\ K_H=[H_2SO_3]/[SO_2]=30.9 \text{ mol mol}^{-1} \quad (3.5.3)$$

$$H_2SO_3+H_2O\rightarrow H_3O^+ + HSO_3^-,\ K_1=[H_3O^+][HSO_3^-]/[H_2SO_3]=13.3\ \text{mol m}^{-3} \quad (3.5.4)$$

$$2H_2O\rightarrow H_3O^+ + OH^-,\ K_w=[H_3O^+][OH^-]=10^{-8}\ \text{mol}^2\ \text{m}^{-6} \quad (3.5.5)$$

A sulfur balance leads to a relationship between the SO_2 gas phase concentration and the total amount of sulfur species dissolved:

$$[H_2SO_3]+[HSO_3^-]=K_H[SO_2]+\sqrt{K_1K_H[SO_2]}=Hc(x)+H'\sqrt{c(x)} \quad (3.5.6)$$

As a result of equation 3.5.6, the model was modified to:

$$c(x)/c(0)=\left(\frac{-W_2x}{1+W_1x}+\sqrt{\frac{W_2^2x^2}{(1+W_1x)^2}+\frac{1}{1+W_1x}}\right)^2,\ W_2=\frac{\varphi_O H'c_r}{r\sqrt{c(0)}} \quad (3.5.7)$$

The contaminant concentration is dependent on two parameters in the presence of dissociation reactions. The new parameter W_2 is dependent on the inlet gas phase concentration. As a result, the scavenging effect is relatively more important for small concentration (figure 3.5.4). The extended model shows a significant SO_2 scavenging effect by dissociation below 1 ppm (>50 % is scavenged). For that reason, SO_2 tolerance limits based on extrapolations of high concentration data are conservative and need to be re-interpreted.

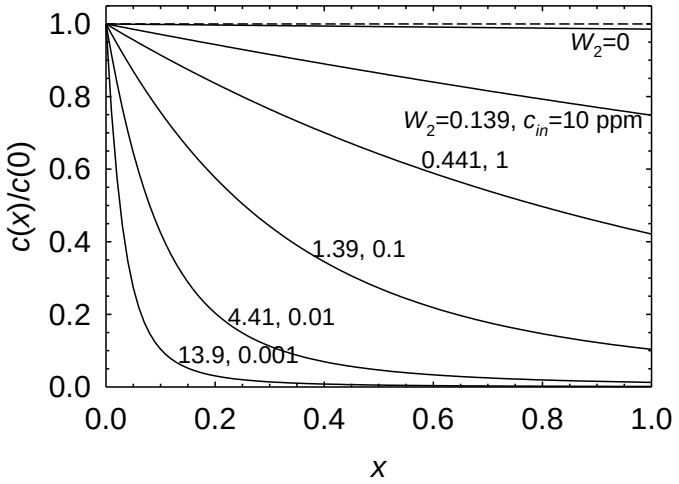

Figure 3.5.4. Dimensionless SO_2 contaminant concentration in the gas phase (equation 3.5.7) as a function of the dimensionless flow field channel length x and parameter W_2. W_1=0.0145. Reprinted and reformatted with permission from *ECS Trans.*, **50** (2), 649 (2012). Copyright 2012, The Electrochemical Society.

A non-operating cell was used for validation to minimize interpretation artifacts by chemical and electrochemical oxidation of contaminants (figure 3.5.5). The water was transferred by a small temperature gradient simulating water production in an operating cell. The absence of the anode gas diffusion layer promoted a good contact between the water and the catalyst layer ionomer. Methanol was used as a non-dissociating model contaminant whereas SO_2 was used as a

dissociating species. The collected water composition was analyzed by cyclic voltammetry and total organic carbon whereas the gas phase was studied by gas chromatography. Results shown in figure 3.5.6, top, left demonstrate the validity of the scavenging model for a non-dissociating contaminant (methanol) over an order of magnitude change in the equivalent stoichiometry *r*. It is also noted that Henry's law coefficient is difficult to quantify because available literature data significantly vary.

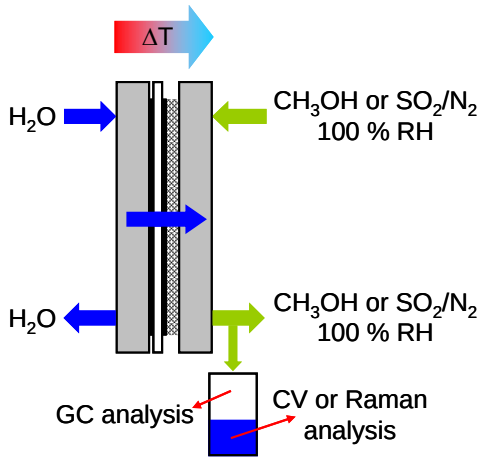

Figure 3.5.5. Scavenging model validation setup with a non-operating cell and a temperature gradient inducing water transport through the membrane. Original, *Journal of The Electrochemical Society*, **161** (8) E3357-E3364 (2014). © The Author(s) 2014. Published by ECS. This is an open access article distributed under the terms of the Creative Commons Attribution Non-Commercial No Derivatives 4.0 License (CC BY-NC-ND, http://creativecommons.org/licenses/by-nc-nd/4.0/), which permits non-commercial reuse, distribution, and reproduction in any medium, provided the original work is not changed in any way and is properly cited. For permission for commercial reuse, please email: oa@electrochem.org. [DOI: 10.1149/2.0291409jes]. All rights reserved.

For SO_2 (figure 3.5.6, top, right and bottom), model curves (full line) adequately reproduce experimental data (circles). Also, the quantity scavenged (the departure from the $c(1)=c(0)$ dash line in figure 3.5.6, top, right equal to $c(0)-c(1)$) progressively increases at low cathode inlet concentrations reflecting the increased contribution from SO_2 dissociation. As a consequence, fuel cell contamination data reported in the literature may be misleading. The effect of SO_2 is usually determined using high concentrations because they accelerate degradation and minimize errors because the performance loss is larger. However, an extrapolation to lower concentrations neglecting the scavenging effect would result in conservative air inlet tolerance limits.

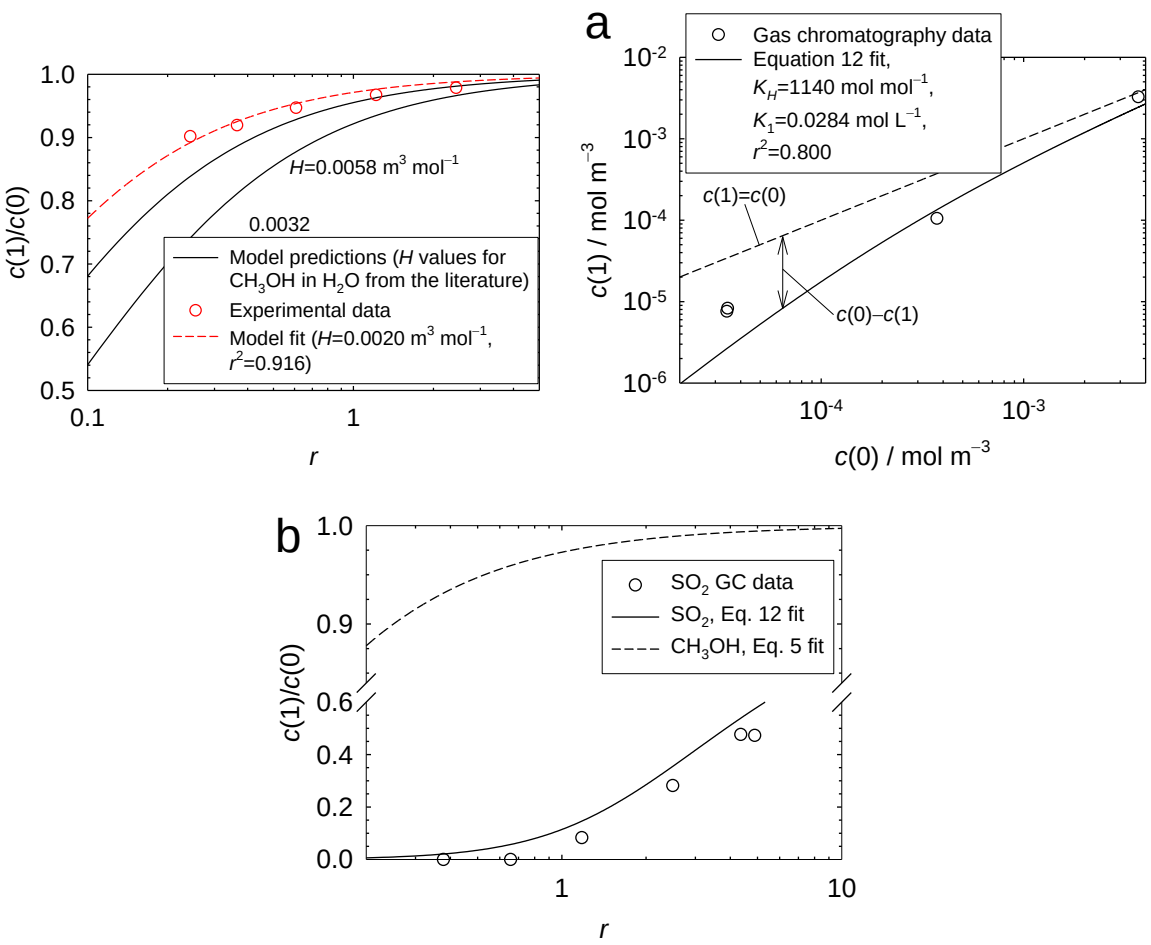

Figure 3.5.6. Methanol concentration data obtained by cyclic voltammetry demonstrate the scavenging model validity in absence of dissociation reactions (top, left). In the presence of SO_2 dissociation reactions (top, right and bottom), good agreement was also obtained. For the top, right figure, r~2.5. For the bottom figure, c_{in}/c_a~10 ppm. Top, right and bottom figures are reformatted originals (axes re-labelled), *Journal of The Electrochemical Society*, **161** (8) E3357-E3364 (2014).

3.5.2 *Contamination by a neutral species sorbed by the ionomer (C2)*

A model was developed for the case of an uncharged species affecting ionomer conductivity using the same principles as prior efforts to develop analytic solutions. The model is based on contaminant transport in gas, liquid water and solid ionomer phases, and interfacial transport between gas/liquid and ionomer phases followed by accumulation in the ionomer and membrane phases. Several simplifications were introduced to exploit the low concentration of the contaminant. The ohmic loss impact on the cell current was obtained (controlled cell voltage) by using an empirical relationship linking the contaminant concentration to the ionomer ionic

conductivity. Solutions are presented in table 3.5.1 for the 2 possible rate determining steps and for both contamination and recovery periods. It is noted that equations have the same form for both rate determining steps (rds).

Table 3.5.1. Model solutions for an ionomer contaminated with an uncharged species.

	Contamination phase	**Recovery phase**
Gas/liquid phase rate determining step	$\frac{i(t)}{i(0)} = 1 + ab\frac{x_X(0,t)}{\alpha_X^{H_2O}}\left(1 - e^{\frac{-k_l \alpha_X^{H_2O} c_{l,H_2O}}{d_l c_{i,H_2O}} t}\right)$	$\frac{i(t)}{i(0)} = 1 + ab\frac{x_X(0,0^-)}{\alpha_X^{H_2O}} e^{\frac{-k_l \alpha_X^{H_2O} c_{l,H_2O}}{d_l c_{i,H_2O}} t}$
Ionomer phase rate determining step	$\frac{i(t)}{i(0)} = 1 + ab\frac{x_X(0,t)}{\alpha_X^{H_2O}}\left(1 - e^{\frac{-2D_i}{d_l d_i} t}\right)$	$\frac{i(t)}{i(0)} = 1 + ab\frac{x_X(0,0^-)}{\alpha_X^{H_2O}} e^{\frac{-2D_i}{d_l d_i} t}$

A comparison with a cell temporarily operated with ethylene glycol is presented in figure 3.5.7 which demonstrates a good agreement with the dimensionless cell resistance. The dimensionless current density, expected to have the same values, is smaller presumably due to the additional effect of glycol adsorption on the catalyst which is not taken into account in the model.

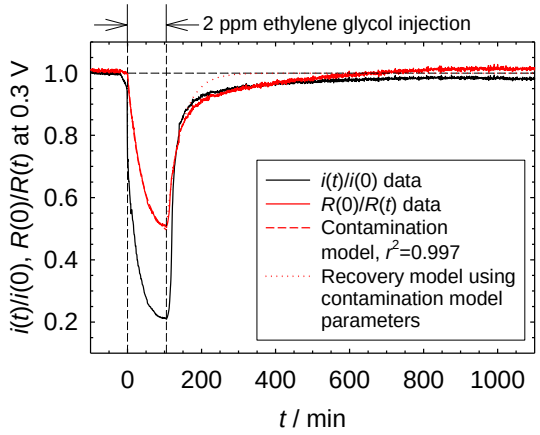

Figure 3.5.7. Comparison between experimental data for a cell temporarily contaminated with ethylene glycol and a dimensionless resistance model.

The model increases the existing model library size (table 3.5.2) [21-24]. The library can be used to facilitate contaminant mechanism identification because experimental current density data obtained in the presence and in the absence of the main reactant and experimental cell resistance data are sufficient to qualitatively distinguish almost all cases (fingerprint characteristics). Separation between 2 qualitatively similar membrane contamination cases (foreign cation X^{+n} and, X electro- and chemically inactive) is possible because model solutions are functionally different. This is a practical approach because few contamination mechanisms were identified [25]. In essence, the model library is similar to the use of continuous stirred tank reactor and plug flow reactor models in chemical engineering which embody ideal behaviors that are used as yardsticks for real reactor performance evaluations. For example, acetylene results in section

2.3.1, figures 2.3.22, top, left and 2.3.24, top correspond to the catalyst contamination kinetics, X electroactive leading to a product P_2, P_2 desorption rds case (table 3.5.2).

Table 3.5.2. Contamination model library summary.

Measured variable for step changes in contaminant concentration				i ($c_R \neq 0$)	i_X or $i_{X^{+n}}$ ($c_R = 0$)
Catalyst contamination kinetics	X electroactive leading to a product P_2	X reaction rds	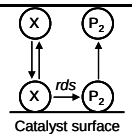	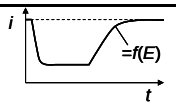	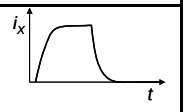
		P_2 desorption rds	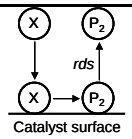	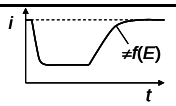	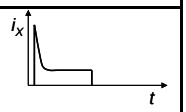
		Irreversible P_2 adsorption	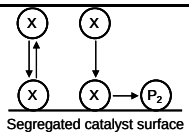	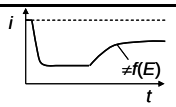	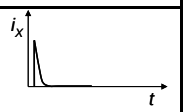
	X electroinactive		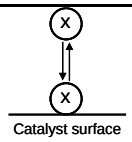	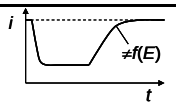	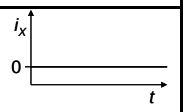
Membrane contamination kinetics	X^{+n} electroinactive		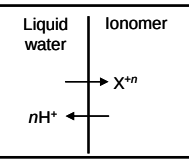	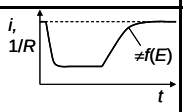	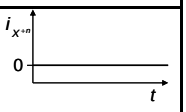
	X electroinactive	X ionization	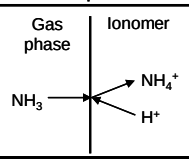	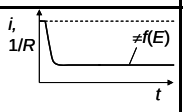	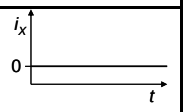
		X chemically inactive	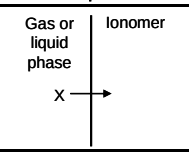	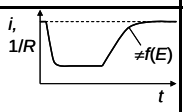	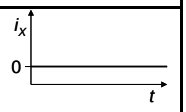

The model library also facilitates cell performance predictions and the definition of tolerance limits because explicit expressions for concentration dependent steady state and time constants are available [26-28].

The model library is currently incomplete. Other relevant cases in need of a derivation include:

- Kinetic losses
  - Metal plating (for example, from catalyst alloys or metallic bipolar plates)
  - Amalgam formation (Hg in H_2 from brine electrolysis and coal, methane and oil reforming)
- Mass transport losses

- Adsorption of a contaminant on the gas diffusion electrode affecting water transport properties (change in hydrophobicity)
- Contaminant supply limitation

3.5.3 *Cation contamination (section 3.1, reference J5)*

Model description, key assumptions, version, source and intended use

The model consists of the anode catalyst layer, the polymer electrolyte membrane (PEM) and the cathode catalyst layer. Hydrogen enters through the anode and oxidizes to produce protons and electrons in the anode catalyst layer (ACL). Electrons travel through the external electrical circuit and protons are transported through the PEM. Contaminated air enters through the cathode and reacts with protons and electrons to form water in the cathode catalyst layer (CCL). The model is based on the following assumptions:

- One dimensional model
- Steady state and isothermal conditions
- Ideal gas mixtures
- Electroneutrality within the membrane

In this model, a mixed domain approach is used. The ionomer phase water concentration is solved in the ACL, the PEM, and the CCL. The gas phase water concentration is solved only in the ACL and CCL. Water is exchanged between the ionomer phase and the gas phase in both catalyst layers. The oxygen concentration is solved only in the CCL, and the hydrogen concentration is solved only in the ACL. The model is developed to predict the effect of foreign cation contamination in polymer electrolyte fuel cells.

Performance criteria for the model related to the intended use

The model is designed to predict the concentration profiles of protons and foreign cations across the membrane/electrode assembly and predict the effect of foreign cations on the cell potential.

Test results to demonstrate the model performance criteria were met

The multiple foreign cation effects are not experimentally separable. Furthermore, measurement methods may include artifacts. As a result, model validation is challenging and was not attemped. Figure 3.5.8 shows the protonic current density distribution along the membrane/electrode assembly thickness during cell operation at 0.7 V. Current density profiles are plotted for both non-contaminated and contaminated cases. First, the baseline case (no contamination) was solved. Subsequently, contamination effects were sequentially added and included proton transport, water transport, oxygen transport and equilibrium potential (Nernst equation). For the absence of contamination case, it is assumed that all sulfonic acid sites are occupied by protons. The protonic current density across the PEM is calculated as 0.72 A cm^{-2} and protons are transported only by migration due to the electrostatic potential gradient.

The first contamination effect is studied by solving the cation transport equation. As Na^+ has a higher affinity for the sulfonic acid site, it replaces the proton, occupies the site and decreases the proton concentration in the ionomer. The proton production and consumption rates in the catalyst layers also decrease because both processes are dependent on proton concentration. As a result, the protonic current density decreases from 0.72 to 0.43 A cm^{-2}, a 40.3 % decrease in current density. As Na^+ replaces protons from sulfonic acid sites, a proton concentration gradient is created across the membrane/electrode assembly, from the anode to the cathode. Consequently, in addition to migration, protons are also transported by diffusion due to the concentration gradient.

The presence of cations in the ionomer decreases the water diffusivity which affects the water content in the ionomer phase. As the membrane proton conductivity is a strong function of water content, the protonic current density further decreases from 0.43 to 0.38 A cm^{-2}. Oxygen diffusivity in the ionomer also decreases due to the presence of foreign cations and current density further decreases to 0.34 A cm^{-2}. Finally, contamination is considered in the calculation of the equilibrium potential by the Nernst equation, which is sensitive to proton concentration. As proton concentration decreases due to Na^+ occupancy, the equilibrium potential drops and the current density further decreases to 0.25 A cm^{-2}. In summary, a total decrease of 65.3 % in current density occurs due to all cation contamination effects. This result is qualitatively consistent with figure 2.3.29.

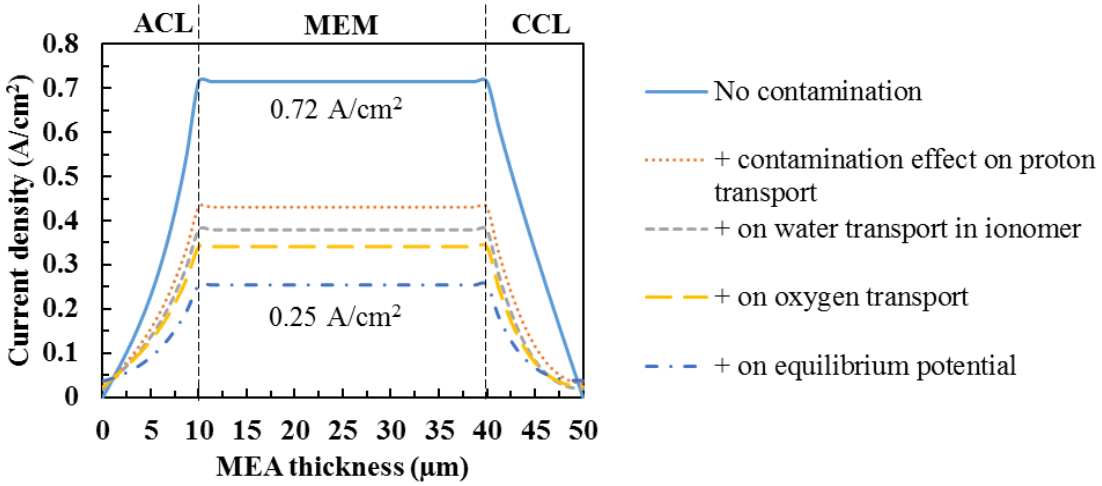

Figure 3.5.8. Calculated protonic current density distribution along the membrane/electrode assembly thickness. The absence of contamination case was solved first. Subsequently, contamination effects were added in sequence: cation transport, water transport, oxygen transport and the Nernst equation. Operating conditions: 0.7 V cell voltage, anode/cathode, 80 %/100 % relative humidity, 80 °C. Reprinted and reformatted with permission from *ECS Trans.*, **64** (3), 649 (2014). Copyright 2014, The Electrochemical Society.

Figure 3.5.9 shows the predicted profiles for the relative Na^+ occupancy in the ionomer along the membrane/electrode assembly thickness. For the absence of contamination case, the Na^+ occupancy is equal to 0 whereas for the contamination case, the Na^+ is introduced from the CCL side. As Nafion has a higher affinity for Na^+ than H^+ ions, Na^+ replaces protons and occupies the sulfonic acid site. This occupancy is expressed by the term "relative Na^+ occupancy" which is

defined by the concentration of Na^+ in the ionomer normalized by the concentration of the sulfonic acid groups. As shown in figure 3.5.9, the relative Na^+ occupancy is larger in the CCL and monotonically decreases from 98 in the CCL to 40 % toward the anode. Na^+ transport in the membrane/electrode assembly is governed by both diffusion due to the concentration gradient and migration due to the potential gradient. As the electrolyte phase potential has a negative slope from the anode to the cathode, migration always drives cations from the anode to the cathode, while diffusion drives cations in the opposite direction (cations are introduced through the cathode). The overall effect leads to a foreign cation accumulation in the CCL.

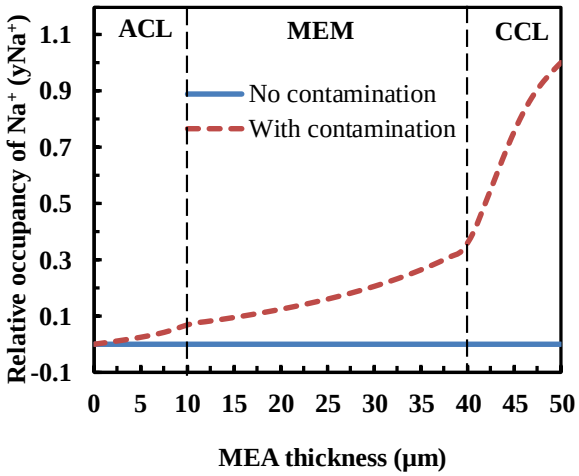

Figure 3.5.9. Calculated relative Na^+ occupancy across the membrane/electrode assembly with and without contaminants in the air stream. The relative Na^+ occupancy is assumed to be 1 at the CCL and cathode gas diffusion layer (GDL) interface. Operating conditions: 0.7 V cell voltage, anode/cathode, 80 %/100 % relative humidity, 80 °C. Reprinted with permission from *J. Electrochem. Soc.*, **161** (10), F1081 (2014). Copyright 2014, The Electrochemical Society.

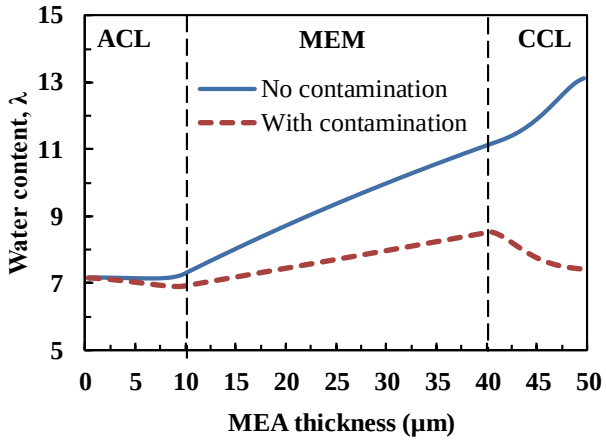

Figure 3.5.10. Calculated water content profile along the membrane/electrode assembly thickness with and without contaminants in the air stream. Operating conditions: 0.7 V cell voltage, anode/cathode, 80 %/100 % relative humidity, 80 °C. Reprinted with permission from *J. Electrochem. Soc.*, **161** (10), F1081 (2014). Copyright 2014, The Electrochemical Society.

Proton transport has a strong dependence on the water content in Nafion membranes. Nafion can conduct protons only in the presence of water, and proton conductivity decreases with a decrease in the level of hydration of the membrane. The decrease in water content is mainly due to the presence of Na^+ in the ionomer. Figure 3.5.10 shows the membrane water content profile across the membrane/electrode assembly thickness. It is assumed that the relative humidity at the ACL/GDL interface and CCL/GDL interface is 80 % and 100 %, respectively, which correspond to water contents of 7.2 and 14 water molecules per sulfonate sites, respectively. For the absence of contamination case, the water content varies from 7.1 to 13.1, from the ACL to the CCL, linearly increasing in the anode to cathode direction. For the contaminated case, water content decreases throughout the membrane/electrode assembly thickness in comparison to the absence of contamination case. The water content change is larger in the CCL and membrane whereas the change is minimal in the ACL.

Figure 3.5.11 shows the gas phase and the dissolved oxygen concentration profile in the CCL for the absence of contamination and contamination cases. As the concentration of Na^+ in the fluid phase is not directly considered, the gas phase oxygen concentration in the presence of contaminant is not affected. The dissolved oxygen concentration for the contamination case varies from the GDL to the PEM side of the CCL as a result of Na^+ occupation (40 to 98 % of the sulfonic acid sites, figure 3.5.9) by the exchange of H^+ with Na^+ in the ionomer, which decreases the oxygen diffusivity and the oxygen reduction rate. The dissolved oxygen concentration in the CCL close to the GDL (between 48 and 50 microns, figure 3.5.11) for the contamination case is larger than in the absence of contamination. As Na^+ occupies 93 to 98 % of the CCL sulfonic acid sites close to the GDL (figure 3.5.9), this region is not active because the proton conductivity and current density are very low. Therefore, the dissolved O_2 concentration in that region is relatively large due to the very low reaction rate.

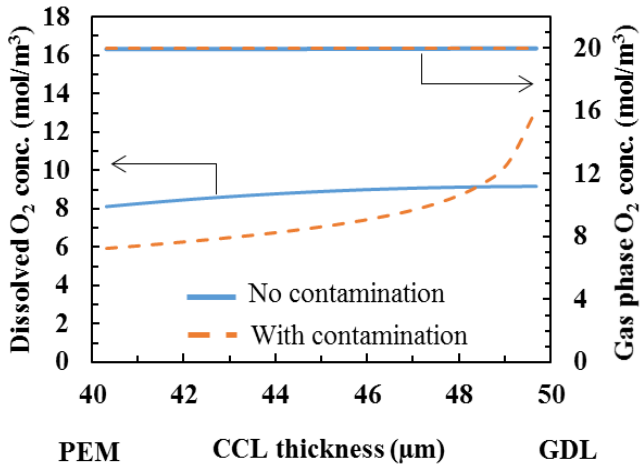

Figure 3.5.11. Calculated gas phase and dissolved oxygen concentration profile in the CCL. Operating conditions: 0.7 V cell voltage, anode/cathode, 80 %/100 % relative humidity, 80 °C. Reprinted with permission from *J. Electrochem. Soc.*, **161** (10), F1081 (2014). Copyright 2014, The Electrochemical Society.

Theory behind the model expressed in non-mathematical terms

Almost all foreign cations have higher affinity for ionomer and membrane sulfonic acid groups than protons. As a result, foreign cations in contact with an ionomer or membrane displace protons contained in these polymers by ion exchange. The presence of foreign cations in the membrane or catalyst layer ionomer results in reduced ionic conductivity, increased electro-osmotic drag and reduced water content. In turn, all these property changes affect species transport and reaction rates. The model considers the transport of foreign cations and protons across the ionomer phase in the polymer electrolyte and catalyst layers, proton generation and consumption in the catalyst layers due to electrochemical reactions, transport of water in ionomer and in void phases (gas phase only), including diffusion and electro-osmotic drag. It also incorporates the transport of hydrogen and oxygen, as well as electrochemical kinetics and ohmic losses to predict cell potential as a function of current density.

Mathematics to be used, including formulas and calculation methods

In this model, three charged species are considered in the PEM: positively charged proton and one foreign cation (Na^+) and negatively charged sulfonic acid sites fixed to the polymer side-chains (stationary species). Two species equations are independent according to the Gibbs-Duhem restriction [29, 30]. Therefore, equation 1 in table 3.5.3 is solved for H^+ and Na^+.

Table 3.5.3. Governing equations in various regions.

Species	Domain	Conservation equation	Eq.	Source
H^+, Na^+	CL, membrane	$\nabla(-N_j) + S_u = 0$	1	$ACL^a: S_u = \frac{j_a}{2F}$ for H^+ $CCL^a: S_u = -\frac{j_c}{4F}$ for H^+
Water	CL, membrane	$\nabla\left(D_w^{m,eff}\frac{\rho_{dry,m}}{EW}\nabla\lambda\right) + S_{w,\lambda} = 0$	2	$ACL: S_{w,\lambda} = h_m(\lambda^{eq}(C_w^g) - \lambda) - \nabla\left(n_d\frac{I}{F}\right)$ $CCL: S_{w,\lambda} = h_m(\lambda^{eq}(C_w^g) - \lambda) - \nabla\left(n_d\frac{I}{F}\right) + \frac{j_c}{4F}$
	CL	$\nabla\left(D_{w,g}^{eff}\frac{\rho_{dry,m}}{EW}\nabla C_w^g\right) + S_{w,g} = 0$	3	$ACL: S_{w,g} = -h_m(\lambda^{eq}(C_w^g) - \lambda)$ $CCL: S_{w,g} = -h_m(\lambda^{eq}(C_w^g) - \lambda)$
Hydrogen	ACL	$\nabla(D_{H_2,g}^{eff}\nabla C_{H_2}^g) + S_{H_2} = 0$	4	$ACL: S_{H_2} = -\frac{j_a}{2F}$
Oxygen	CCL	$\nabla(D_{O_2}^{eff}\nabla C_{O_2}^g) + S_{O_2} = 0$	5	$CCL: S_{O_2} = -\frac{j_c}{4F}$

[a] The source term for Na^+ is zero.

The effective mass diffusivity in porous media is described using the Bruggeman relation: $D_i^{eff} = \varepsilon^{1.5} D_{i.}$

In equation 1 (table 3.5.3), N represents the total flux of cation. Serincan *et al*. [30] derived a cation flux equation using the generalized Maxwell-Stefan (MS) approach. It can be expressed as:

$$\{N\} = -2c_{so_3^-}[B]^{-1}\{\nabla y\} - \frac{2Fc_{so_3^-}}{RT}[B]^{-1}\{z.y\}\nabla\phi \quad (3.5.8)$$

where y is the relative occupancy and [B] is a matrix including binary diffusivities and relative occupancies. The elements of [B] are [31]:

$$B_{jj} = \sum_{\substack{k=1 \\ k\neq j}}^{n} \frac{y_k}{D_{jk}} \quad \text{and} \quad B_{jk} = -\frac{y_j}{D_{jk}} \quad (3.5.9)$$

The binary diffusion coefficient, D_{jk} is calculated by [30]:

$$D_{jk} = \left(D_{j,M}\right)^{x_j} \times \left(D_{k,M}\right)^{x_k} \quad (3.5.10)$$

where $D_{j,M}$ and $D_{k,M}$ are self-diffusivities of species j and k. The proton self-diffusivity is calculated from the Nernst-Einstein relation:

$$\kappa_{H^+} = c_{H^+}D_{j,H^+}\frac{z_{H^+}^2F^2}{RT} \quad (3.5.11)$$

where κ_{H^+} is the proton conductivity. An expression for the membrane conductivity in pure proton form is borrowed from Springer *et al*. [32]:

$$\kappa_{H^+} = (0.5139\lambda - 0.326)\exp\left[1268\left(\frac{1}{303} - \frac{1}{T}\right)\right] \quad (3.5.12)$$

The self-diffusivity of Na^+ is calculated using a relation in terms of polymer volume fraction and water content in the membrane [33, 34]:

$$D_{j,Na^+} = D_{Na^+}^{aq}\exp\left(-b\frac{V_p}{1-V_p}\right) \quad (3.5.13)$$

where $D_{Na^+}^{aq}$ is the aqueous diffusion coefficient of Na^+, V_p is the volume fraction of polymer in the water-swollen membrane and b is an empirical parameter. For a monovalent cation, b is 0.21 [34]. Equation 3.5.13 accounts for the tortuosity effect due to the polymer volume fraction in the polymer matrix.

Water transport across the catalyst layers occur both in the ionomer phase and in the gas phase whereas in the membrane, only water transport in the ionomer phase is relevant. Mass

conservation equations for both phases of water are listed in table 3.5.3 (equations 2 and 3). In those equations, h_m represents the mass transfer coefficient of water between gas phase and ionomer phase, and λ^{eq} is the equilibrium water content at the corresponding gas phase molar concentration C_w^g.

As foreign cations have a higher affinity with sulfonic acid groups than protons and replace protons from active sites by ion exchange, the equivalent water content is calculated by the following equation to account for the presence of both H^+ and Na^+:

$$\lambda^{eq} = y_{H^+} \times \lambda_{H^+}^{eq} + y_{Na^+} \times \lambda_{Na^+}^{eq} \quad (3.5.14)$$

where $\lambda_{H^+}^{eq}$ and $\lambda_{Na^+}^{eq}$ are the water uptake for the membrane in H^+ form and Na^+ form, respectively.

Springer *et al*. [32] provided an expression for the water content in a proton form membrane:

$$\lambda_{H^+}^{eq} = \begin{cases} 0.043 + 17.81a - 39.85a^2 + 36.0a^3 & \text{for } 0 < a \leq 1 \\ 14 + 1.4(a-1) & \text{for } 1 < a \leq 3 \end{cases} \quad (3.5.15)$$

Serincan *et al*. [29] used an expression for $\lambda_{Na^+}^{eq}$ which was a curve fit to the experimental plot of Jalani and Datta [35]:

$$\lambda_{Na^+}^{eq} = 10.3a^3 - 4.73a^2 + 1.78a + 0.0149 \quad (3.5.16)$$

where the water activity, a is defined as:

$$a = \frac{C_w^g RT}{P^{sat}} \quad (3.5.17)$$

Experiments related to equations 3.5.15 and 3.5.16 were completed at 30 °C. These expressions are used here because data are not available at 80 °C for foreign cations.

The effective water diffusivity $D_w^{m,eff}$ in the membrane is calculated using a similar expression as equation 3.5.14 to account for the presence of both H^+ and Na^+. For water diffusivity in a H^+ form membrane, the following expression is borrowed from Motupally et al [36]:

$$D_{w,H^+}^m = \begin{cases} 3.1 \times 10^{-7}\lambda\left(e^{0.28\lambda} - 1\right).e^{\left(-\frac{2346}{T}\right)} & \text{for } 0 < \lambda \leq 3 \\ 4.17 \times 10^{-8}\lambda\left(1 + 161e^{-\lambda}\right).e^{-\frac{2346}{T}} & \text{otherwise} \end{cases} \quad (3.5.18)$$

and for a Na^+ form membrane, a similar expression to equation 3.5.13 is used and given in terms of polymer volume fraction [33]:

$$D^{m}_{w,Na^{+}} = D^{aq}_{w} \exp\left(-b\frac{V_p}{1-V_p}\right) \quad (3.5.19)$$

In equation 3.5.19, the water diffusivity in the Na^+ form membrane not only depends on the tortuosity due to the polymer volume fraction but also on the tortuosity originating from the Na^+ ion. As the membrane in Na^+ form has a higher tortuosity in comparison to a H^+ form membrane, the water diffusivity decreases in the Na^+ form membrane [37]. Moreover, the equilibrium water content decreases from 14 (H^+ form) to 7.36 (Na^+ form) for a membrane exposed to a water activity of 1 at 30 °C [29].

In the CCL, a spherical agglomerate model is considered to account for micro-scale effects of foreign cations (change in effective oxygen diffusivity in the ionomer phase). It is assumed that the agglomerate outer layer is covered with a thin ionomer film and each agglomerate consists of a cluster of carbon particles covered with Pt catalyst nano-particles. Interior pores (primary pores) in each agglomerate are filled with ionomer. Secondary pores exist between agglomerates, provide space for gas diffusion and are partially or fully filled with water. Oxygen diffuses through the secondary pores and reaches the agglomerate ionomer film surface. Oxygen subsequently dissolves into the film and diffuses through it to reach catalyst sites.

The dissolved oxygen concentration is calculated in two steps. First, the gas phase oxygen concentration is solved by the model by taking into account reaction kinetics and diffusion through secondary pores (equation 5 in table 3.5.3). Second, the ionomer phase oxygen concentration is calculated using analytical relations.

The dissolved oxygen concentration at the pore/ionomer film interface is described by Henry's law:

$$C^{m}_{O_2,film-pore} = \frac{C^{g}_{O_2}}{K_{O_2}/(RT)} \quad (3.5.20)$$

The dissolved oxygen concentration at the interface of the ionomer film and agglomerate core is expressed as [38]:

$$C^{m}_{O_2} = \left(1 + \frac{AEk\delta_{agg}}{a_{agg}D^{m}_{O_2}}\frac{r_{agg}+\delta_{agg}}{r_{agg}}\right)^{-1} C^{m}_{O_2,film-pore} \quad (3.5.21)$$

where k is the reaction rate constant. It is defined as:

$$k = \frac{j_c}{4FC^{m}_{O_2}} \quad (3.5.22)$$

All other terms in equation 3.5.21 and other related relations are taken from the study of Khajeh-Hosseini-Dalasm *et al.* [39, 40].

It is assumed that open pores in the CCL contain water. Oxygen passes through both liquid water and open space in pores to reach the surface of the agglomerate ionomer film. A parallel model that accounts for oxygen transport in both media is assumed to calculate the oxygen diffusion coefficient [38]:

$$D_{O_2}^{eff} = D_{O_2,g}^{eff} \frac{(1-s)\varepsilon_{cl}}{\varepsilon_{cl} + \varepsilon_{gcl}(1-\varepsilon_{GDL})} + D_{O_2,w}^{eff} \frac{s\varepsilon_{cl}}{\varepsilon_{cl} + \varepsilon_{gcl}(1-\varepsilon_{GDL})} \quad (3.5.23)$$

where $D_{O_2-g}^{eff}$ and $D_{O_2-w}^{eff}$ are the effective oxygen gas diffusion coefficients in gas pores and liquid water, respectively. The Bruggeman correlation is used to calculate the effective diffusivity of oxygen:

$$D_{O_2,g}^{eff} = ((1-s)\varepsilon_{cl})^{1.5} D_{O_2,g} \quad (3.5.24)$$

$$D_{O_2,w}^{eff} = (s\varepsilon_{cl})^{1.5} D_{O_2,w} \quad (3.5.25)$$

where $D_{O_2,g}$ and $D_{O_2,w}$ are the diffusion coefficients of oxygen in the gas phase and the water phase, respectively and the water phase diffusivity is expressed as [41]:

$$D_{O_2,w} = 4522 \times 10^{-9} \exp\left(-\frac{2287.9}{T}\right) \quad (3.5.26)$$

The dissolved oxygen diffusivity in the ionomer phase $D_{O_2}^{m}$ is calculated using a similar approach as equation 3.5.14 and considers the effect of both H^+ and Na^+ presence in the ionomer. The oxygen diffusivity in the ionomer in H^+ form is obtained from Sakai *et al.*'s experimental data for Nafion 125 [42] whereas diffusivity data for a Na^+ form ionomer as reported by Ogumi *et al.* for Nafion 120 are used [43]. The dissolved oxygen diffusivity for foreign cation form membranes is smaller than the value measured for an acid form membrane [42].

Whether or not the theory and mathematical algorithms were peer reviewed, and, if so, include a summary of theoretical strengths and weaknesses

The physical model and the corresponding mathematical model were published in peer reviewed publications (section 3.1, references J5, C14). The major model strength is the comprehensive analysis of all effects of foreign cations, which was previously limited to the effect on proton transport. The absence of a description for the foreign ion transport between the open void phase and the ionomer phase (cation transport in water drops/columns in flow field channels/gas diffusion layers, ion exchange at the water phase/ionomer phase interface), particularly in catalyst layers, represents the major model weakness.

Hardware requirements

The model is solved using Matlab and therefore it should work on any platform that runs Matlab. However the performance (solution time to reach convergence) may vary. The model was only tested on a Microsoft Windows platform with Matlab v12.

Documentation (model code, user guide, etc.)

The Matlab code and the user guide were submitted at the same time as this report.

4 References

[1] J. St-Pierre, *Electrochim. Acta*, **55** (2010) 4208.
[2] J. Becker, C. Brandt, D. Dauble, *Environ. Toxicol. Chem.*, **17** (1998) 2354.
[3] B. L. Kienitz, H. Baskaran, T. A. Zawodzinski Jr., *Electrochim. Acta*, **54** (2009) 1671.
[4] D. Strmcnik, D. F. van der Vliet, K.-C. Chang, V. Komanicky, K. Kodama, H. You, V. R. Stamenkovic, N. M. Marković, *J. Phys. Chem. Lett.*, **2** (2011) 2733.
[5] T. Okada, J. Dale, Y. Ayato, O. A. Asbjørnsen, M. Yuasa, I. Sekine, *Langmuir*, **15** (1999) 8490.
[6] N. Nonoyama, S. Okazaki, A. Z. Weber, Y. Ikogi, T. Yoshida, *J. Electrochem. Soc.*, **158** (2011) B416.
[7] A. Ohma, T. Mashio, K. Sato, H. Iden, Y. Ono, K. Sakai, K. Akizuki, S. Takaichi, K. Shinohara, *Electrochim. Acta*, **56** (2011) 10832.
[8] T. A. Greszler, D. Caulk, P. Sinha, *J. Electrochem. Soc.*, **159** (2012) F831.
[9] J. P. Owejan, J. E. Owejan, W. Gu, *J. Electrochem. Soc.*, **160** (2013) F824.
[10] A. Z. Weber, A. Kusoglu, *J. Mater. Chem. A*, **2** (2014) 17207.
[11] R. E. Melnick, G. T. R. Palmore, *J. Phys. Chem. B*, **105** (2001) 1012.
[12] R. E. Melnick, G. T. R. Palmore, *J. Phys. Chem. B*, **105** (2001) 9449.
[13] *Electrocatalysis*, J. Lipkowski, P. N. Ross, Editors, Wiley-VCH, 1998.
[14] B. Kienitz, B. Pivovar, T. Zawodzinski, F. H. Garzon, J. Electrochem. Soc., **158** (2011) B1175.
[15] A. Pozio, R. F. Silva, M. De Francesco, L. Giorgi, *Electrochim. Acta*, **48** (2003) 1543.
[16] Y. Zhai, K. Bethune, G. Bender, R. Rocheleau, *J. Electrochem. Soc.*, **159** (2012) B524.
[17] Y. W. Rho, S. Srinivasan, Y. T. Kho, *J. Electrochem. Soc.*, **141** (1994) 2089.
[18] H. A. Gasteiger, S. S. Kocha, B. Sompalli, F. T. Wagner, *Appl. Catal. B*, **56** (2005) 9.
[19] Y. Zhai, G. Bender, S. Dorn, R. Rocheleau, *J. Electrochem. Soc.*, **157** (2010) B20.
[20] Y. Garsany, J. Ge, J. St-Pierre, R. Rocheleau, K. E. Swider-Lyons, *J. Electrochem. Soc.*, **161** (2014) F628.
[21] J. St-Pierre, *J. Electrochem. Soc.*, **156** (2009) B291.
[22] J. St-Pierre, *J. Power Sources*, **195** (2010) 6379.
[23] J. St-Pierre, *J. Power Sources*, **196** (2011) 6274.
[24] J. St-Pierre, *Int. J. Hydrogen Energy*, **36** (2011) 5527.
[25] J. St-Pierre, 'Air Impurities', in *Polymer Electrolyte Fuel Cell Durability*, Edited by F. N. Büchi, M. Inaba, T. J. Schmidt, Springer, 2009, p. 289.
[26] J. St-Pierre, *Electrochim. Acta*, **55** (2010) 4208.
[27] J. St-Pierre, *J. Power Sources*, **195** (2010) 6379.
[28] J. St-Pierre, *Int. J. Hydrogen Energy*, **36** (2011) 5527.
[29] M. F. Serincan, U. Pasaogullari, T. Molter, *Int. J. Hydrogen Energy*, **35** (2010) 5539.
[30] R. Krishna, J. A. Wesselingh, *Chem. Eng. Sci.*, **52** (1997) 861.
[31] E. Leonardi, C. Angeli, *J. Phys. Chem. B*, **114** (2009) 151.
[32] T. E. Springer, T. Zawodzinski, S. Gottesfeld, *J. Electrochem. Soc.*, **138** (1991) 2334.
[33] H. Yasuda, C. E. Lamaze, L. D. Ikenberry, *Makromol. Chem.*, **118** (1968) 19.

[34] A. Goswami, A. Acharya, A. Pandey, *J. Phys. Chem. B*, **105** (2001) 9196.
[35] H. Jalani, R. Datta, *J. Membr. Sci.*, **264** (2005) 167.
[36] S. Motupally, A. J. Becker, J. W. Weidner, *J. Electrochem. Soc.*, **147** (2000) 3171.
[37] G. Suresh, S. Sodaye, Y. Scindia, A. Pandey, A. Goswami, *Electrochim. Acta.*, **52** (2007) 5968.
[38] N. Khajeh-Hosseini-Dalasm, M. Fesanghary, K. Fushinobu, K. Okazaki, *Electrochim. Acta.*, **60** (2012) 55.
[39] N. Khajeh-Hosseini-Dalasm, M. Kermani, D. G. Moghaddam, J. Stockie, *Int. J. Hydrogen Energy*, **35** (2010) 2417.
[40] N. Khajeh-Hosseini-Dalasm, S. Ahadian, K. Fushinobu, K. Okazaki, Y. Kawazoe, *J. Power Sources*, **196** (2011) 3750.
[41] K. Morohoshi, T. Hayashi, *Polymers*, **5** (2013) 56.
[42] T. Sakai, H. Takenaka, E. Torikai, *J. Electrochem. Soc.*, **133** (1986) 88.
[43] Z. Ogumi, Z. Takehara, S. Yoshizawa, *J. Electrochem. Soc.*, **131** (1984) 769.